This is to certify that the

dissertation entitled

Optical Properties of Ordered and Disordered Systems

presented by

N. Kedarnath

has been accepted towards fulfillment
of the requirements for

Ph.D. degree in Physics

C. L. Foiles
Major professor

Date August 19, 1987

OPTICAL PROPERTIES OF ORDERED AND DISORDERED SYSTEMS

by

N. Kedarnath

A Dissertation

Submitted to
Michigan State University
in partial fulfillment of the requirements
for the degree of

DOCTOR OF PHILOSOPHY

Department of Physics and Astronomy
1987

ABSTRACT

OPTICAL PROPERTIES OF ORDERED AND DISORDERED SYSTEMS

BY

N. KEDARNATH

An experimental investigation of the effects of generalized order-disorder transitions on the optical properties and electronic levels in three metallic systems is described. The three metallic systems studied were (1) atomically ordered and disordered $Cu_{1-x}Pt_x$ alloys ($x \leq 0.25$), (2) metallic glass a-$Fe_{0.8}B_{0.2}$ and (3) layered and laser quenched Ni-Ti alloys. Measurements of the optical reflectivity in the energy range 1 eV to 5 eV and the electron energy loss spectra in the energy range 3 eV to 90 eV were undertaken to study electronic properties. Sample characterization was achieved by X-ray and electron diffraction for structure determination and X-ray energy dispersive spectroscopy for composition micro-analysis.

In dilute ($x \leq 0.10$) $Cu_{1-x}Pt_x$ disordered alloys, an indirect evidence suggesting the formation of Pt derived impurity states (virtual bound states) was seen. In alloys with $0.175 \leq x \leq 0.25$ certain order-disorder related effects were identified. These included (1) an overall lower

reflectivity of the ordered phase compared to the disordered phase and (2) a structure in $\varepsilon_2(\omega)$ at about 6 eV seen only in the disordered phase. Origins of these effects are discussed in detail.

The electron energy loss spectra of the metallic glass a-$Fe_{0.8}$ $B_{0.2}$ agree well with the results of other investigators. Certain features (at 2.5 eV and 4.0 eV) in the loss spectra attributed to volume excitations by other investigators were seen to be due to surface excitations. Directly measured and computed reflectivities agree well with published results; a significant difference between our computed $\varepsilon_2(\omega)$ and that of other workers was seen.

The energy loss spectra of layered NiTi was seen to be different from a simple superposition of the spectra of Ni and Ti. In addition, a close resemblance between the EELS of layered Ni-Ti and crystalline NiTi alloy was seen. The processes of alloying and amorphization appeared to have no effect on the dominant loss feature in the EELS of these systems. However, the $M_{2,3}$ core losses of Ti appeared to have undergone a large change in the laser quenched alloy, indicating a drastic change in the joint density of states associated with these transitions.

ACKNOWLEDGMENTS

I would like to thank Dr. Carl Foiles for his continued help and guidance during the course of the work described here. In addition to learning many techniques of experimental physics, I have obtained from him an essential ingredient for success in any endeavor of this nature--perseverance. For this and his words of encouragement I am greatly in debt.

I would also like to thank Dr. S. D. Mahanti and Dr. A. Bansil and Dr. R. Prasad of North Eastern University for their contribution to my understanding of the Cu-Pt alloy system. In addition, I would like to acknowledge the assistance provided by Dr. J. Cowen, Dr. J. Nolen, Dr. K. Mukhergee and Dr. P. Duxbury in reviewing this manuscript and suggesting improvements.

Mr. V. Shull and Dr. S. Mahmood provided invaluable assistance during my early attempts to use the electron microscope, and I am very thankful for that.

I would like to thank my family, especially my sisters Jana and Rukku, for their behind-the-scene support and

encouragement without which I certainly would not have come this far.

I would like to acknowledge the financial support provided by NSF, MSU-CFMR, MSU-AEM Laboratory and the Physics Department.

TABLE OF CONTENTS

LIST OF FIGURES

Figure Page

CHAPTER 1

INTRODUCTION

Optical and electronic properties of various solids are strongly influenced by the electronic states and energy levels. Properties like electrical and thermal conductivity, magnetic susceptibility and even the physical appearance like color of the solid all have their origin in the electronic band structure; macroscopic properties like the dielectric function can be derived from quantum mechanical descriptions of the electrons in a solid. Thus, a study of the physical properties of solids leads one to a study of the energy levels and states of the electrons in these systems.

The electronic states are influenced by, among other factors, physical structure of the solid. The presence of a long range order in the structure profoundly affects the electronic states and causes changes in the electronic properties. The element germanium which occurs in crystalline and amorphous phases offers a dramatic illustration of this point. The optical reflectivity of amorphous Ge lacks the rich detail (sharp structures) found in the reflectivity of the crystalline phase.

This study is an attempt to systematically study the

CHAPTER 1

INTRODUCTION

Optical and electronic properties of various solids are strongly influenced by the electronic states and energy levels. Properties like electrical and thermal conductivity, magnetic susceptibility and even the physical appearance like color of the solid all have their origin in the electronic band structure; macroscopic properties like the dielectric function can be derived from quantum mechanical descriptions of the electrons in a solid. Thus, a study of the physical properties of solids leads one to a study of the energy levels and states of the electrons in these systems.

The electronic states are influenced by, among other factors, physical structure of the solid. The presence of a long range order in the structure profoundly affects the electronic states and causes changes in the electronic properties. The element germanium which occurs in crystalline and amorphous phases offers a dramatic illustration of this point. The optical reflectivity of amorphous Ge lacks the rich detail (sharp structures) found in the reflectivity of the crystalline phase.

This study is an attempt to systematically study the

effects of generalized order-disorder effects on the optical and electronic properties of solids. We identified three kinds of disorders and focussed our attention on their effects on the electronic excitation spectra. The types of disorder chosen were:

(i) atomic order-disorder in crystalline solids
(ii) artificial order
(iii) topological disorders (metallic glasses)

The noble metal alloy $Cu_{1-x}Pt_x$ $(0.175 \leq x \leq 0.25)$ was selected as a candidate for the atomic order-disorder study. Alloys with low Pt concentration (10% and lower) were also studied . The metallic glasses a-$Fe_{0.8}B_{0.2}$ and laser quenched NiTi alloys were studied as specific examples of systems with topological disorders. Alternating thin (about 50 A) layers of Ni and Ti sputtered on suitable substrates were studied as systems with artificial order.

The triad Cu-Au, Cu-Pd and Cu-Pt alloys are well suited for the study of order-disorder effects. These alloys occur in atomically ordered and substitutionally disordered phases for a range of compositions. Though several experimental investigations of these alloys have been conducted, they are in no sense comprehensive. The alloy system Cu-Au has been well investigated. Independent studies of the valence and conduction bands density of states in Cu-Au by photoemissionspectroscopy and measurements of the transport and magnetic properties are available.

In contrast, there is very little experimental data available on the properties of Cu-Pd and Cu-Pt alloys. There exist in the scientific literature some reports of resistivity and thermopower measurements on the Cu-Pd and Cu-Pt systems. Some photoemission investigations (X-ray and Ultraviolet Photoemission Spectroscopy) have been done on the Cu-Pd system and virtually none on the Cu-Pt system. To the best of our knowledge, the work described in this dissertation is the only effort to date to study the optical properties and electronic structure of the Cu-Pt alloy system.

The layered Ni-Ti system was chosen as a candidate for the study of the influence of artificial order on the electronic properties. The samples were alternating layers (thickness ~ 50 A) of crystalline Ni and Ti sputtered onto suitable substrates. Layered systems with well defined sharp interfaces between the layers exhibit electronic excitations not present in the constituent elements. For example, collective oscillations of electrons at the interfaces can be present in ideal layered systems. Furthermore, the distributions of the conduction and valence electrons in the layers are likely to be different from the distribution in the constituent elements due to transfers of charge between the layers. Such charge transfers change the density of states (DOS) and the Fermi energy and significantly alter the electronic excitations.

Experimental methods like optical reflectivity measurements and Electron Energy Loss Spectroscopy (EELS) are very useful for tracking these changes in the excitation spectra.

To study the effects of topological disorders and the loss of long range order two metallic glasses--a-$Fe_{0.8}B_{0.2}$ and laser quenched Ni-Ti alloys--were chosen.

The metallic glass $Fe_{0.8}B_{0.2}$ has been well studied by electron spectroscopic methods by various investigators. These measurements do not yield a clear picture of the fundamental electronic processes in a-$Fe_{0.8}B_{0.2}$ due to some discrepancies among various experimental results. The reason for these discrepancies is mainly the fact that most of the existing measurements come from techniques that are sensitive to the condition of the samples' surfaces. This problem has been alleviated to some extent in this study by the use of techniques that have different (and lower) sensitivity to surface excitations. The results of our measurements are presented and compared with published results.

The layered Ni-Ti samples studied as an example of systems with artificial order were later converted into metallic glasses by laser quenching. Significant changes in the local atomic arrangement occur in these crystalline → amorphous transitions. Current models of the alloying process suggest that the valence and conduction electrons states are affected by these phase and composition

changes;because of their higher binding energies, deep core levels would not be susceptible to any changes. Electron energy loss measurements show evidence to the contrary. These results are discussed in detail.

Chapter 2 of the dissertation describes the important material characterization techniques and spectroscopic methods employed in this study. Chapters 3, 4 and 5 discuss the studies on the ordered-disordered $Cu_{1-x}Pt_x$ alloys, the a-$Fe_{0.8}B_{0.2}$ metallic glass and the Ni-Ti system (layered and laser quenched) respectively. These chapters are to be treated as being independent pieces of work because of the diverse types of disorders investigated. No attempt has been made to collect the results of the three chapters and draw a simple conclusion.

CHAPTER 2

EXPERIMENTAL TECHNIQUES

Several experimental techniques that were employed during the course of this study are described in this chapter. Techniques described include X-ray diffraction, electron diffraction and X-ray energy dispersive spectroscopy (EDS) for characterization of the samples. Also described are analytical methods such as electron energy loss spectroscopy (EELS) and optical reflectivity spectroscopy for investigation of electronic properties of the systems under study.

The systems studied may be broadly divided into two classes--crystalline and amorphous. The following specific samples of crystalline solids were studied:

1. Binary alloys with substitutional disorder ($Cu_{1-x}Pt_x$)
2. Binary alloys with chemical (atomic) order ($Cu_{1-x}Pt_x$ and NiTi)
3. Layered systems

The metallic glasses $Fe_{0.8}B_{0.2}$ and NiTi were studied as representatives of amorphous systems.

DIFFRACTION TECHNIQUES

In order to determine the crystal structure of the various alloys studied, the techniques of electron diffraction and X-ray diffraction were used. Characterization of the crystal structure through electron diffraction was done in the FE-STEM using the microscope's selected area and micro-diffraction capabilities. A Rigaku X-ray diffractometer was used for the X-ray diffraction studies. The following two sections describe the two diffraction techniques.

X-RAY DIFFRACTION:

The principle of X-ray diffraction is expressed by the Bragg equation [2.1, 2.2]:

$$2d \sin\theta = n\lambda$$

where d is the spacing between the planes participating in the reflection, θ the incident angle of the x-ray beam relative to the sample's surface, n is the order of the reflection and λ is the x-ray wavelength used (λ = 1.54 A, Cu Kα radiation).

In a polycrystalline solid, the crystallites are oriented randomly and as θ is scanned reflections from different crystal planes appear at angles that satisfy the Bragg equation. Once these Bragg peaks are indexed (i.e. the [hkl] planes responsible for those reflections identified), it is a simple task to compute the lattice constant or any other relevant parameters.

In a crystal, the regular arrangement of atoms on lattice sites leads to the formation of many atomic planes. These are the (hkl) planes separated by characteristic distances d_{hkl}. Here, h, k and l are the Miller induces that specify crystal planes and directions. X-radiation of wavelength λ incident on a set of planes is elastically scattered in all directions--atoms in these planes acting as sources of radiation [2.1, 2.2, 2.3]. Since the size of these atoms is comparable to the wavelength the incident radiation ($r_{atom} \simeq \lambda$), they cannot be regarded as point sources; and this fact is taken into account by the atomic form factor f when computing the intensity of scattered (diffracted) radiation[2.1, 2.2, 2.3].

The amplitudes of the elastically scattered radiation add to give intense scattering in certain directions ($\sin\theta_{hkl} = n\lambda/2d_{hkl}$) relative to the incident radiation. These are the various Bragg peaks in the diffraction pattern. In a crystal of a given Bravais lattice (say FCC crystal), the relative arrangement of the atoms also determines the intensity of the diffraction peaks. This influence of the crystal structure on the intensities of the scattered radiation is mirrored in a quantity called 'geometrical structure factor,' F [2.1, 2.3]. A rigorous calculation [2.1] of the structure factor for a FCC crystal

shows that Bragg peaks from planes of mixed indices are absent in the diffraction pattern. For the BCC crystal reflections from planes with (h+k+l) odd are absent. One may use this fact to measure (experimentally) the long range order parameter of a chemically ordered crystal [2.1]. This is explained later in this section.

The CuPt alloys studied were of two different crystal structures--ordered and disordered crystals. The ordered alloy was made by a very slow cooling (few degrees/day) of the alloy melt. At such low rates of cooling, the atoms of the alloy crystallize in the lowest energy configuration--that of a FCC crystal having chemical (atomic) order. In a fully ordered Cu_3Pt crystal, the copper atoms occupy the face center positions and the platinum atoms occupy the cube corners. If the alloy melt is cooled (quenched) rapidly, the atoms will not be able to rearrange to achieve the chemically ordered crystalline state; instead, they will carry into the crystalline state some of the disorder that is characteristic of the melt. In the disordered Cu_3Pt alloy, each FCC site is occupied by a copper or a platinum atom with a probability that depends on the relative concentrations of the two elements. Thus, the ordered Cu_3Pt alloy possesses a superlattice structure and the disordered Cu_3Pt alloy does not. This is true for alloys with platinum concentration in the range 15% to 35% (see Figure 2.1 for a phase diagram of the Cu-Pt system). Figures 2.2 and 2.3 depict the arrangement of Cu and Pt atoms in these alloys.

In order to quantify the degree of chemical order, the Long Range Order (LRO) parameter S is defined as follows [2.1]:

$$S = \frac{(R_A - C_A)}{(1 - C_A)}$$

where R_A is the fraction of 'A' sites occupied by A and C_A is the concentration fraction of A.

The order parameter may be experimentally determined using X-ray diffraction techniques [2.1]. The presence of order in binary alloys leads to the occurrence of certain Bragg reflection lines that are absent for a pure element of the same crystal structure. In the FCC crystal structure (of a pure element), only planes of unmixed indices (all even or all odd) give rise to diffraction peaks. These are the Fundamental lines of the diffraction pattern. A disordered Cu_3Pt can be considered to be made of just one kind of atom, an 'average' atom (25% Pt and 75% Cu). Thus the disordered Cu_3Pt crystal does not produce the (100), (110), (210) . . . diffraction peaks.

In an ordered Cu_3Pt crystal, there are planes of Cu atoms midway between the (100) plans of Pt and Cu. The amplitude of X-rays scattered by these planes of copper does not exactly cancel the scattered amplitude from the (100)

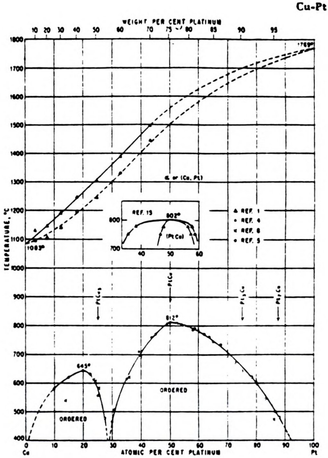

Figure 2.1

Phase Diagram of the Cu-Pt System

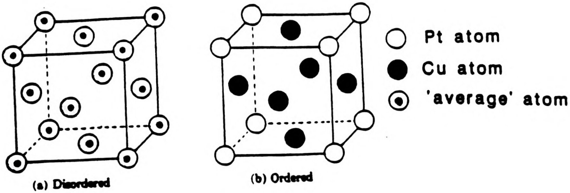

Figure 2.2

Unit Cells of Ordered and Disordered Cu_3Pt Alloys

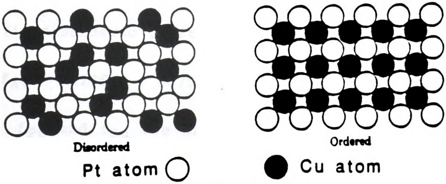

Figure 2.3

100) Planes of Ordered and Disordered Cu_3Pt Alloys

planes of copper and platinum. This gives rise to the (100) reflection in the diffraction pattern of the ordered Cu_3Pt crystal. Such diffraction peaks that are peculiar to the ordered alloy are called 'superlattice' lines. These include the (100), (110), (210) lines for the FCC crystal. By measuring the ratio of integrated intensities of a superlattice line and a fundamental line, one may deduce the degree of order in the alloy [2.1].

The detected intensity of a diffraction peak is given by [2.1]

$$I(hkl) = |F|^2 p \left(\frac{1 + \cos^2\theta}{\sin^2\theta \cos\theta}\right) A(\theta) e^{-2M}$$

where F is the geometrical structure factor ,p the multiplicity factor, $A(\theta)$ the absorption factor and e^{-2M} the temperature dependent Debye-Waller factor

The atomic scattering factor of the 'average' Cu-Pt atom (in disordered Cu_3Pt) is given by [2.1]:

$$f_{av} = 0.25 f_{Pt} + 0.75 fC_u$$

Here, f_{Pt} and f_{Cu} are the atomic scattering factors of Cu and Pt atoms.

There are four 'average' atoms in each unit cell at 000, ½½0, ½0½ and 0½½. Therefore, the structure factor is given by [2.1]:

$$F = \sum_i f_i e^{2\pi i(hu + kv + l_w)}$$

$$= f_{av}[1 + e^{\pi i(h+k)} + e^{\pi i(h+l)} + e^{\pi i(k+l)}]$$

$F = 4\ f_{av}$ for hkl unmixed

$F = 0$ for hkl mixed

In the completely ordered alloy, each unit cell contains one Pt atom at 000 and 3 Cu atoms at ½½0, ½0½ and 0½½.

$F = (f_{Pt} + 3f_{Cu})$ for hkl unmixed

$F = (f_{Pt} - f_{Cu})$ for hkl mixed

In an ordered alloy of order parameters S, the last expression for F is modified to [2.1]:

$F = S\ (F_{Pt} - F_{Cu})$ for hkl mixed.

The measured intensity of a reflection is proportional to $|F|^2$ and hence to $|S|^2$.

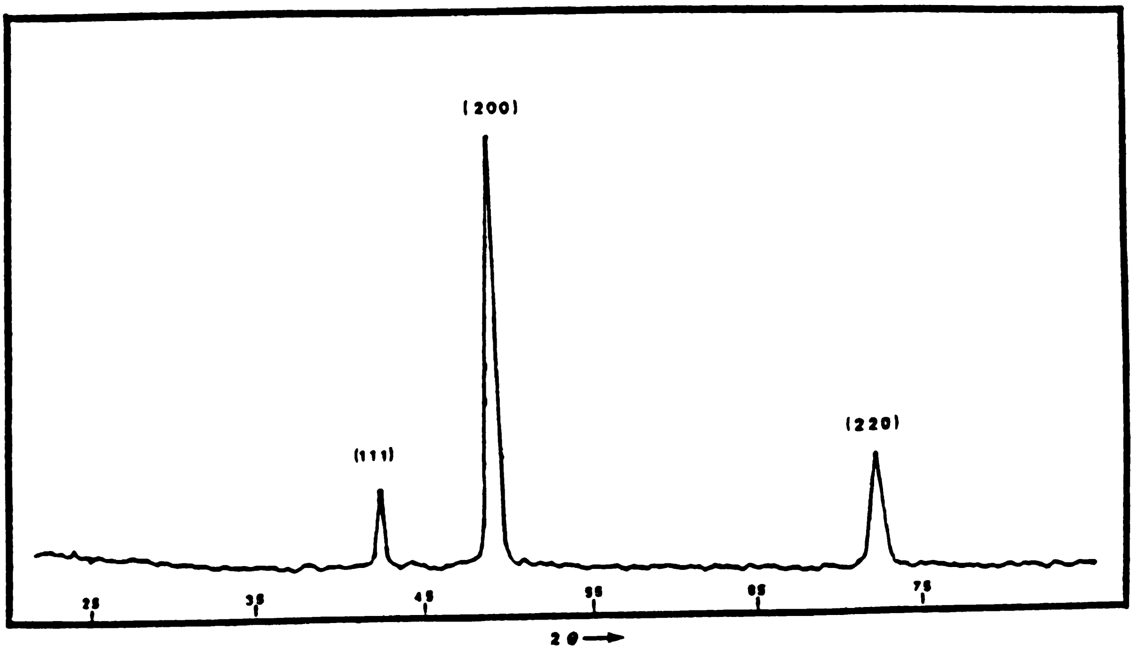

Figure 2.4

X-ray Diffraction Pattern of Disordered $Cu_{0.8}Pt$ Alloy

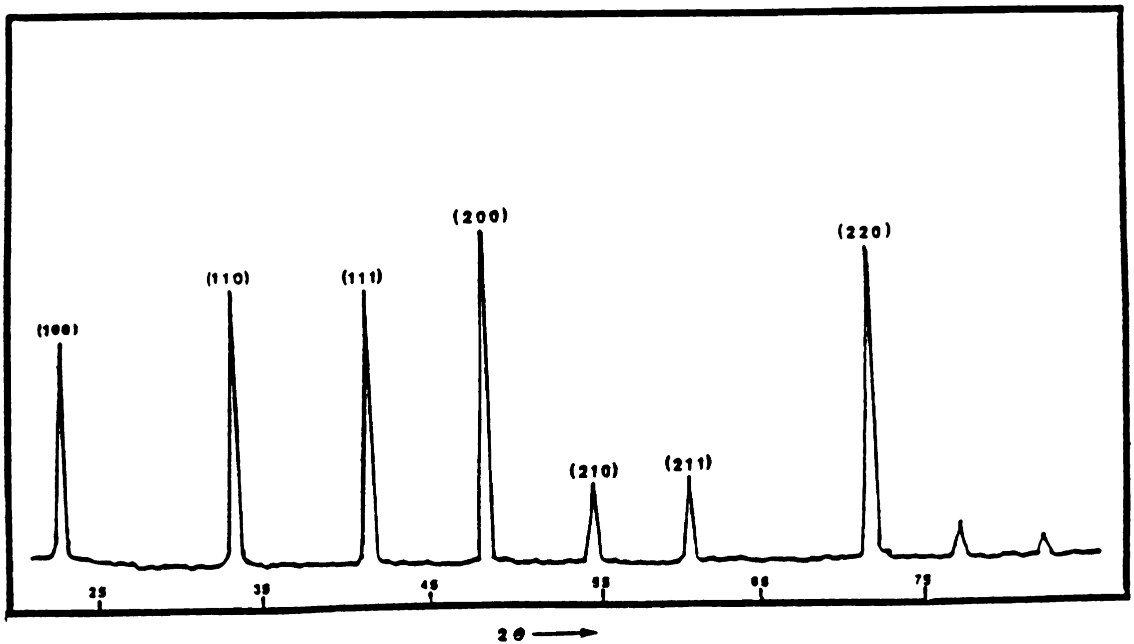

Figure 2.5

X-ray Diffraction Pattern of Ordered $Cu_{0.8}Pt$ Alloy

ELECTRON DIFFRACTION

The HB 501 FE-STEM analytical electron microscope used in this study is capable of producing electron diffraction images of the sample. Using this feature, it is possible to study the crystal structure of the sample on length scales that are unattainable with X-ray diffraction techniques. A well collimated X-ray beam on a modern diffractometer is about 2 mm in diameter. In the θ-2θ reflection geometry, this X-ray beam is projected onto the sample at an angle θ increasing the 'footprint' of the beam by the factor $(\sin\theta)^{-1}$. Hence, the region of the sample probed by the X-ray beam is a few mm across. In contrast, in electron diffraction, the region probed is determined by size (cross-section) of the electron beam and the spreading of the beam within the sample. By a judicious use of the electron optics and the apertures, this may be increased to as much as 30 μm (Selected Area Diffraction) or reduced to as little as 30 nm (Micro-Diffraction). Thus, one can probe the local crystal structure and correlate this with structure dependent properties such as the dielectric function ($\varepsilon(\omega)$).

PRINCIPLES OF ELECTRON DIFFRACTION

Electron diffraction is similar to X-ray diffraction in that the Bragg equations describe the two processes. A collimated beam of monochromatic electrons of kinetic energy 100 KeV (de Broglie wavelength 0.037 A) are incident on the

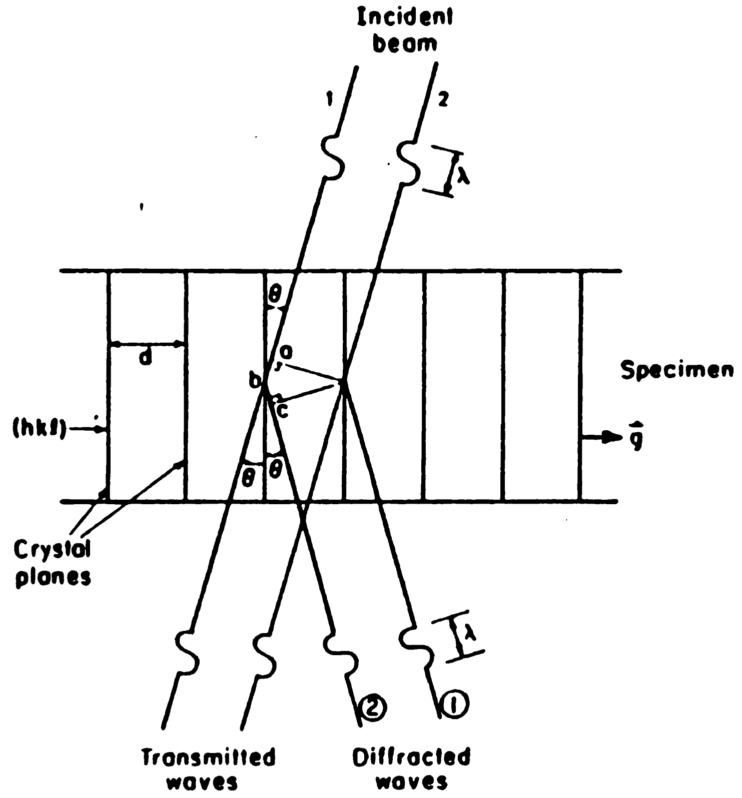

Figure 2.6

Electron Diffraction in Transmission Geometry sample. The electrons that are scattered at small angles ($<$ 2°) to the transmitted beam are focussed by the objective lens to form the diffraction pattern at the back focal plane. With L as the distance between the sample and the detector plane we have the following expression for the spacing d of the atomic planes responsible for the reflection [2.5, 2.6, 2.7].

$$d = \frac{\lambda L}{R}$$

Here, R is the distance between the undeviated beam and the diffraction spot in the detector plane.

A polycrystalline sample consists of many small crystallites of random orientations. Each of these crystallites--being a single crystal of finite size--diffract the incident electron beam to produce Bragg reflections in various directions θ_{hkl} (relative to the incident beam direction) subject to the condition

$$2d_{hkl} \sin\theta_{hkl} = n\lambda$$

Here, d_{hkl} is the spacing between the atomic planes of Miller indices hkl. The random orientation of crystallites in the sample results in a diffraction pattern that is axially symmetric (about the incident electron beam direction). Thus, discrete diffraction spots of many crystallites merge to form a ring. Such diffraction rings are formed only if the incident electron beam illuminates a large number of randomly oriented crystallites (i.e., the crystallites are small in size compared to the beam spread).

The sharpness of the diffraction rings (or spots) conveys information about the average size of the crystallites. The sharpness of a diffraction ring is determined by the number of atomic planes of a given index hkl participating in that Bragg reflection and is proportional to the quantity $\sin^2 Nn/\sin^2 x$, N being the number of planes participating in that Bragg reflection. In a large single crystal, the number N can be large resulting in very sharp diffraction spots. As the size of the crystallite (and the number of crystal planes of a given index) decreases, the corresponding diffraction spot gets broader and less defined. In an amorphous solid, the broad diffraction peaks correspond to the nearest neighbor and next-nearest neighbor distances. In a limited sense, these diffraction patterns may be thought of as the Radial Distribution Functions (RDF) of the solid in the reciprocal space.

Electrons of energy 100 KeV (de Broglie wavelength 0.037 A) were used for electron diffraction in this study. The wavelength of Cu-K_α X-rays used elsewhere in this study was 1.54 A. The scattering angle ($\sin\theta$) of a given Bragg reflection is directly proportional to the wavelength used; hence, the electron diffraction patterns were of lower resolution compared to the diffraction patterns produced

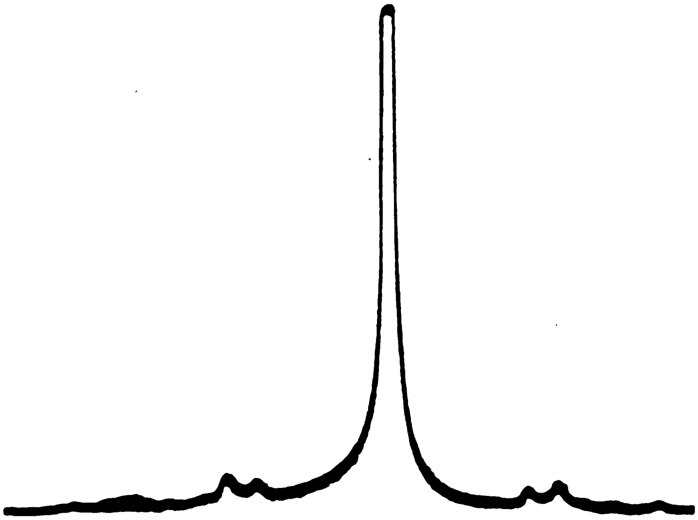

Figure 2.7

Selected Area Diffraction of Layered NiTi System

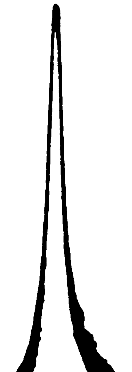

Figure 2.8

Selected Area Diffraction of Laser Quenched Alloy

using Cu_α X-rays. The electron diffraction patterns were unsuitable for quantitative analysis (like determination of the long range order parameter). Instead, the electron diffraction patterns were used to classify the regions under study as either crystalline or amorphous.

The two diffraction (x-ray & electron) techniques were carried out in two different geometries. This introduced an important difference in the nature of information the two techniques yielded. X-ray diffraction was carried out in the reflection geometry and the electron diffraction in the transmission geometry. Thus, the x-ray diffraction yielded structural information in a direction $\perp^r$ to the sample's surface; and the electron diffraction yielded information on the in-plane structure. The samples studied by us were homogeneous and did not require special care in interpreting the results.

X-RAY MICROANALYSIS

The compositions of the various metallic systems studied were measured in the FE-STEM using the techniques of thin-film X-ray microanalysis [2.8, 2.9]. The use of high accelerating voltage (100 Kev) and thin samples in the analytical electron microscope enabled measurements of composition of regions of sample < 10 nm in diameter. This ability to measure local composition is very important since the electron energy loss measurements in this study are from regions < 10 nm in diameter. Information about the local crystal structure were obtained by using the micro-diffraction capability of the electron microscope.

When a beam of fast electrons hit a solid, electrons of the inner core levels of the atoms (of the solid) are knocked out. During the ensuing relaxation process, the atoms emit characteristic X-ray photons. These are the K, L, M--series X-rays with energies in the KeV range. An energy dispersive detector such as lithium drifted silicon [Si(Li)] is used to detect and quantitatively measure these X-ray photons. The output of the detector is digitized and stored in a multi-channel analyzer for quantitative analysis. See Figure 2.9 for the detector - sample geometry.

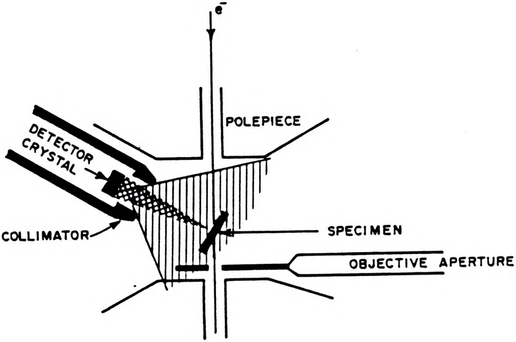

Figure 2.9

X-EDS Detector-sample Geometry

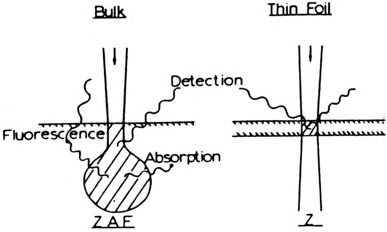

Figure 2.10

X-ray Emission from Thick and Thin Samples

PRINCIPLES OF THIN-FILM MICROANALYSIS:

The main advantage of the thin-film micro-analysis technique is that in most cases no absorption or fluorescence correction need be applied (see Figure 2.10). Several workers (2.9, 2.10, 2.11) have shown that in a homogeneous sample containing the elements A, B, C . . . the integrated intensity ratio of any two x-ray lines (I_A/I_B) is directly proportional to the concentration (by weight) ratio of the corresponding elements.

$$\frac{I_A}{I_B} = \frac{K_A e_A}{K_B e_B} \cdot \frac{C_A}{C_B} , \qquad K_A = \frac{Q w_A A_A}{W_A}$$

The quantities Q, w and A are the ionization cross-section X-ray fluorescence yield and the radiative branching ratio; W is the atomic weight, and e is the relative detector efficiency for the detected X-ray line. This equation may be rewritten as:

$$\frac{C_A}{C_B} = K_{BA} \frac{I_A}{I_B}$$

The factor K_{BA} may be computed from published data [2.9] or measured directly in a given AEM-Si(Li) detector combination. For the latter approach, one studies samples of known concentration and algebraically solves for KBA.

To be able to use the thin-film micro-analysis technique accurately, the two X-ray intensities must be measured simultaneously and the thin-film criterion must be

satisfied. For an alloy AB the thin-film criterion [2.10] is:

$$(\chi_A - \chi_B)\rho t < 0.2$$

where χ is the mass absorption factor, t is the thickness of the sample, and ρ is the concentration weighted average density of the sample. The thin-film criterion is not satisfied in many metallic AEM samples for thickness $t >$ 1500 A. The samples used in this study were thinner than 1000 A, as revealed by EELS measurements. The accuracy of the thin-film micro-analysis technique is in the 5% - 10% range. For higher accuracies, "k-factors" computed from standard thin-film samples of known composition are needed.

A typical x-ray energy dispersive spectrum is shown in Figure 2.11 for the Cu_3Pt ordered alloy.

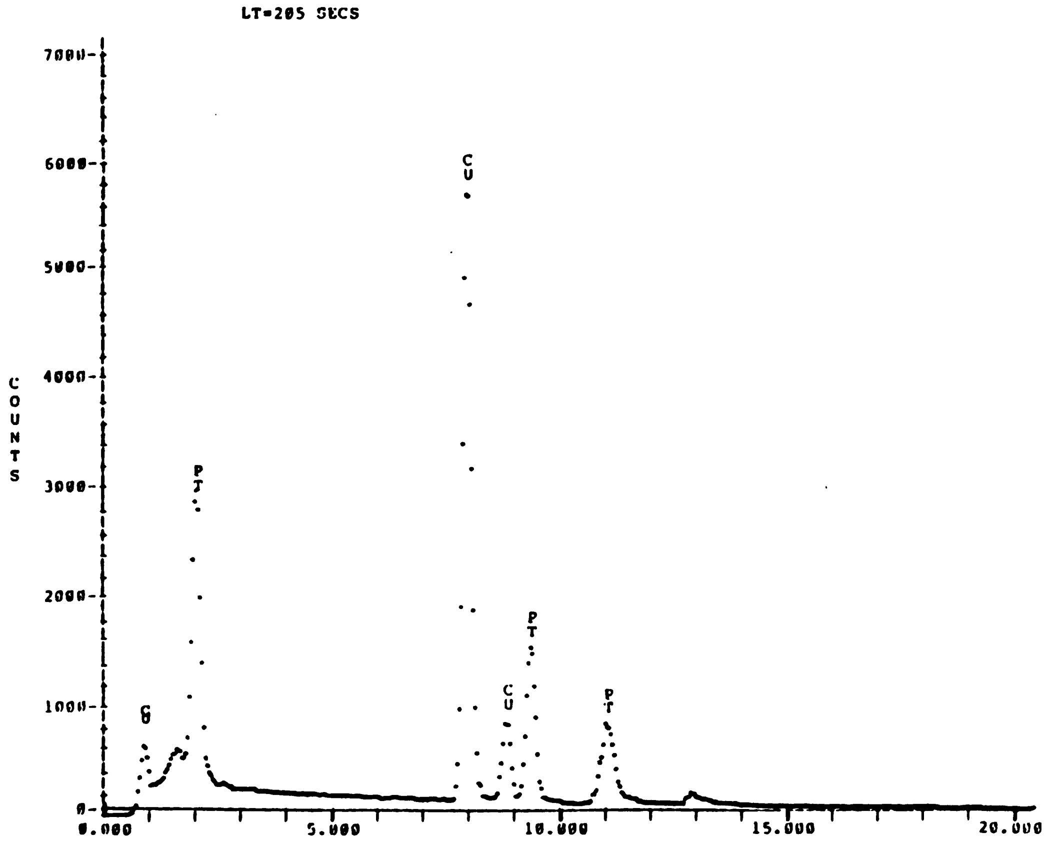

Figure 2.11

X-EDS of Cu_3Pt Alloy

MEASUREMENT OF ELECTRONIC PROPERTIES

In this study of the order-disorder effects on the optical/electronic properties of metallic systems we chose the following two techniques to measure the electronic properties:

1. Electron Energy Loss Spectroscopy (EELS)
2. Optical Reflection Spectroscopy

The EELS measurements were carried out in the electron energy loss range (electronic excitation energy range) 5 eV to 90 eV in the Vacuum Generators HB 501 FE-STEM of the MSU Analytical Electron Microscopy Lab. The optical reflectivity spectra were obtained using a measurement facility developed by us on a NSF equipment grant. The following two sections describe these two techniques in detail.

ELECTRON ENERGY LOSS SPECTROSCOPY

Electron Energy Loss Spectroscopy (EELS) is the study of momentum and energy distribution of electrons that have interacted with a solid [2.6]. This is a powerful micro-analytical tool to study various electron excitations in a solid. The incident electrons interact with the electrons in the solid through electromagnetic interaction; hence, EELS provides us with a method to study quantitatively the bulk dielectric function of the solid. A brief description of this technique is given below.

Consider a beam of fast electrons of energy E_0 (100 KeV, for example) and intensity I_0 incident on a thin (<1000 A) sample. A large fraction of these electrons go through without interacting with the sample. The rest are elastically and inelastically scattered. The energy and momentum distributions of these scattered electrons yield information about the solid under investigation. The scattered electrons are detected over a solid angle $d\Omega$ in the direction (θ,ϕ). An energy analyzer is used to collect the energy spectrum. See Figure 2.12 for a schematic of the electron energy loss measurement process in the transmission geometry.

The energy loss intensity $I(E,\theta)$ for single interactions is given by [2.12, 2.13]:

$$\frac{I(E,\theta)}{I_0} = N \cdot \frac{d^2\sigma(E,\theta)}{dEd\Omega}$$

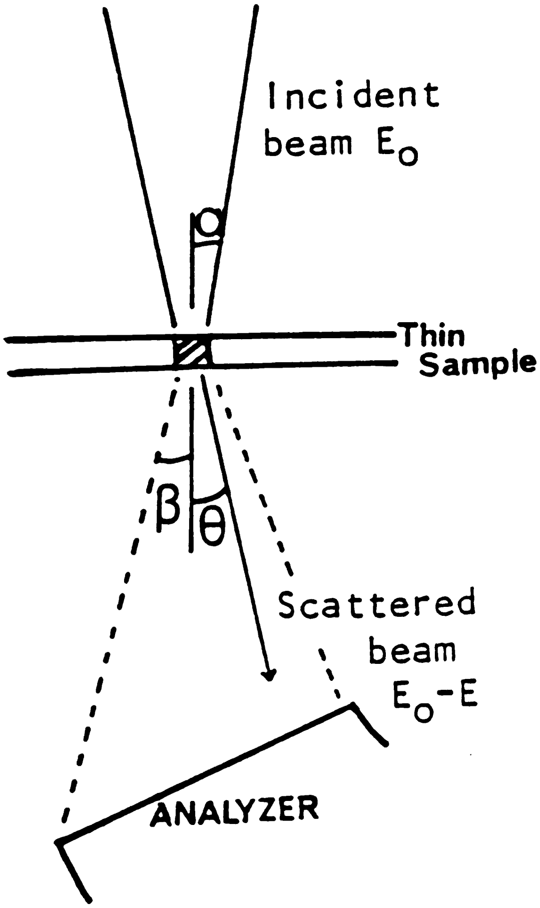

Figure 2.12

Transmission EELS in an AEM

where $d^2\sigma/dEd\Omega$ is the differential scattering cross-section for an electron in the direction θ and with an energy loss E. N is the number of atoms/unit area in the volume of the sample examined. The differential scattering cross-section is related to the macroscopic dielectric function $\varepsilon(\omega)$ as shown below [2.12, 2.13]:

$$\frac{d^2\sigma(E,\theta)}{dEd\Omega} = \frac{\mathrm{Im}\ (-1/\varepsilon(\omega))}{2\pi^2 a_0 n E_0} \cdot \frac{1}{\theta^2 = \theta_E^2}$$

Here, θ_E is the characteristic scattering angle defined by:

$$\theta_E = \frac{E}{2E_0} \qquad E << E_0$$

Thus for a fixed θ, we find that the energy loss probability is directly propositional to the imaginary part of the loss function, $-1/\varepsilon(\omega)$. Optical measurements, on the other hand are proportional to $\varepsilon 2$, the imaginary part of $\varepsilon(\omega)$. The difference is due to the fact that the electrons in the solid respond to a transverse electromagnetic field in optical measurements and to a longitudinal electrical field in the case of electron energy loss experiments. By the same argument, optical experiments measure ε_{trans} and EELS measure ε_{long}; but detailed studies indicate that these two functions agree very well [2.14].

A typical energy loss spectrum has many features depending on the types of excitations present in the solid [2.14, 2.12, 2.13]. Commonly occurring excitations are interband transitions, collective oscillations and core excitations.

The low energy end of the spectrum is dominated by the zero loss peak, the electrons that have lost little or no energy in traversing the solid. In addition to this, one may find features that are due to interband transitions and collective excitations (plasma oscillations). Both direct and indirect interband transitions can occur. Volume and surface plasma oscillations are the collective oscillations that occur in this energy range. The volume plasmons are oscillations in the electron charge density setup by the electric fields of the incident electrons. The energy Ep of the volume plasmon is a function of the electron density N (number/volume). The exact relationship is [2.13, 2.14, 2.15].:

$$E_p = \hbar \left(\frac{4\pi N e^2}{m_e}\right)^{\frac{1}{2}}$$

where m_e is the (effective) mass of the electrons. This energy E_p is determined by the condition $\varepsilon(\omega) = 0$ at the plasma frequency. For a vacuum-metal interface the surface plasmons oscillations occur at the energy E_s [2.14],

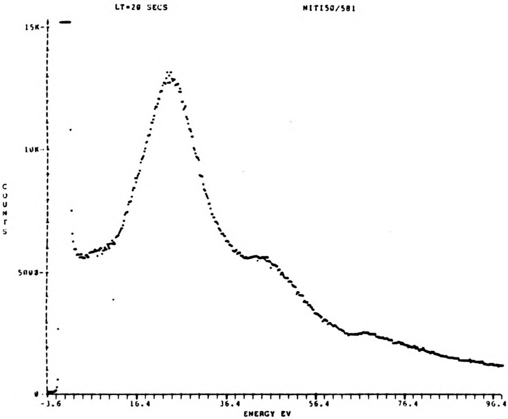

Figure 2.13

EELS of NiTi Alloy

$$E_s = \frac{E_p}{\sqrt{2}} \quad , \quad \text{with } \varepsilon_{vac} = 1$$

For a system of free-electrons with very little scattering, the volume plasmons would show up as a sharp peak at Ep is the loss spectrum. In a real metal, this peak is broadened by the different scattering mechanisms present. Shifts in the location of this peak are possible due to changes in the electron density and the effective mass [2.14]. For most metals and alloys the collective excitations can be found below 35ev.

For energy losses above 35ev, a different physical process is responsible. This is the excitation of a core electron of an atom to the continuum [2.12, 2.13]. These excitations are sensitive to the local chemical composition and atomic environment, and this is exploited in techniques such as EXAFS [2.16].

MEASUREMENT OF OPTICAL REFLECTIVITY

Band structure investigation of various elements and alloys using optical spectroscopic methods is well established. Some of these methods are photoemission spectroscopy (PES, XPS, UPS), ellipsometry and optical reflection spectroscopy. These techniques provide much needed information about the conduction and valence bands Density of States (DOS). In this study, we measured the total reflectivity of the samples in the photon energy range 1 eV to 5 eV. These measurements complement the electron energy loss measurements.

The total (specular and diffuse) optical reflectivity of the various alloys were measured using a facility developed at MSU. This facility consists of a light source (IR and UV-VIS), a monochromator, an integrating sphere, a detector and associated electronics. See Figure 2.14 for a schematic of this facility.

The heart of this facility is a 15 cm diameter integrating sphere made by Labsphere. The inner surface of the sphere is coated with a highly reflective material (barium oxide). The reflectivity of this material is accurately known over the energy range measured. Measurements of the absolute reflectivities of samples were avoided; instead, the sample's reflectivity was compared to that of a reference coated with barium oxide. Moreover the use of an integrating sphere made possible the measurement

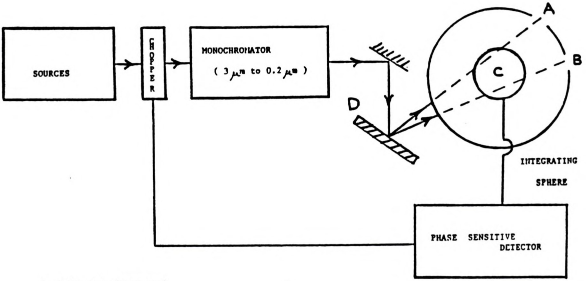

A: Reference mirror port

B: Sample port

C: Detectors (PbS cell or PMT)

D: Vibrating mirror

Figure 2.14

Layout of Optical Reflectivity Measurement Systems

of the total reflectivity without extensive efforts to prepare the surface of the sample. The reflectivity measurements were made at near normal (~ 4°) incidence. The relative location of the inlet and detector ports were such that the detector only measured the uniform light level setup by multiple scattering off the sphere wall.

Optical reflectivity measurements over the photon energy range 0.6 eV to 5.5 eV was possible. Two different light sources were used to accomplish this. A 150 W xenon arc lamp for the range 1.0 eV to 5.5 eV and a IR lamp for the range 0.6 eV to 1.0 eV. The lamps were operated by stabilized power supplies. Though reflectivity measurements in the photon energy range 0.6 eV to 5.5 eV were possible, noise considerations limited the range to 1 eV to 5.0 eV.

A SPEX MINIMATE monochromator was for wavelength selection. This monochromator incorporates a diffraction grating in the Czerney-Turner mount. A microprocessor controlled stepper motor drive ensured wavelength selection to within 1 nm. Three gratings were used -a 600 lines/mm 1250 nm blazed grating for the range 700 nm to 2000 nm (1.7 eV to 0.6 eV), a 1200 lines/mm 500 nm blazed grating for the range 400 nm to 700 nm (4 eV to 1.8 eV) and a 1200 lines/mm 250 nm blazed grating for the range 250nm to 400 nm (5.5 eV to 4.0 eV). Two order sorting filters (pass bands 400 nm to 1200 nm and 700nm to 1200 nm) were used to eliminate unwanted higher orders. The detectors used were a

photomultiplier and a PbS cell. The photomultiplier, with its quartz envelope had good sensitivity in the UV and visible spectrum. The PbS cell served as the IR detector. The incident light was chopped at about 200 Hz and the output of the detector at this frequency was measured using a lock-in amplifier. The incident light could be switched from the sample to the reference with help of a scanning mirror. Thus, one could see the intensities of light reflected by the sample or the reference. The ratio of these two intensities is the reflectivity of the sample. To obtain the absolute reflectivity this has to be corrected for the actual reflectivity of the reference.

Pure metallic samples of known reflectivities such as Cu,Au, Pt and Ag were measured to check the accuracy of the system. The results obtained were within 5% of the published results. Hence, the error associated with the measurements obtained with our system was taken to be 5%.

CHAPTER 3

Optical Properties of Ordered and Disordered $Cu_{1-x}Pt_x$

Many metallic alloys exhibit generalized order-disorder transitions with attendant changes in electronic and optical properties. Elsewhere in this dissertation, we have described the effects of topological disorder on electronic and optical properties. In this chapter an experimental study of the effects of atomic order-disorder transitions on electronic structures is described. In alloy systems where the constituent elements are very similar in their electronic structure (configuration), atomic order-disorder transitions produce minor perturbations in electronic levels of the alloys. The noble elements Cu and Au form a series of stoichiometric alloys that show very small changes in the properties due to order-disorder transitions. Apart from showing weak structures the reflectivity of ordered Cu_3Au differs by less than 3% from the reflectivity of the disordered phase [3.1].

The transition metal--noble metal alloy $Cu_{1-x}Pt_x$ was chosen for study in this investigation. The alloy was available in the ordered and disordered phases for x = 0.175, 0.20 and 0.25. For Pt compositions below 10%

(n = 0.10, 0.08, 0.06, 0.04 and 0.02) the alloy was available as cast (disordered).

The systems Cu-Au, Cu-Pd and Cu-Pt are specially suited for investigating the effects of atomic order-disorder transitions because the order-disorder transitions occur over a range of compositions. For example, the alloy system $Cu_{1-x}Pt_x$ exhibits ordered phases [3.2] for x near 0.25, 0.50 and 0.75. For x near 0.25, the structure of the disordered phase is the FCC Crystal with each lattice site occupied by an 'average' atom ((1-x) Cu + x Pt). In the ordered phase the Pt atoms occupy the cube-corners and the Cu atoms occupy the face centers of the FCC lattice. This selective occupation of the lattice sites by atoms of different species leads to extra Bragg lines in the X-ray diffraction pattern called 'Super lattice' lines [3.3]. The effect of ordering can also be seen by constructing reciprocal lattices of the ordered and disordered phases. For the ordered phases, there are extra Brillouin planes in the reciprocal K-space [3.4]. The presence of these extra planes are a potential source for structure in the optical properties. Figure 3.1 depicts the Wigner-Seitz cell for the FCC lattice with a cubic superlattice inscribed. We will refer to Figure 3.1 and discuss the origin of extra structures in the optical properties later in this chapter.

The systems Cu-Au, Cu-Pd and Cu-Pt offer a few other advantages for the study of order-disorder transitions and (n = 0.10, 0.08, 0.06, 0.04 and 0.02) the alloy was available as cast (disordered).

The systems Cu-Au, Cu-Pd and Cu-Pt are specially suited for investigating the effects of atomic order-disorder transitions because the order-disorder transitions occur over a range of compositions. For example, the alloy system $Cu_{1-x}Pt_x$ exhibits ordered phases [3.2] for x near 0.25, 0.50 and 0.75. For x near 0.25, the structure of the disordered phase is the FCC Crystal with each lattice site occupied by an 'average' atom ((1-x) Cu + x Pt). In the ordered phase the Pt atoms occupy the cube-corners and the Cu atoms occupy the face centers of the FCC lattice. This selective occupation of the lattice sites by atoms of different species leads to extra Bragg lines in the X-ray diffraction pattern called 'Super lattice' lines [3.3]. The effect of ordering can also be seen by constructing reciprocal lattices of the ordered and disordered phases. For the ordered phases, there are extra Brillouin planes in the reciprocal K-space [3.4]. The presence of these extra planes are a potential source for structure in the optical properties. Figure 3.1 depicts the Wigner-Seitz cell for the FCC lattice with a cubic superlattice inscribed. We will refer to Figure 3.1 and discuss the origin of extra structures in the optical properties later in this chapter.

The systems Cu-Au, Cu-Pd and Cu-Pt offer a few other advantages for the study of order-disorder transitions and

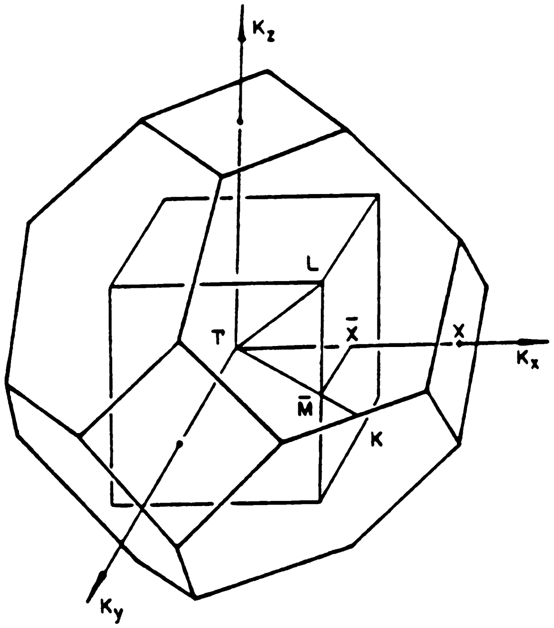

Figure 3.1

Wigner Seitz Cells of Face Centered and Simple Cubic Unit Cells their effect on the optical properties. In these systems, the order-disorder transitions are not accompanied by a large change in the crystal structure or the lattice constant. In Cu_3Au and Cu_3Pt the change in the lattice constant is less than 1%. These systems are also free from the complications of magnetic effects. That the Cu-Au system has been a prototype for order-disorder studies should come as no surprise.

There are some important differences between the Cu-Au and the Cu-Pt and Cu-Pd systems. The elements Cu and Au belong to the noble elements group and have similar electronic structure. These two elements have 11 outer electrons in the configuration $d^{10}s^1$. The noble metals (Cu, Au and Ag) are characterized by a sharp absorption edge in their optical reflectivity spectra. This sharp edge is caused by the onset of interband transitions and for Cu and Au this edge occurs at about 2 eV and 2.6 eV respectively; for Ag this edge is at about 4.0 eV. Below this edge, the reflectivity is very high (almost 1.0). This accounts for the characteristic colors of Cu, Au and Ag.

The elements Pt and Pd are transition metals. They have a total of 10 outer electrons. Their electronic structure is $d^{10-n}s^n$. In contrast with the d-bands of the noble metals which do not cross the Fermi level, the d-bands of these elements cross the Fermi level. Interband transitions from the occupied d-levels start at very low energies.

Investigations of the electronic and optical properties were carried out using electron energy loss spectroscopy (EELS) and optical reflection spectroscopy. Other analytical techniques employed were X-ray diffraction and electron diffraction for structure determination and X-ray energy dispersive spectroscopy (X-ray EDS) for composition analysis. These techniques are discussed in detail in Chapter 2.

SAMPLE PREPARATION:

Samples of $Cu_{1-x}Pt_x$ atomically ordered (denoted 'G') and disordered ('U') in the Pt concentration range $0.175 \leq x \leq 0.25$ were supplied to us by E. W. Collings of the Battelle Memorial Institute. A measurement of the long range order (LRO) parameter by X-ray diffraction revealed that the LRO parameter of the ordered (G) phase was between 0.65 and 0.75 for the 3 compositions ($x = 0.175$, 0.20 and 0.25), studied. Atomically disordered samples made by quenching the alloy melt showed no superlattice Bragg lines in the diffraction pattern.

Thin sheets (about 200 μm) of the sample were prepared for the reflectivity measurements by etching them in 15% KCN solution. A potential difference of 5 Vac was used for this electro-chemical process. This procedure yielded surfaces that were free of scratches and other surface damage.

After optical reflectivity measurements, 3 mm dia. discs were cut from the sample and mechanically polished to a final thickness of about 30 μm. Using a South-Bay jet-etching unit and a 15% KCN solution, these discs were etched. This procedure produced perforations in the middle of the discs. Regions around the perforations were thin enough (< 1000 A) to transmit the high energy electrons of the electron microscope.

RESULTS AND DISCUSSION:

Measurements of the optical reflectivities (1.0 eV to 5.0 eV) and the EELS were done for the phases (G) and (U) for Pt concentrations of 17.5%, 20% and 25%. For lower Pt concentrations (below 10%), the alloy exists in the disordered phase; reflectivity measurements alone were carried out on these samples. Figures 3.2 - 3.11 display the results of the reflectivity measurements.

For low Pt concentrations, the absorption edge at 2 eV in pure Cu is well preserved, though diminished in magnitude. No measurable shift in the position (2 eV) of the edge is observed. The magnitude of the drop in R decreases as the Pt concentration increases. By about 10% Pt, the edge has completely disappeared. For Pt concentrations of 17.5% and above the R(ω) spectra resembles that of pure Pt. The reflectivity of the ordered phases is consistently below that of the disordered phase, in the energy range 1.0 eV to 5.0 eV. Apart from this difference,

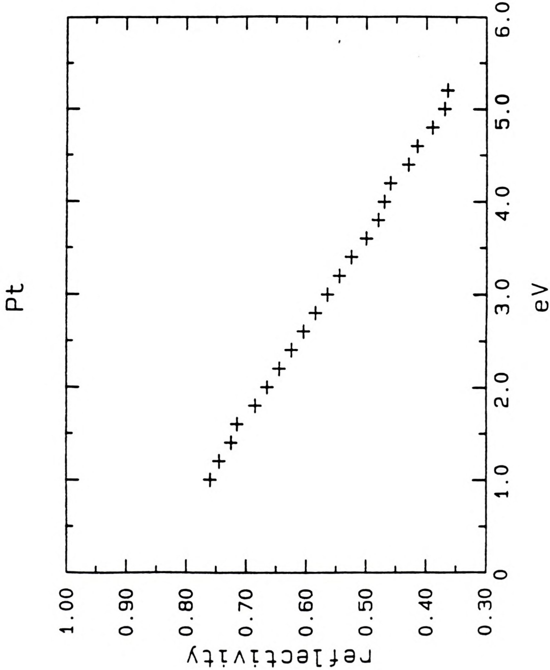

Figure 3.2

Reflectivity of Pt

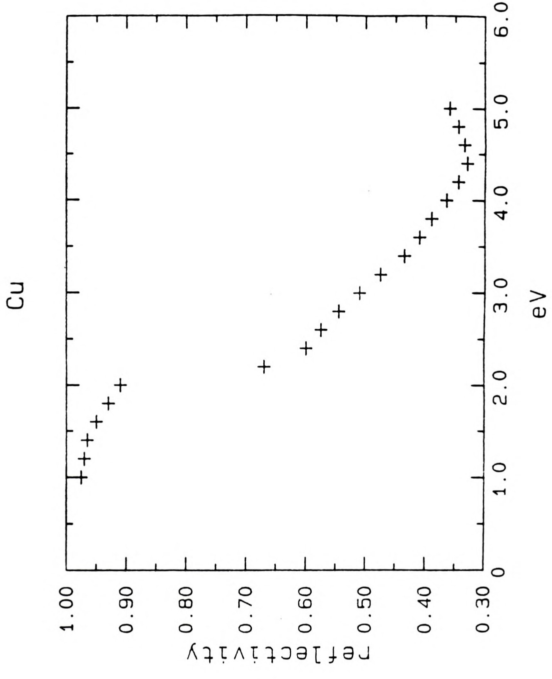

Figure 3.3

Reflectivity of Cu

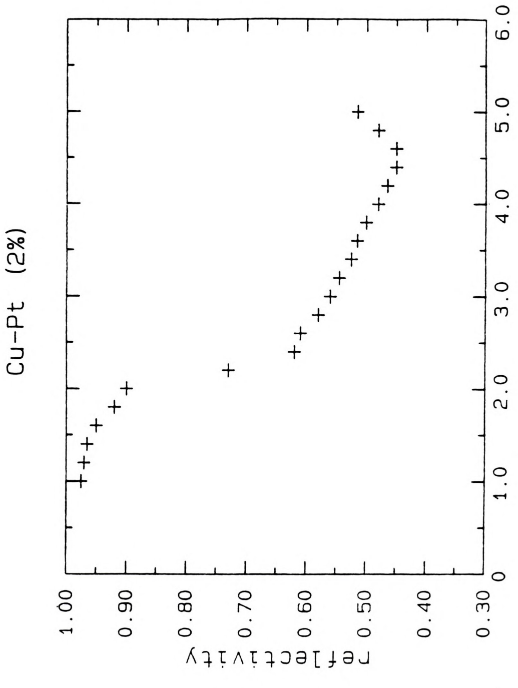

Figure 3.4

Reflectivity of $Cu_{0.98}Pt_{0.02}$

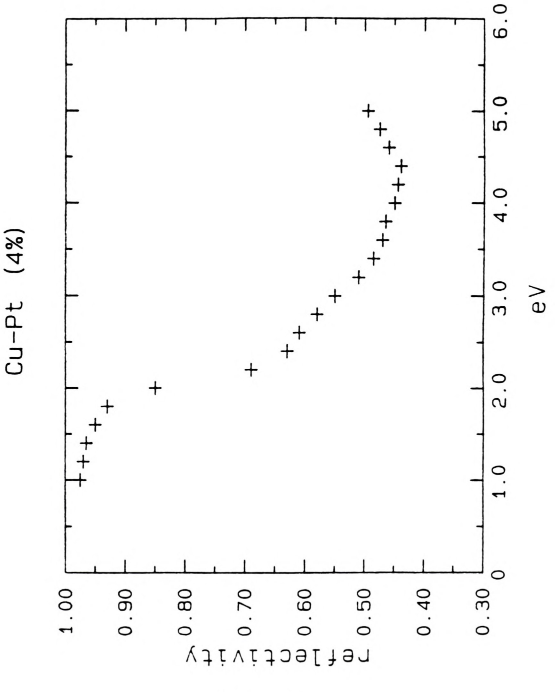

Figure 3.5

Reflectivity of $Cu_{0.96}Pt_{0.04}$

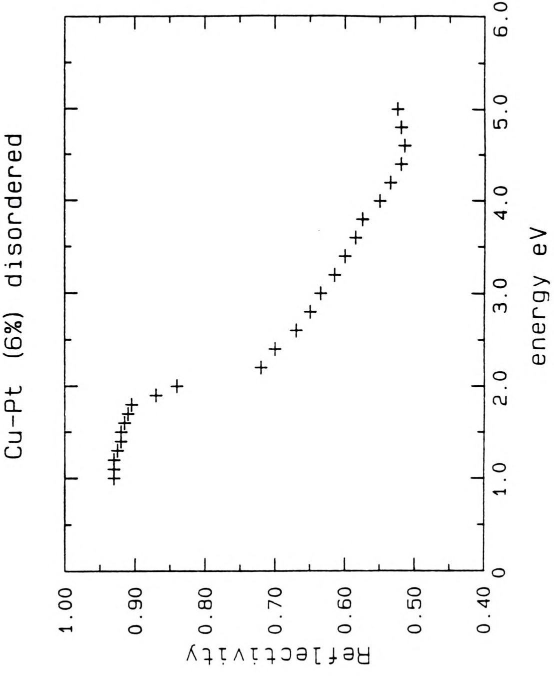

Figure 3.6

Reflectivity of $Cu_{0.94}Pt_{0.06}$

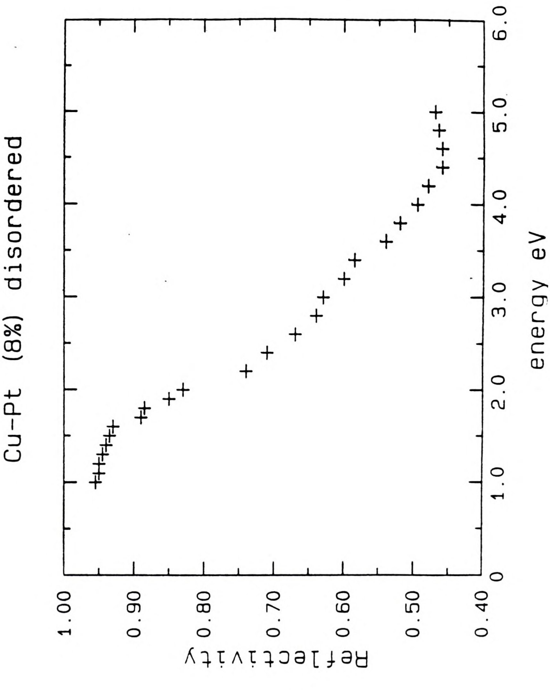

Figure 3.7

Reflectivity of $Cu_{0.92}Pt_{0.08}$

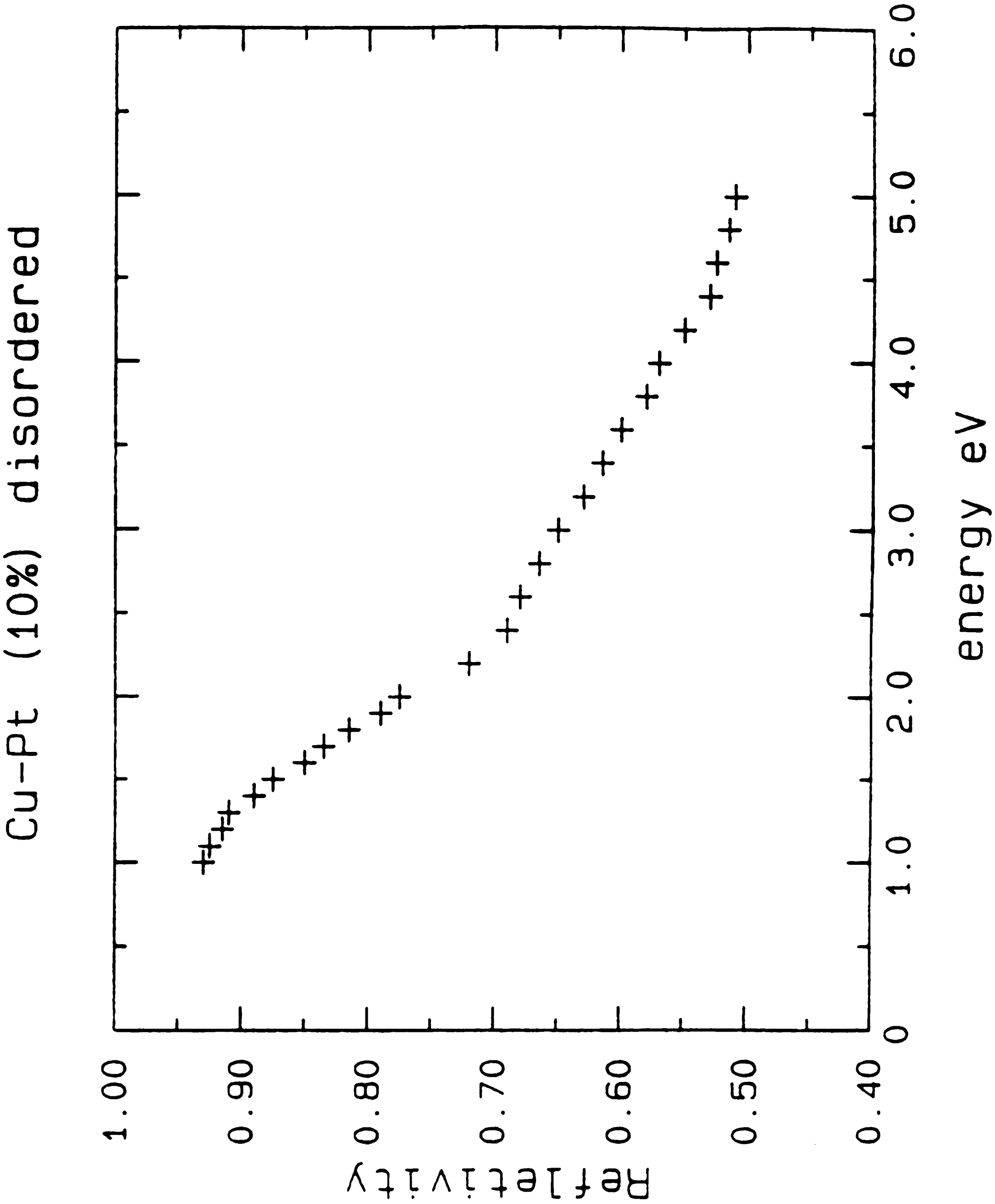

Figure 3.8

Reflectivity of $Cu_{0.90}Pt_{0.10}$

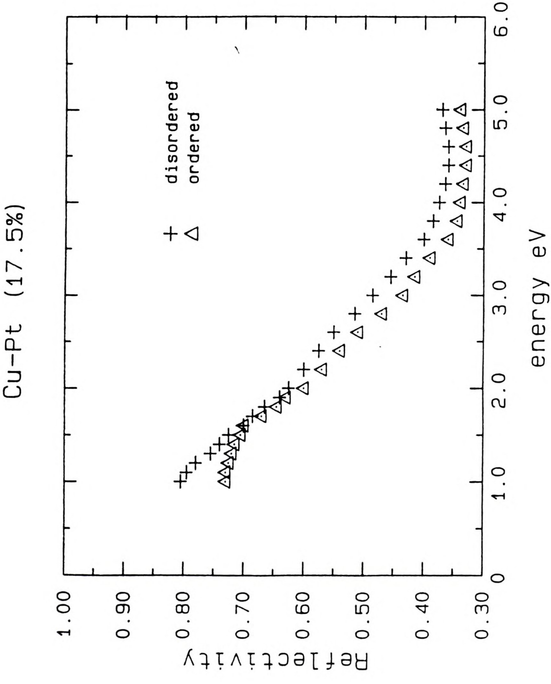

Figure 3.9

Reflectivities of Ordered and Disordered $Cu_{82.5}Pt_{17.5}$

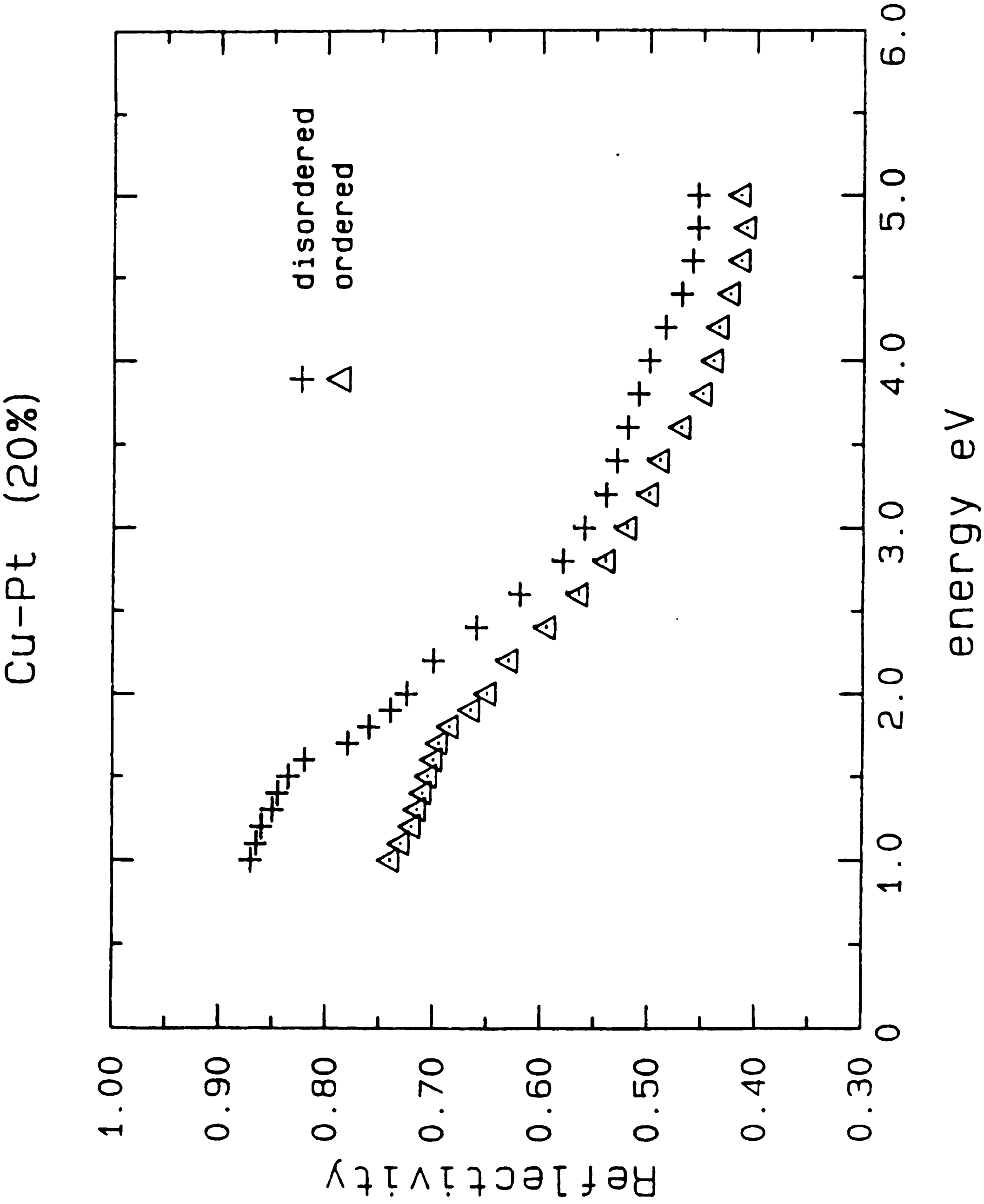

Figure 3.10

Reflectivities of Ordered and Disordered $Cu_{80}Pt_{20}$

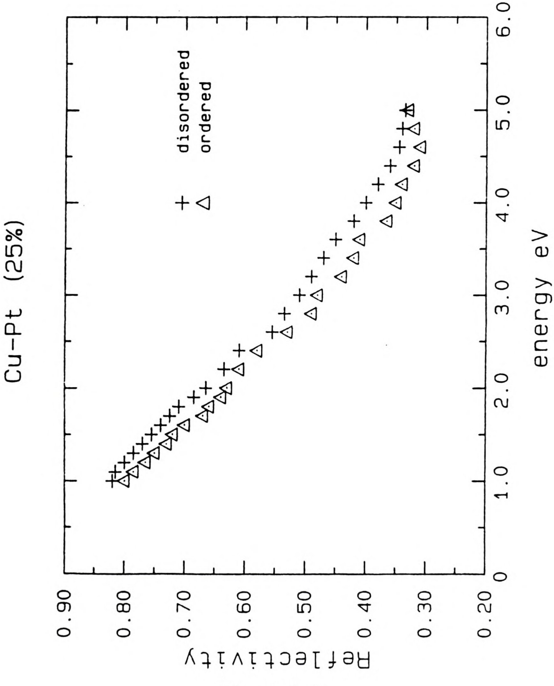

Figure 3.11

Reflectivities of Ordered and Disordered $Cu_{75}Pt_{25}$

there are no significant differences in R(ω) of the two phases. The error associated with these reflectivity measurements is about 3%.

Turning our attention to the R(ω) spectra for low Pt concentrations (10% and below) alloys, we find that R(ω) below the edge (at 2 eV) is high, but lower than that of pure Cu. This should be expected because the addition of Pt impurities introduces electron states between the top of Cu d-bands and the Fermi level. Whether these are due to truly localized virtual bound states as suggested by Friedel [3.5] or a lowering of the Fermi level relative to the Cu d-bands by a decrease in the electron density (number/volume) is a question that must be addressed.

Measurements of the transmission and reflection coefficients in thin films of $Cu_{1-x}Pd_x$ for low Pd concentrations have been made by H. P. Myers et al [3.7]. They have also studied AgPd and AuPd films. The optical absorption coefficients computed from these films clearly indicate the presence of extra peaks (relatively broad) in $Ag_{1-x}Pd_x$ and $Au_{1-x}Pd_x$ ($x < 0.40$). In $Ag_{1-x}Pd_x$ this peak occurs at about 2.6 eV (below the 3.8 eV absorption edge of Ag); in $Au_{1-x}Pd_x$ this peak occurs at about 2.0 eV, still below the absorption edge of Au. These extra peaks in ε_2/λ of AgPd and AuPd are attributed to the formation of virtual bound states at Pd sites; these states have energies that are above that of the d-bands of the host but below E_F. In

$Cu_{1-x}Pd_x$ these peaks are not resolved, probably due to copper's own strong peak at 2 eV. It is reasonable to expect a similar behavior in the $Cu_{1-x}Pt_x$ alloys.

In the $R(\omega)$ of $Cu_{1-x}Pt_x$ alloys, the absorption edge stays at 2 eV as the Pt concentration is increased. That the edge does not shift to lower energies is a strong argument against the rigid-band picture of the alloying process. The rigid band model suggests that when Pt (10 valence electrons/atom) is added to a Cu matrix, there is a reduction in the electron density. Thus the Fermi energy, determined mainly by the electron density, would decrease and lead to the onset of interband transitions (top of filled d-bands to states just above E_F) at energies below the 2 eV threshold seen in these alloys. These reflectivities measurements may indeed be indirect evidences of the formation of virtual bound states in dilute Cu-Pt alloys. Rao et.al.[3.12] have calculated the band structure of copper rich Cu-Pd alloys and also conducted angle resolved photoemission studies on these alloys. Their studies show clearly the formation of two Pd derived bands at 1.7 eV and 5.0 eV. Figure 3.12 shows the results of their investigations.

We now turn to a discussion of the expected order-disorder effects on the optical properties. The reciprocal lattice of the ordered Cu_3Pt phase is different from that of the disordered phase. This is due to the extra

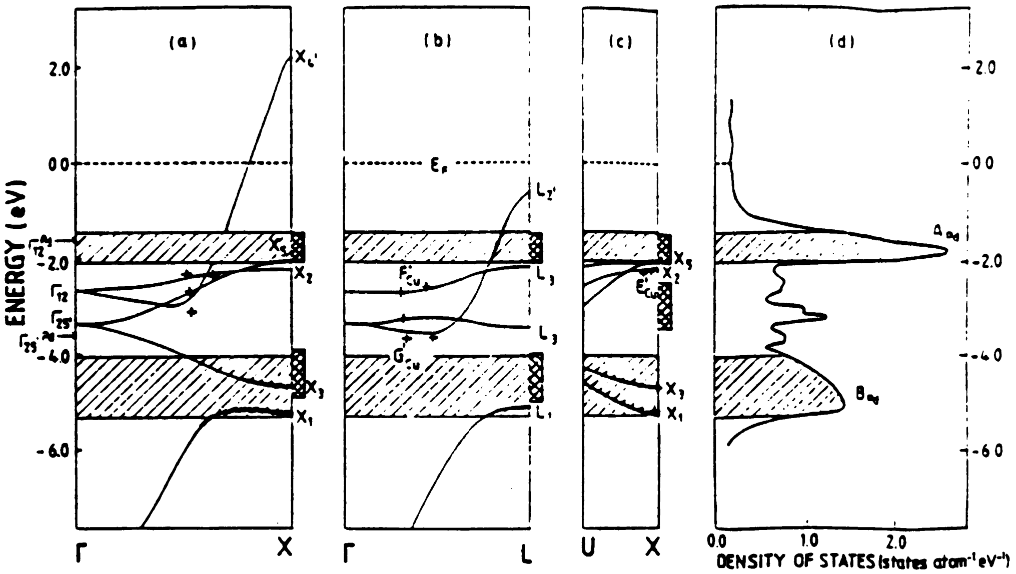

$Cu_{95}Pd_5$

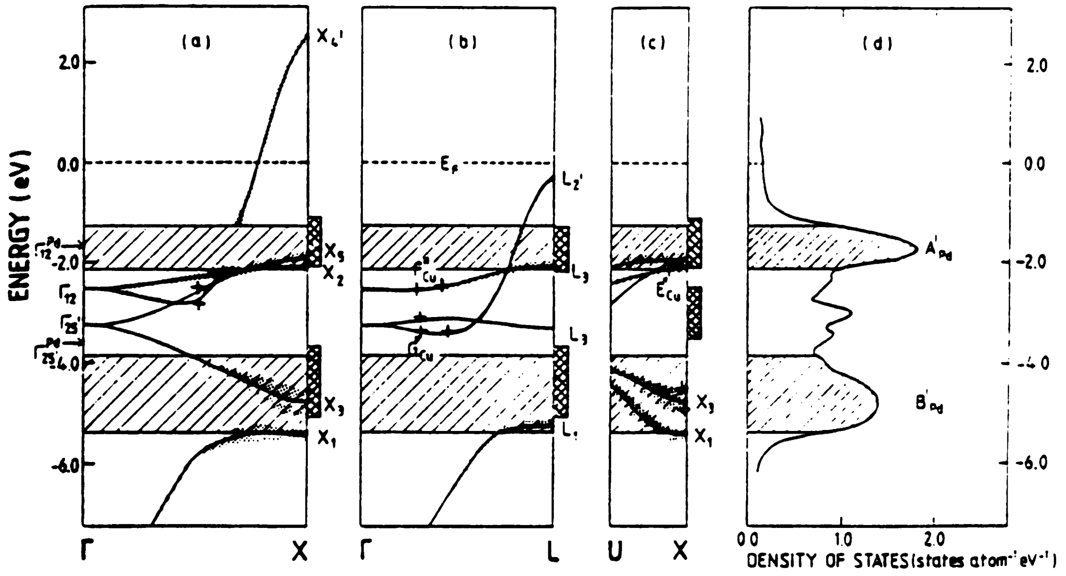

$Cu_{85}Pd_{15}$

Figure 3.12

Band Structures of Cu Rich Cu-Pd Alloys

superlattice symmetry present in the ordered crystal. This can be visualized by inscribing the Wigner-Seitz cell of a simple cubic lattice with the Wigner-Seitz cell of the FCC lattice (see Figure 3.1). The faces of the cubic cell intersect the Brillouin zone in many k-directions. For example, in the Γ-X direction of the 1st Brillouin zone of the FCC lattice is bisected by a face of the cubic Wigner-Seitz cell. Thus the points between this face and the symmetry point X are 'folded' into the cube; the point X is now at Γ. Similar band folding along other directions are possible. Many sub-bands are thus formed for the original bands. This formation of extra bands (states) will change the DOS at these energies. Many more interband transitions are now possible resulting in new structures in the reflectivity spectra. The changes in the DOS is such that the total number of states (area under the DOS curve) does not change. A mere redistribution of the states at various energies occurs [3.11]. Differential reflectogram studies on ordered and disordered Cu_3Au by R. E. Hummel [3.1] show structures at 2.17 eV and 3.85 eV due to 'band folding'.

In the disordered phase of Cu_3Pt, an entirely different set of energy absorption mechanisms are possible. The translational symmetry of the lattice of the ordered phase requires the conservation of crystal momentum, in addition to energy, in electronic transitions. For transitions induced by the absorption of a low energy

photon, only direct transitions are possible. This is due to the fact that the incident photon has a very small momentum (= $2\pi/\lambda$) compared to the dimensions of the Brillouin zone. The K-conservation requirement limits the number of transitions that can be induced by a photon of energy $\hbar\omega$. In the disordered phase, the translational symmetry of the lattice is reduced to that of an FCC lattice by random occupation of the lattice sites by Cu and Pt atoms and the K-conservation requirement is relaxed [3.11]. The disordered phase differs from an ideal FCC lattice due to the presence of an extra (Pt - Cu) potential at the Pt sites and the scattering due to this potential.

The process just described and the increased absorption due to 'band-folding' in the ordered phase result in a decrease in the optical reflectivity. Without the aid of accurate E(K) calculations, it is not possible to predict which of the two absorption processes results in a larger reduction in the reflectivity. Our experimental measurements, however, suggest that the effects of band-folding seem to be relatively stronger. The $R(\omega)$ of the ordered phase for Pt concentrations 17.5%, 20% and 25% are consistently lower than the $R(\omega)$ of the disordered phase. Hummel has observed similar effects ($R_{order}(\omega) < R_{disorder}(\omega)$) in Cu_3Au alloys [3.1].

In addition to optical reflectivity measurements, the transmission EELS of the ordered and disordered phases (Pt

concentrations of 17.5%, 20% and 25%) were measured. The results are displayed in Figures 3.13 - 3.20. We also measured the EELS of pure Cu and Pt. The spectra shown are the raw spectra, before the removal of double losses.

Some of the prominent features in the EELS of $Cu_{1-x}Pt_x$ alloys are those at about 5.0 eV, 8-12 eV, 20 eV and 27-30 eV. The accuracy and resolution associated with these measurements are ±1.0 eV and 1.0 eV respectively. Though there is a superficial resemblance between the EELS of Cu and the alloys, the EELS of Cu has many sharp features not found in the spectra of the alloys. For example, in the spectrum of Cu there is a clearly defined step at 7.8 eV and a peak at 11.6 eV. In the spectra of the alloys (all Pt concentrations and phases) a broad step/shoulder is seen to extend from about 8.0 eV to as much as 11.5 eV.

The EELS of the pure metals Cu and Pt agree very well with published measurements [3.8, 3.9]. Our spectra lack detail below about 3.0 eV; this region is dominated by the tail of the zero loss peak. The absence of the K-core losses of oxygen and carbon indicate that the surfaces were free of oxides and other contaminants.

We will first turn our attention to the two welldefined peaks at about 20 eV and 28 eV, in the spectra of the alloys. In the EELS of pure Cu these peaks are at 20.6 ev and 28.6 eV. The peak at 20.6 is stronger than the peak at 28.6 eV in pure Cu. The 20.6 eV peak has been

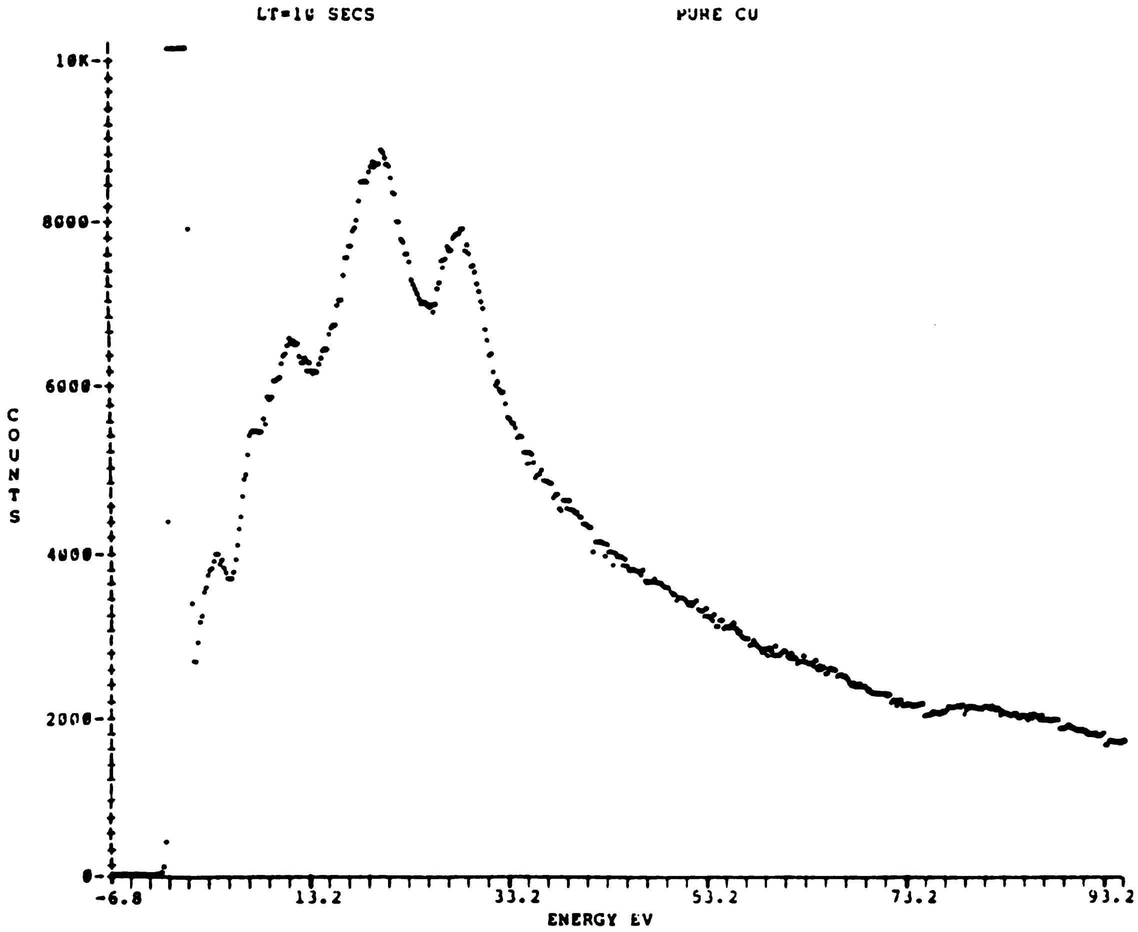

Figure 3.13

EELS of Cu

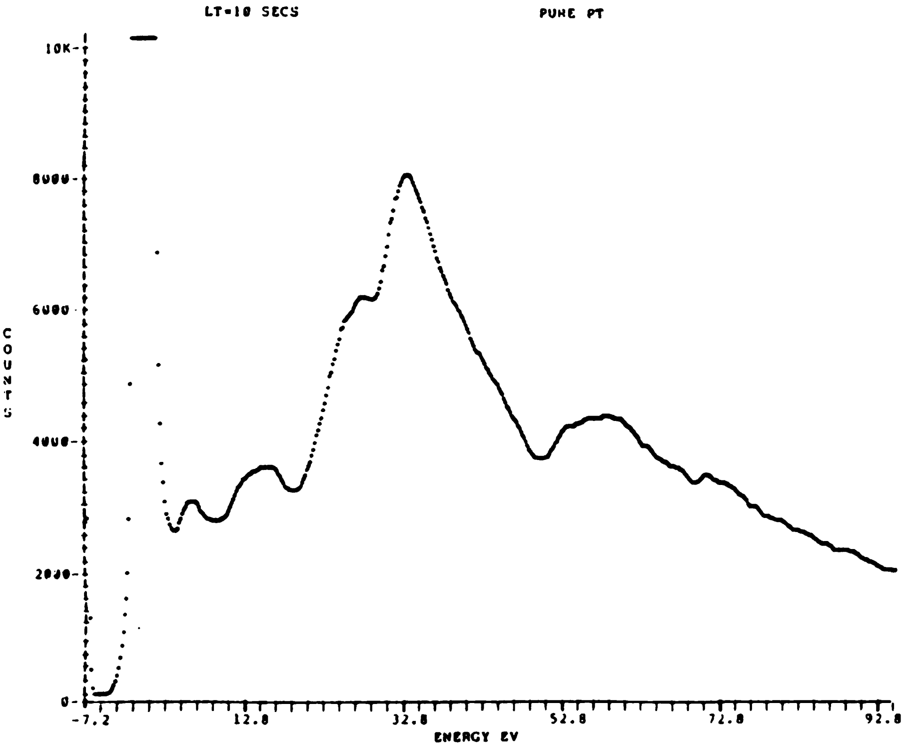

Figure 3.14

EELS of Pt

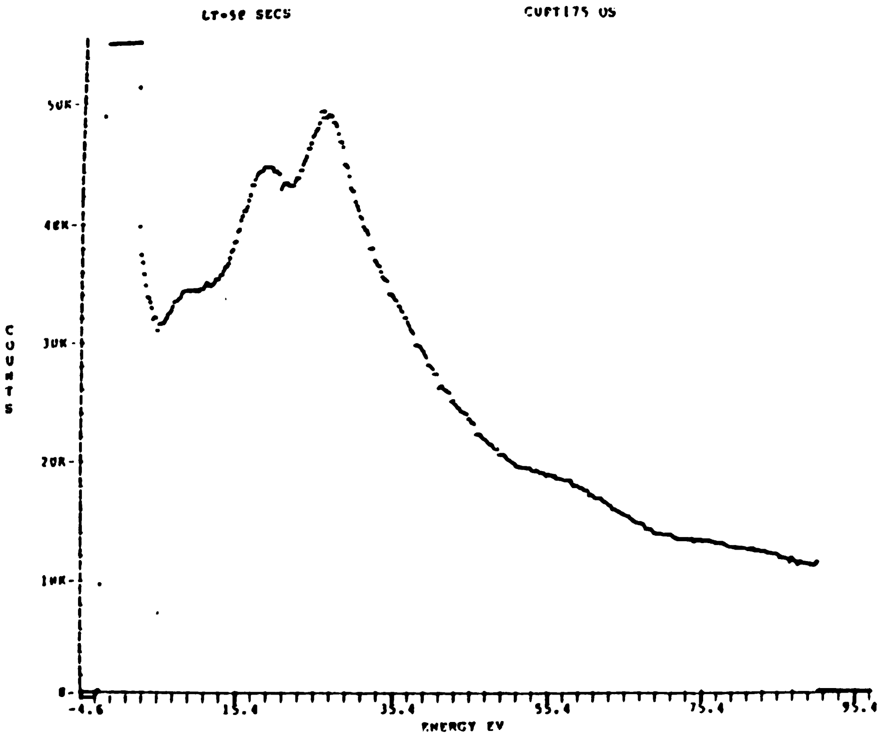

Figure 3.15
EELS of $Cu_{82.5}Pt_{17.5}$ Ordered

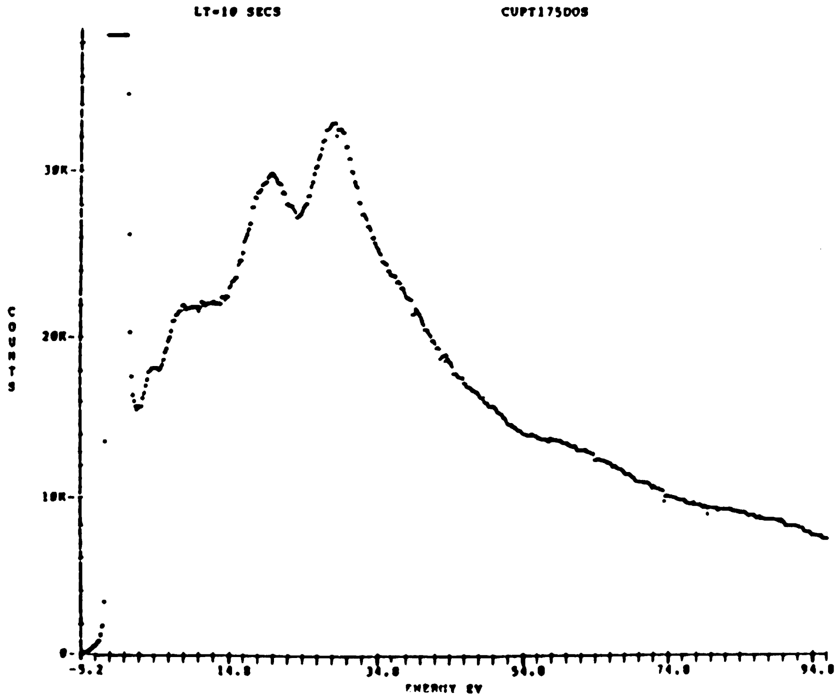

Figure 3.16
EELS of $Cu_{82.5}Pt_{17.5}$ Disordered

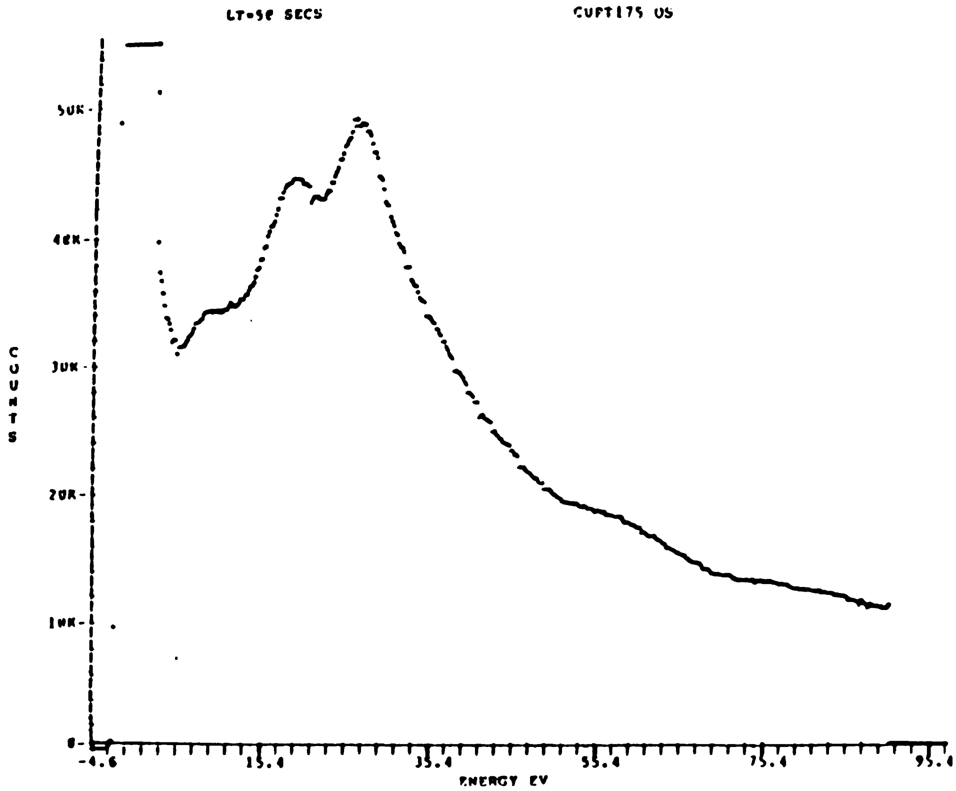

Figure 3.15
EELS of $Cu_{82.5}Pt_{17.5}$ Ordered

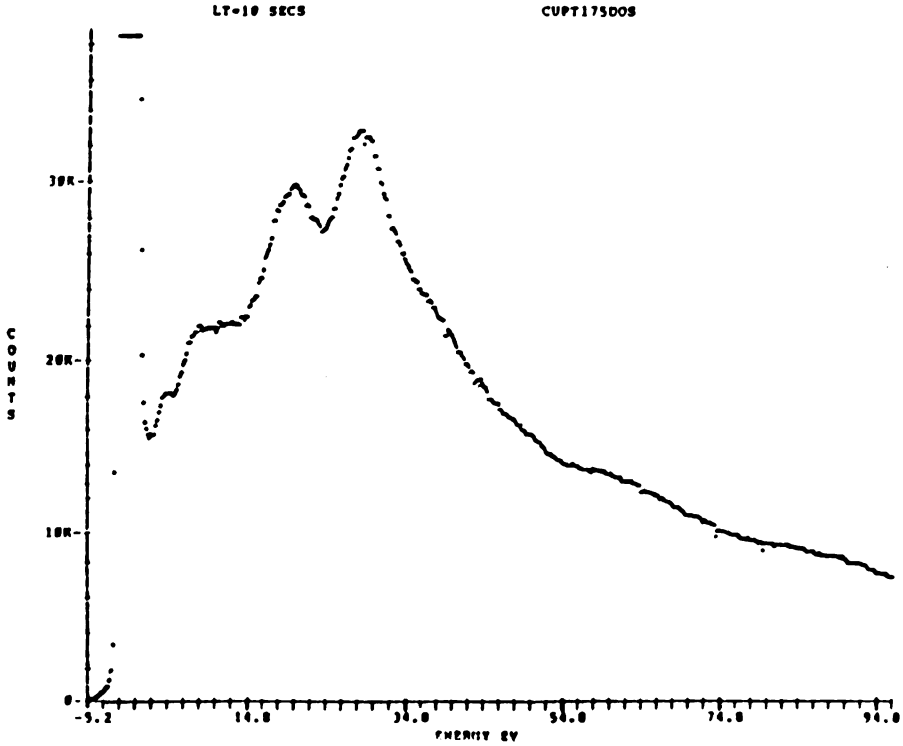

Figure 3.16
EELS of $Cu_{82.5}Pt_{17.5}$ Disordered

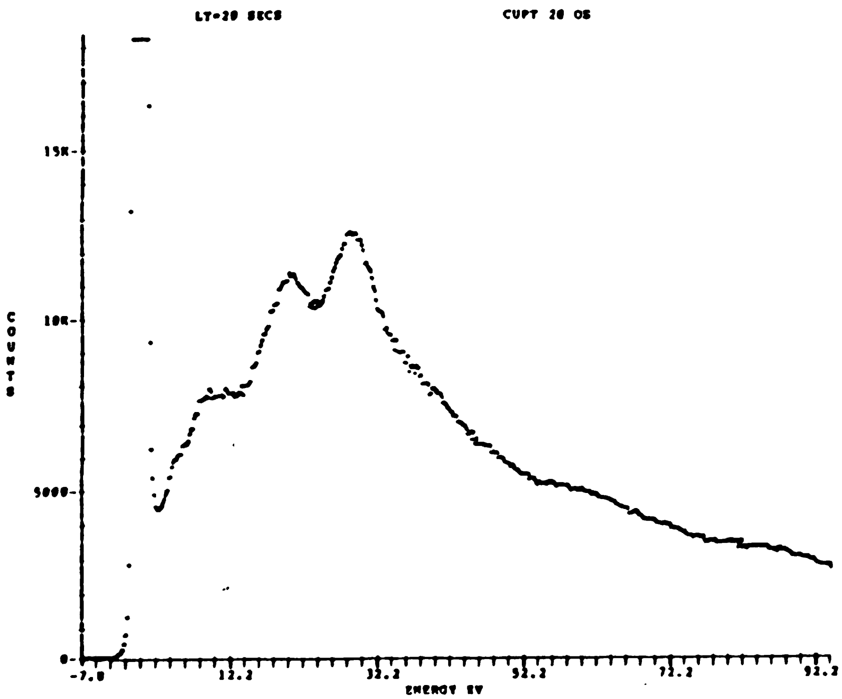

Figure 3.17
EELS of $Cu_{80}Pt_{20}$ Ordered

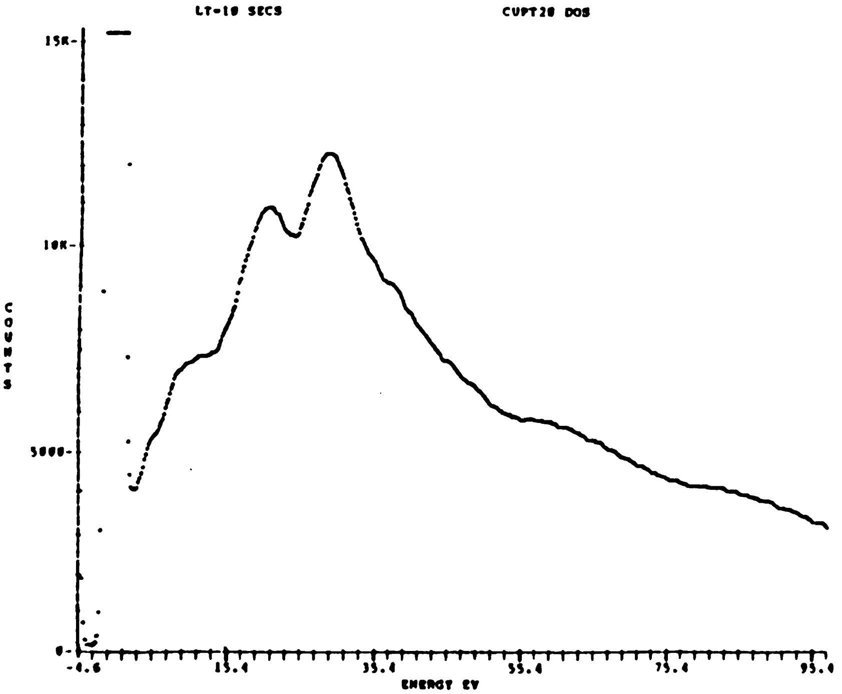

Figure 3.18
EELS of $Cu_{80}Pt_{20}$ Disordered

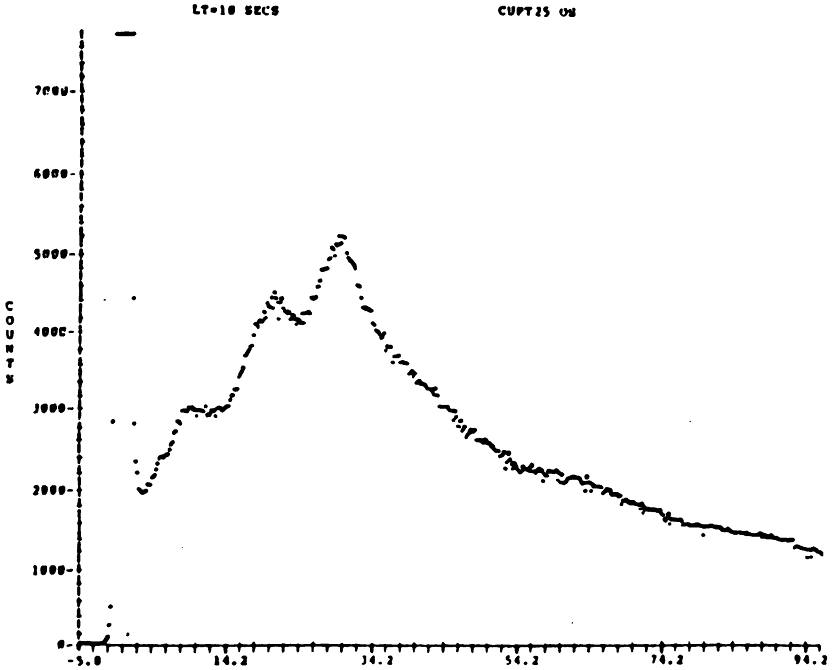

Figure 3.19
EELS of $Cu_{75}Pt_{25}$ Ordered

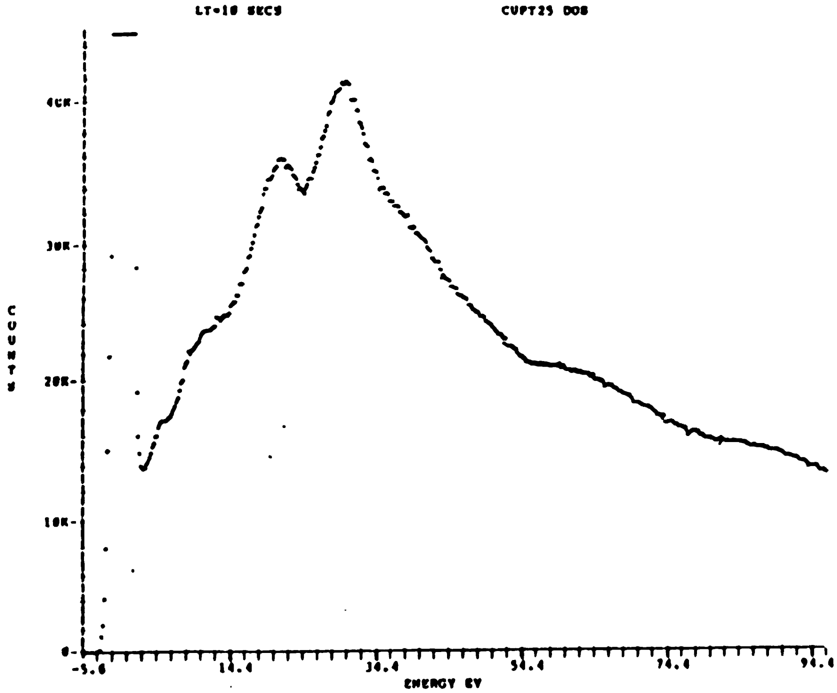

Figure 3.20
EELS of $Cu_{75}Pt_{25}$ Disordered

associated with a volume plasma oscillation, corresponding to an effective electron density of about 4 electrons/atom. There are a total of 11 electrons in the 3d(10) and 4s(1) bands of Cu. Assuming that all 11 electrons participate in the plasma oscillation, the energy of the plasmon is about 32 eV. The ineffectiveness of the free-electron model to describe accurately the transition/noble metals may be seen from this discrepancy in the measured and predicted plasmon energies.

In the EELS of the alloys, the two peaks (at 20 eV and 28 eV) have changed significantly in intensities, but there is no appreciable shift in the position of the 20 eV peak. The 28 eV peak appears to have shifted by less than 2 eV in Cu_3Pt alloy. The 28 eV peak is more intense than the 20 eV peak in the alloys; in pure Cu the 20 eV peak is stronger than the 28 eV peak.

Ya Ksendzov [3.10] has done a review of the electron energy loss spectra of the 3-d transition metals and has attributed the 20 eV excitation to a collective oscillation of the 3-d electrons of a particular spin orientation. In pure Cu there are 5 electrons with spin up (or down). If the 20 eV peak in the EELS of pure Cu was assumed to be due to a free electron like plasma oscillation we arrive at an electron density of about 4.2 electrons/atom. This agreement between Ya Ksendzov's prediction and experimental observation must not be taken too seriously. This model is

just a phenomenological model that appears to explain the occurrence of various features in the EELS of the 3-d transition metals without giving a fundamental reason for the splitting of the electrons into two groups of opposite spins.

The description given by Ya Ksendzov would appear to suggest a shift of the 20 eV peak to lower energies in the alloys. No such shifts in the position of these peaks are observed. This model also attributes the 28 eV excitation in pure Cu to a collective oscillation of all the 11 outer electrons. When Pt atoms are added to Cu to form the alloys the effective number of electrons per atom would decrease; hence the 28 eV peak should shift to lower energies. On the contrary these peaks have a small but systematic shift to higher energies as the Pt concentration is increased. This behavior defies simple explanations. These features also appear to be insensitive to the crystalline phase of the alloys. Extensive band structure calculations for the Cu-Pt alloys are needed before an attempt is made to explain these anamolies.

Many of the sharp features seen at low energies in the EELS of Cu are missing from the EELS of the alloys. Notable among these changes are the presence of a broad step/shoulder between 8 eV and 11.5 eV in the EELS of the alloys. To study the changes in the valence band structure of Cu brought about by alloying, we computed the dielectric function $\varepsilon(\omega)$ of the alloys by a Kramers-Kronig inversion of the energy loss spectra. The structures in $\varepsilon_2(\omega)$ correspond to critical points in the band transitions.

The computed optical functions $\varepsilon_2(\omega)$ for the alloys $Cu_{1-x}Pt_x$ are shown in Figures 3.21 - 3.27. Also shown is the computed optical function $\varepsilon_2(\omega)$ of pure Cu. Unlike the energy loss spectra, $\varepsilon_2(\omega)$ spectra of the alloys are very much like that of pure Cu (in the energy range 5 eV to 30 eV). The $\varepsilon_2(\omega)$ of the disordered phases (all Pt concentrations) show a clear structure at about 6 eV ± 1 eV. This feature is not very pronounced in $\varepsilon_2(\omega)$ of the ordered phase. The $\varepsilon_2(\omega)$ spectrum of pure Cu has a similar peak at about 6 eV. The crystal structure of pure Cu and the disordered $Cu_{1-x}Pt_x$ alloys is the FCC lattice. Thus this feature may well be an order-disorder effect.

On comparing the magnitude of $\varepsilon_2(\omega)$ at about 6.0 eV in the different disordered alloys and pure Cu, we see a trend. It must be stressed that this comparison of the magnitude of ε_2 is proper because the data presented here were all measured under similar conditions and the analysis techniques are identical.

The magnitude of $\varepsilon_2(\omega)$ at 6.0 eV is about 2.0 for pure Cu and increases monotonically to about 3.2 for the disordered $CuPt_{0.25}$, alloy. The $\varepsilon_2(\omega)$ of the ordered phase, on the other hand, is about 2.6 ± 0.1 for all Pt concentrations. Interband transitions set in at

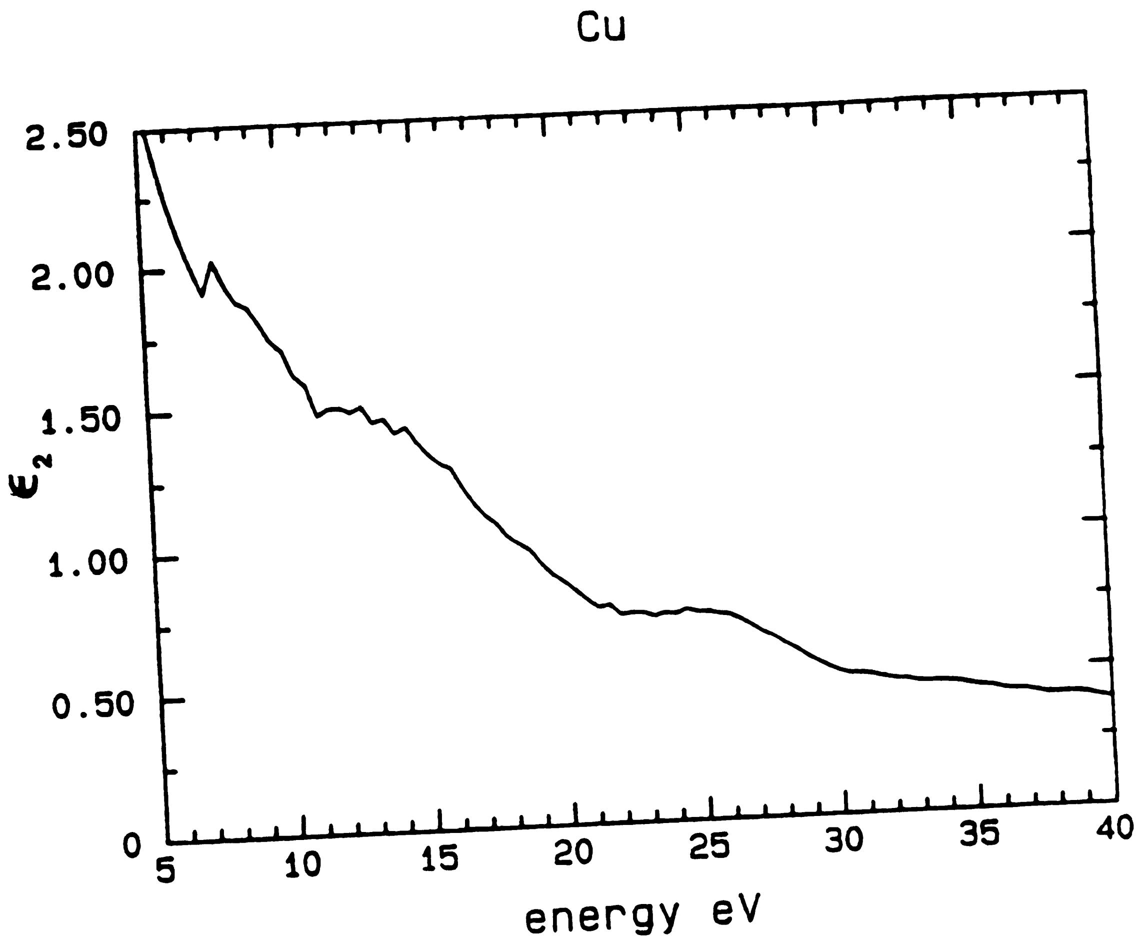

Figure 3.21

$\varepsilon_2(\omega)$ of Cu

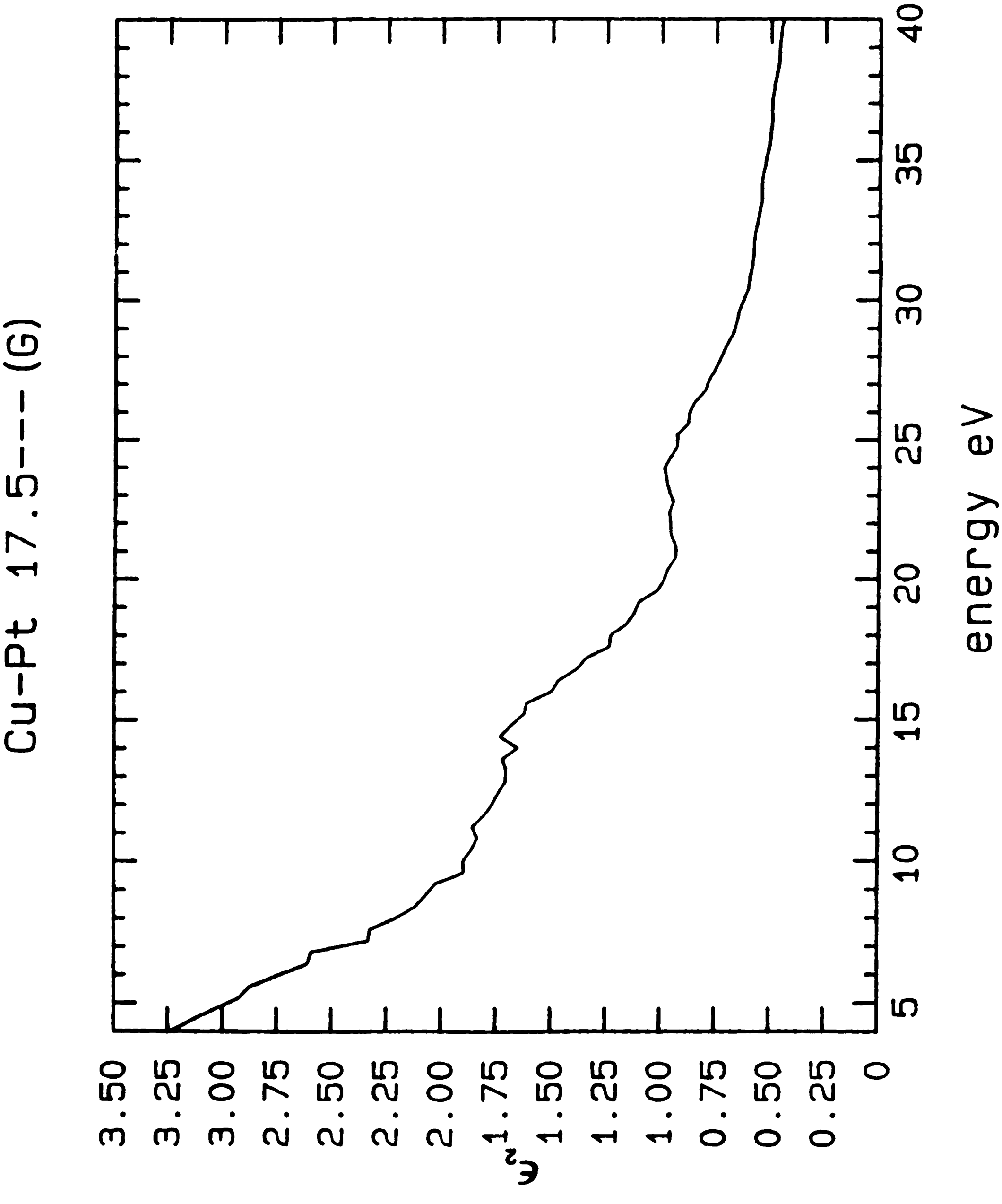

Figure 3.22

$\epsilon_2(\omega)$ of $Cu_{82.5}Pt_{17.5}$ Ordered

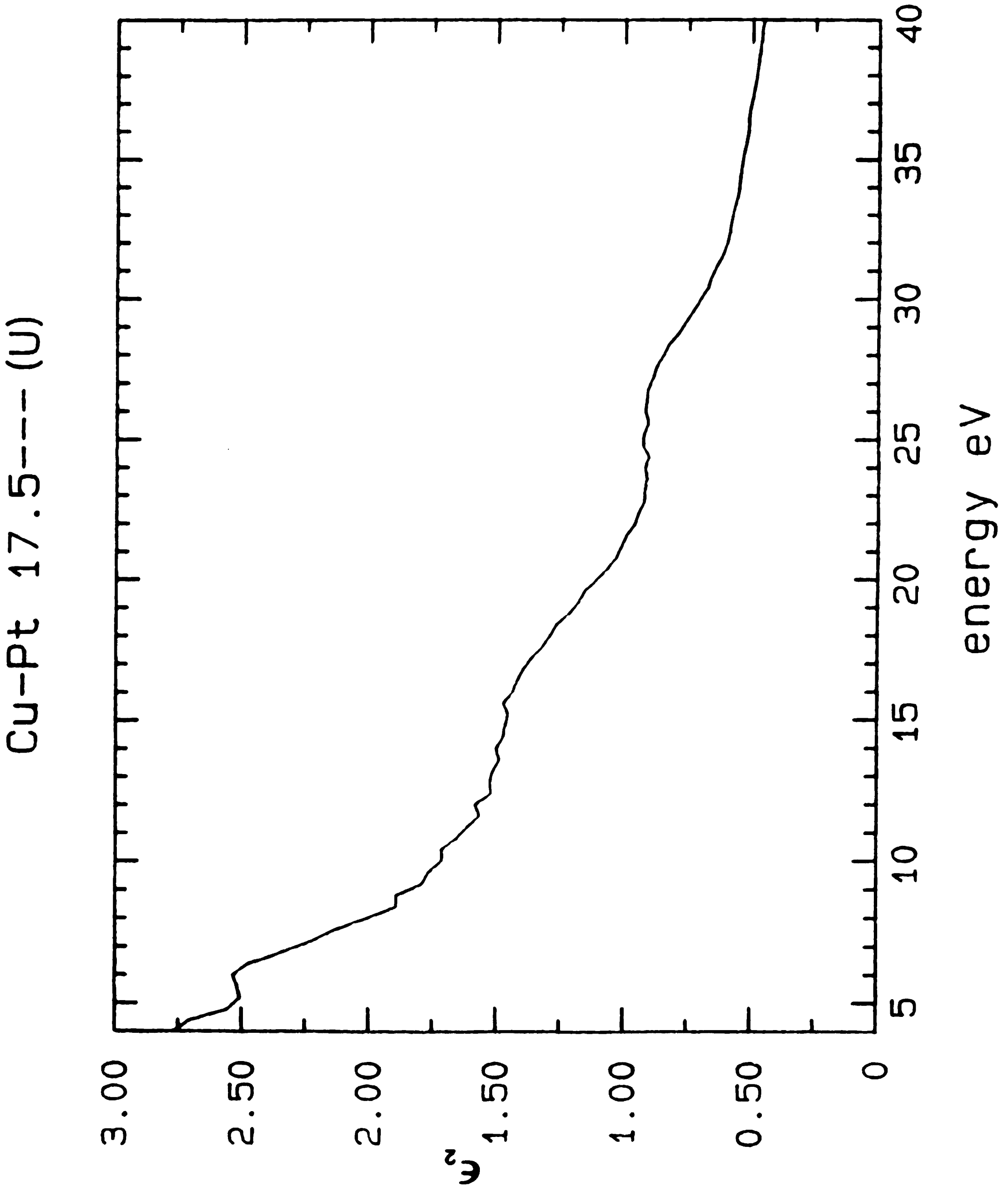

Figure 3.23

$\varepsilon_2(\omega)$ of $Cu_{82.5}Pt_{17.5}$ Disordered

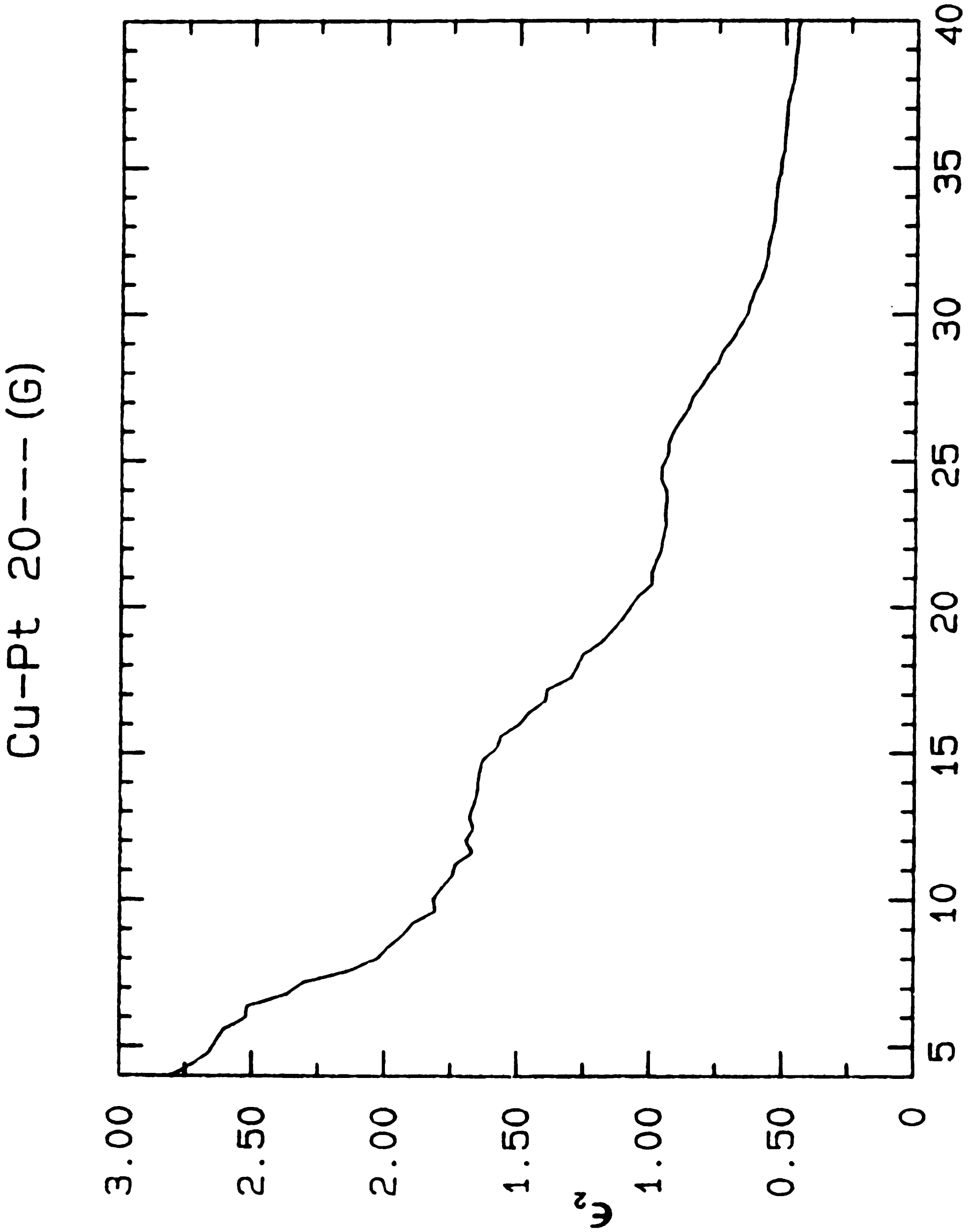

Figure 3.24

$\varepsilon_2(\omega)$ of $Cu_{80}Pt_{20}$ Ordered

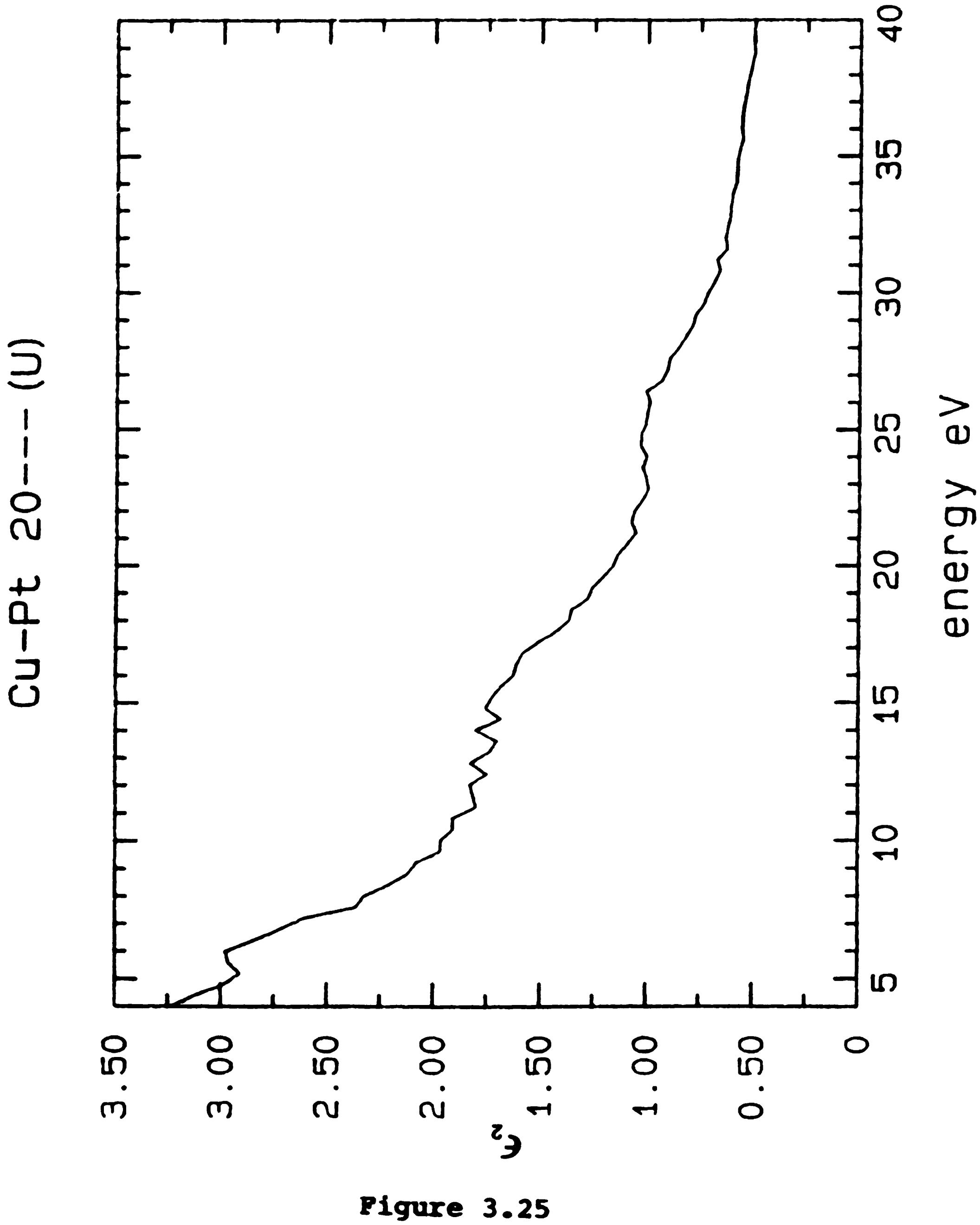

Figure 3.25

$\varepsilon_2(\omega)$ of $Cu_{80}Pt_{20}$ Disordered

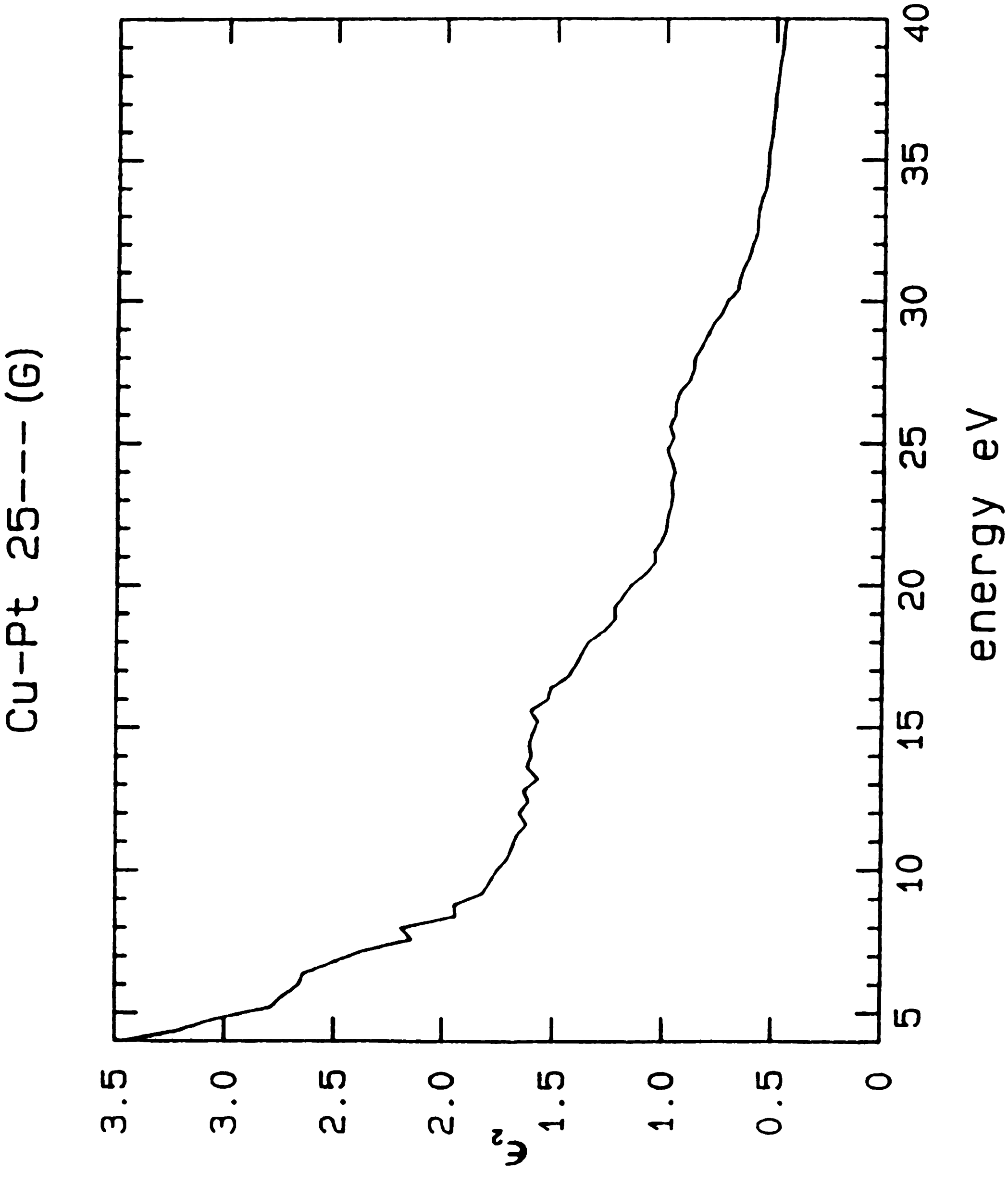

Figure 3.26

$\varepsilon_2(\omega)$ of $Cu_{75}Pt_{25}$ Ordered

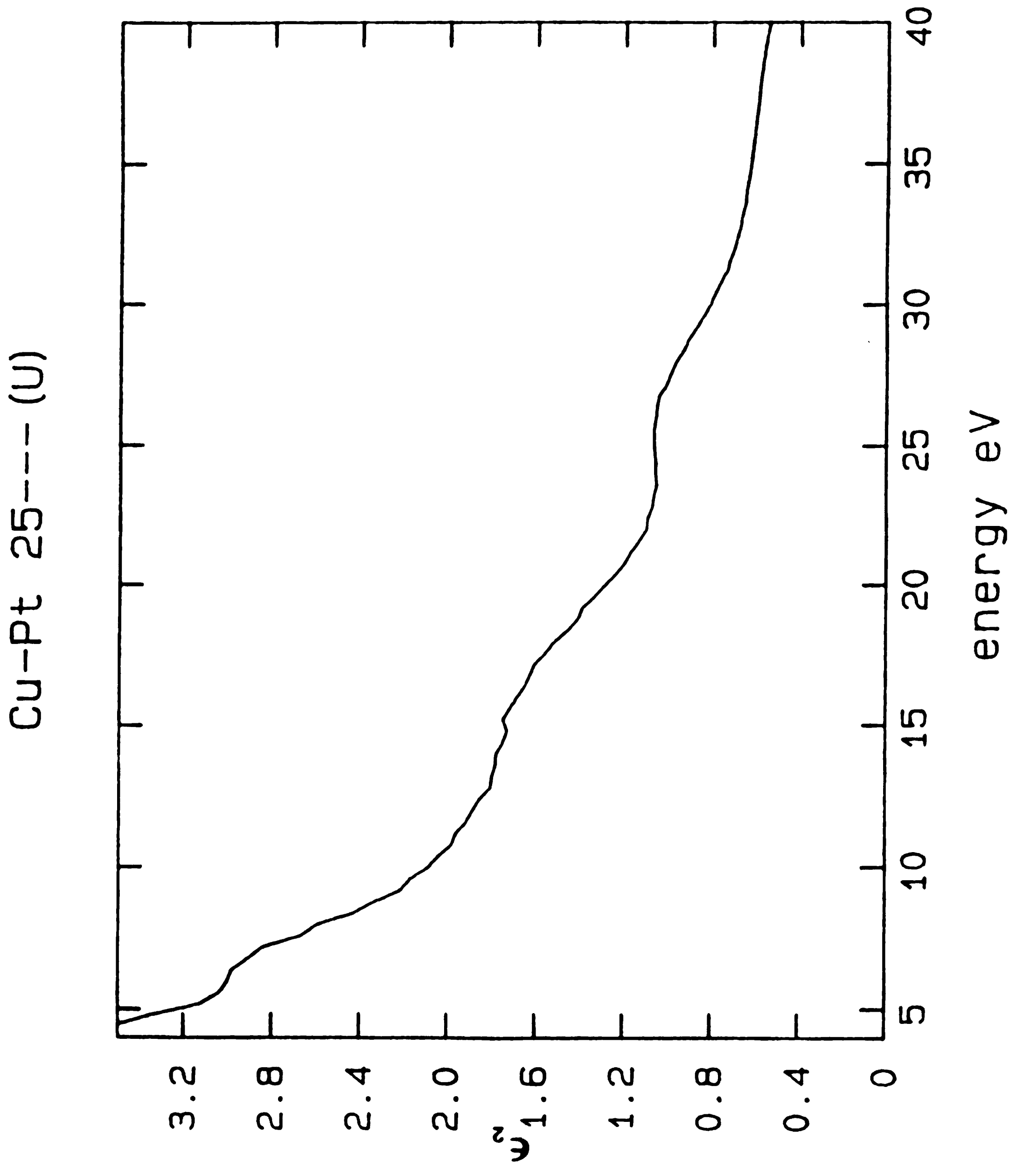

Figure 3.27

$\varepsilon_2(\omega)$ of $Cu_{75}Pt_{25}$ Disordered

about 2 eV in pure Cu and persist up to about 8 eV before falling off in strength. In pure Pt the onset of interband transitions is below 1 eV. Transitions are possible up to 10 eV. The systematic increase in $\epsilon_2(\omega)$ at 6.0 eV as a function of the Pt concentration may be due to an increase in the DOS at about 6.0 eV below the Fermi level.

The $\epsilon_2(\omega)$ spectra of pure Cu and the alloys are very similar at higher (7 eV and above). The loss of sharp features in Cu and the occurrence of a step at about 8 eV in the EELS of the alloys are not reflected in $\epsilon_2(\omega)$. Hence, these changes defy a simple explanation. The feature in $\epsilon_2(\omega)$ at about 26 eV appears to be sensitive to the structural phase of the alloys. The magnitude of $\epsilon_2(\omega)$ at this energy increases from 0.90 for $CuPt_{0.175}$ alloy to 1.1 for the $CuPt_{0.25}$. This is seen only in the disordered phases. The $\epsilon_2(\omega)$ of pure Cu at 26 eV is 0.75. This difference in $\epsilon_2(\omega)$ of the two phases could be an order-disorder effect.

CONCLUSION:

Optical reflectivity $R(\omega)$ and transmission EELS of Pt, Cu, and atomically ordered and disordered $Cu_{1-x}Pt_x$ alloys $(0.175 \leq x\ 0.25)$ were measured. The reflectivity measurements were in the range 1.0 eV to 5.0 eV and the EELS measurements were in the range 3 eV to 90 eV. A few indications of order-disorder effects on the reflectivity and the EELS were identified, though further studies using

highly ordered (LRO > 0.95) samples are needed before arriving at an accurate description of the processes involved. In the reflection spectra, the absorption edge of Cu at 2.0 eV was seen to disappear for Pt concentrations above 10%. The overall reflectivities of the disordered phases was higher than that of the ordered phase--an order-disorder effect. The optical functions were computed from the EELS by kk inversion. The imaginary part $\varepsilon_2(\omega)$, of the dielectric function of the alloys showed a feature at 6.0 eV, that was sensitive to the structural phase of the alloy.

Chapter 4

Order-Disorder Effects in the $Fe_{0.8}B_{0.2}$ System

Topological disorders have a large influence on the electronic and other physical properties of solids. A class of topologically disordered systems called metallic glasses exhibit new and very interesting magnetic and electronic properties that are of great technological importance. A desire to understand and exploit the properties of metallic glasses partly explains the intense research activity this field has seen in recent years.

Amorphous $Fe_{1-x}B_x$ has long been a model for the study of magnetic and structural properties of metallic glasses [4.1]. Extensive investigations of the electronic structure have also been carried out [4.2, 4.3, 4.4]. In spite of the existence of a large body of information on the $Fe_{1-x}B_x$ system, some controversial questions remain unanswered. For example, the work of Abd-Elmeguid et.al. [4.5] suggest that the short range order in crystalline $Fe_{0.8}B_{0.2}$ (c - $Fe_{0.8}B_{0.2}$)and amorphous $Fe_{0.8}B_{0.2}$ (a-$Fe_{0.8}B_{0.2}$) are not very different. But the Mossbauer studies on a-$Fe_{0.8}B_{0.2}$ done by Eibschutz et al [4.6] and Chien and Unruh [4.7] indicate that the short range order and atomic coordination in c-$Fe_{0.8}B_{0.2}$ are different from

those of a-$Fe_{0.8}B_{0.2}$. De Crescenzi et al [4.8] have conducted Auger and EELS studies on the crystalline and amorphous phases of this alloy and found a similarity between c-Fe and c-$Fe_{0.8}B_{0.2}$ and a similarity between c-Ni and the the metallic glass.

There exists a fair amount of data on the electronic properties of crystalline and amorphous $Fe_{1-x}B_x$ for x near 0.2 [4.4, 4.8, 4.9]. But a quick review of the available data on the electronic structure does not yield a clear picture of the electronic excitations in bulk $Fe_{1-x}B_x$. The difficulty is partly due to the fact that some of the experimental information come from experiments that are sensitive to the condition of the surface of the sample. Thus, some of the excitations reported by various investigators may simply be surface excitations or due to the impurities on the surface.

De Crescenzi et al [4.8] have carried out electron energy loss studies on the $Fe_{0.8}B_{0.2}$ system. They used low energy (120 eV) electrons for an EELS study in the reflection geometry. The mean free path of these electrons is about 10 A [4.10]. These electrons thus probe the surface and the top 20-25 A of the sample: Consequently the reflection EELS contains a significant contribution from the surface excitations. Moreover, it is not clear if the spectra were corrected for multiple scatterings. The effect of multiple scatterings are 'amplified' in the

derivative detection technique employed by De Crescenzi et al.

In this investigation we have measured the transmission EELS of a-$Fe_{0.8}B_{0.2}$ using electrons of energy 100 keV. We believe the results reported here reflect the electronic properties of bulk a-$Fe_{0.8}B_{0.2}$.

SAMPLE PREPARATION:

The amorphus $Fe_{0.8}B_{0.2}$ samples used in this study were provided by Denis Greig and were prepared by melt-spinning at the University of Leeds. This technique produced a thin long ribbon about 3 mm wide and 45 μm thick. Samples for the electron microscope were prepared from this ribbon by punching out 3 mm discs and jet-etching these discs in a jet-etching unit. No attempt was made to measure the micro-composition of the specimen in the AEM because the characteristic X-rays of Boron are not detectable using the energy dispersive X-ray detector. X-ray diffraction pattern of these ribbons showed no Bragg lines.

RESULTS AND DISCUSSION:

Ray and Tauc [4.1] measured the optical reflectivity of a-$Fe_{0.8}B_{0.2}$ in the photon energy range 0.05 eV to 6.0 eV (Figure 4.1). The reflectivity monotonically decreases from almost 1.0 at 0.05 eV to about 0.35 at 6.0 eV. The reflectivity spectrum is essentially featureless. Our reflectivity measurements (Figure 4.2) in the energy range

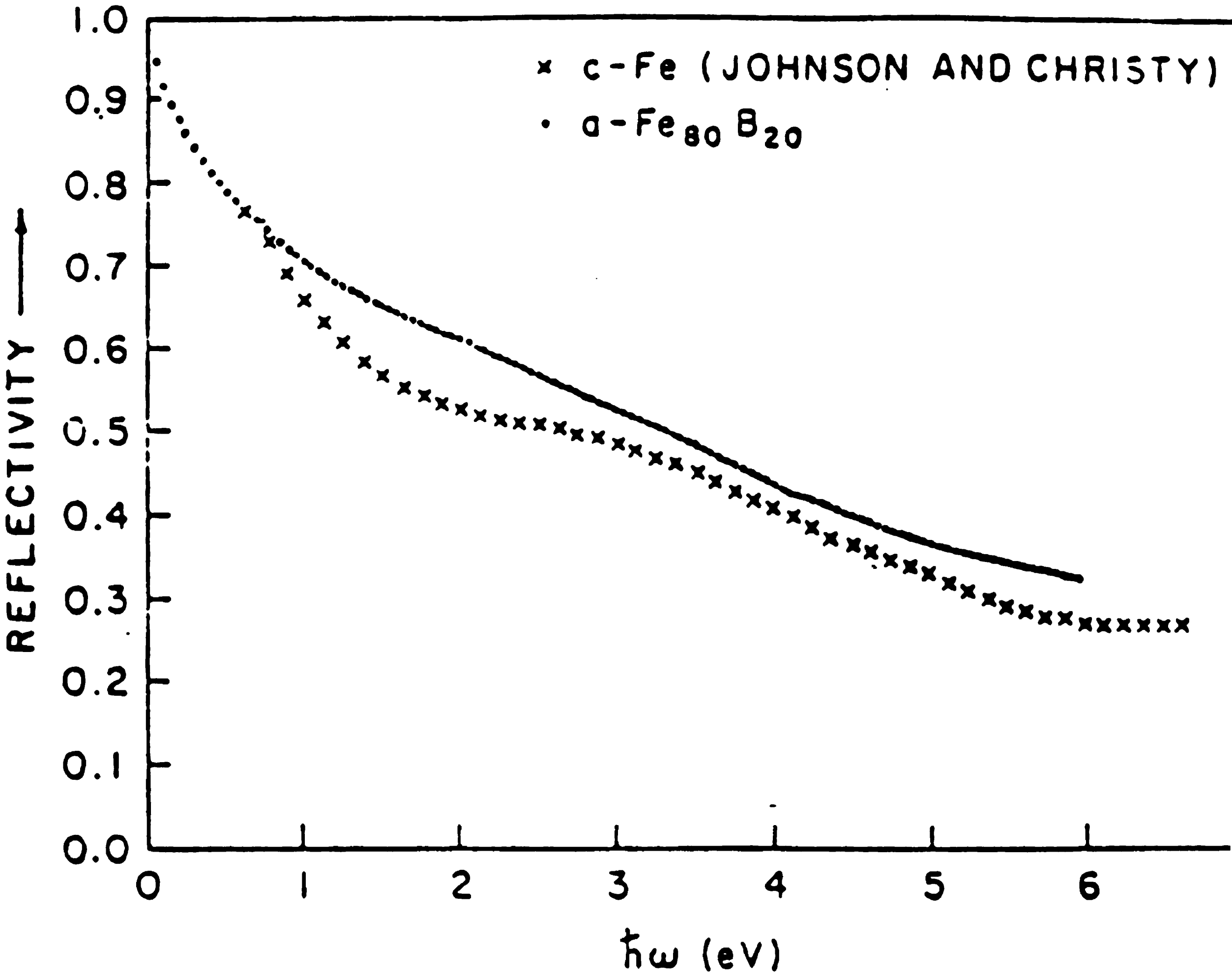

Figure 4.1

$R(\omega)$ of a-$Fe_{0.8}B_{0.2}$, Reference [4.1]

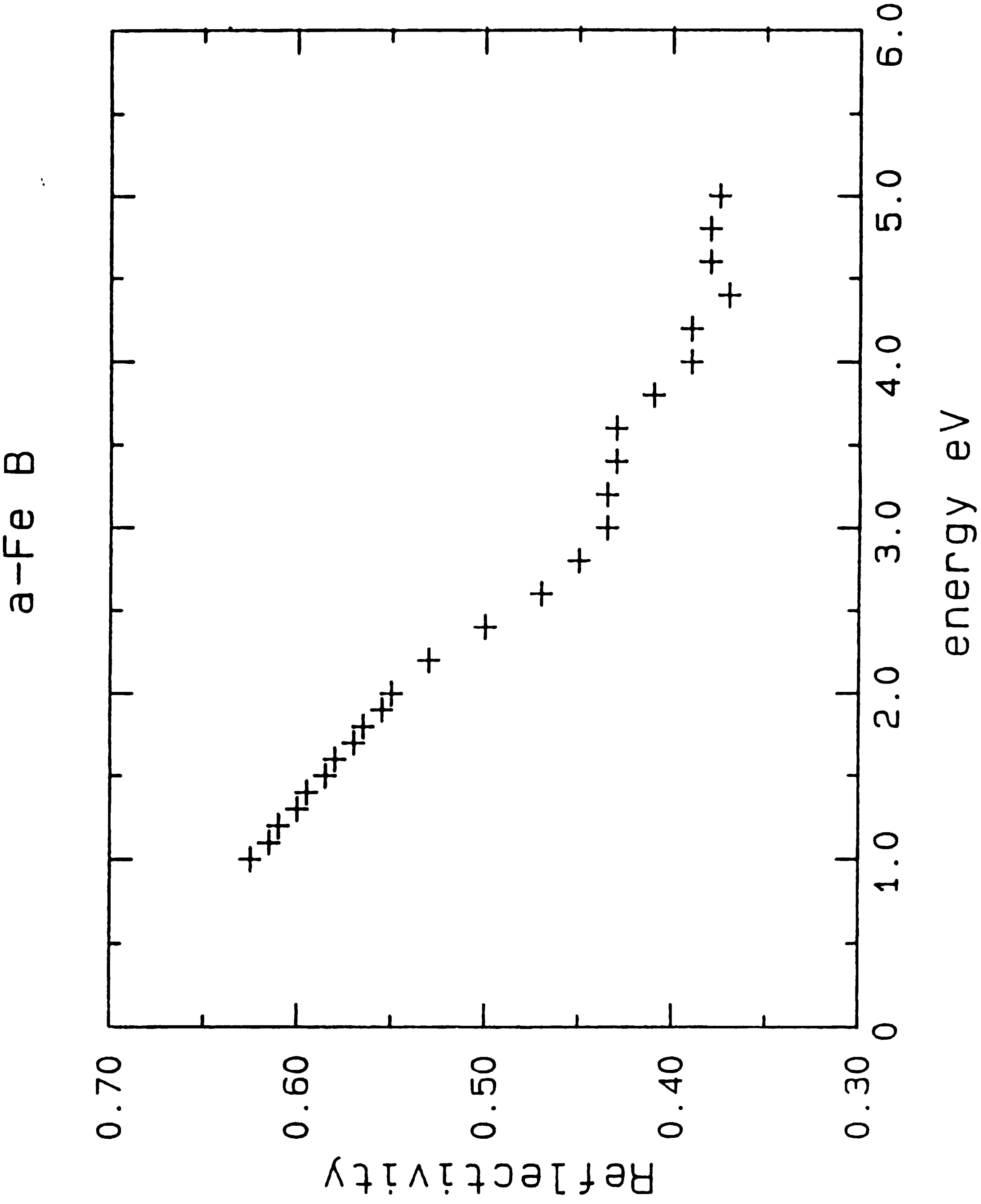

Figure 4.2

R(ω) of a-$Fe_{0.8}B_{0.2}$, This Investigation

0.6 eV to 5.0 eV agree with the results reported by Ray and Tauc. In contrast, the reflectivity spectrum of crystalline Fe has a small broad increase in reflectivity (drop in absorption) at about 3.5 eV.

Our measurements of the electron energy loss spectra of a-$Fe_{0.8}B_{0.2}$ are presented in Figures 4.3, 4.4 and 4.5. Spectra from sample regions of different thicknesses are also presented. As a measure of the thickness of the sample, the ratio t of the integrated loss spectrum (3 eV to 90 eV and the integrated zero loss peak was used. In the spectra from thin regions (t = 0.1 and 0.32) there appears a bump at about 4.0 eV (Figure 4.4). For larger sample thickness (t = 0.66 and 1.0) this feature disappears (Figure 4.5). In addition the 'tail' of the zero loss peak decreases for larger thicknesses.

Loss features due to volume excitations increase in intensity as the sample thickness increases. Loss features due to surface excitations, on the other hand, stay the same in intensity; indeed, relative to the rest of the spectrum they seem to decrease in intensity. Using this guideline, we attribute the feature seen at about 4.0 eV to a surface excitation.

In the energy loss spectra for all thicknesses, there is a broad loss feature at about 23 eV. One probable explanation for this feature is a collective excitation similar to the plasma oscillations of a free-electron

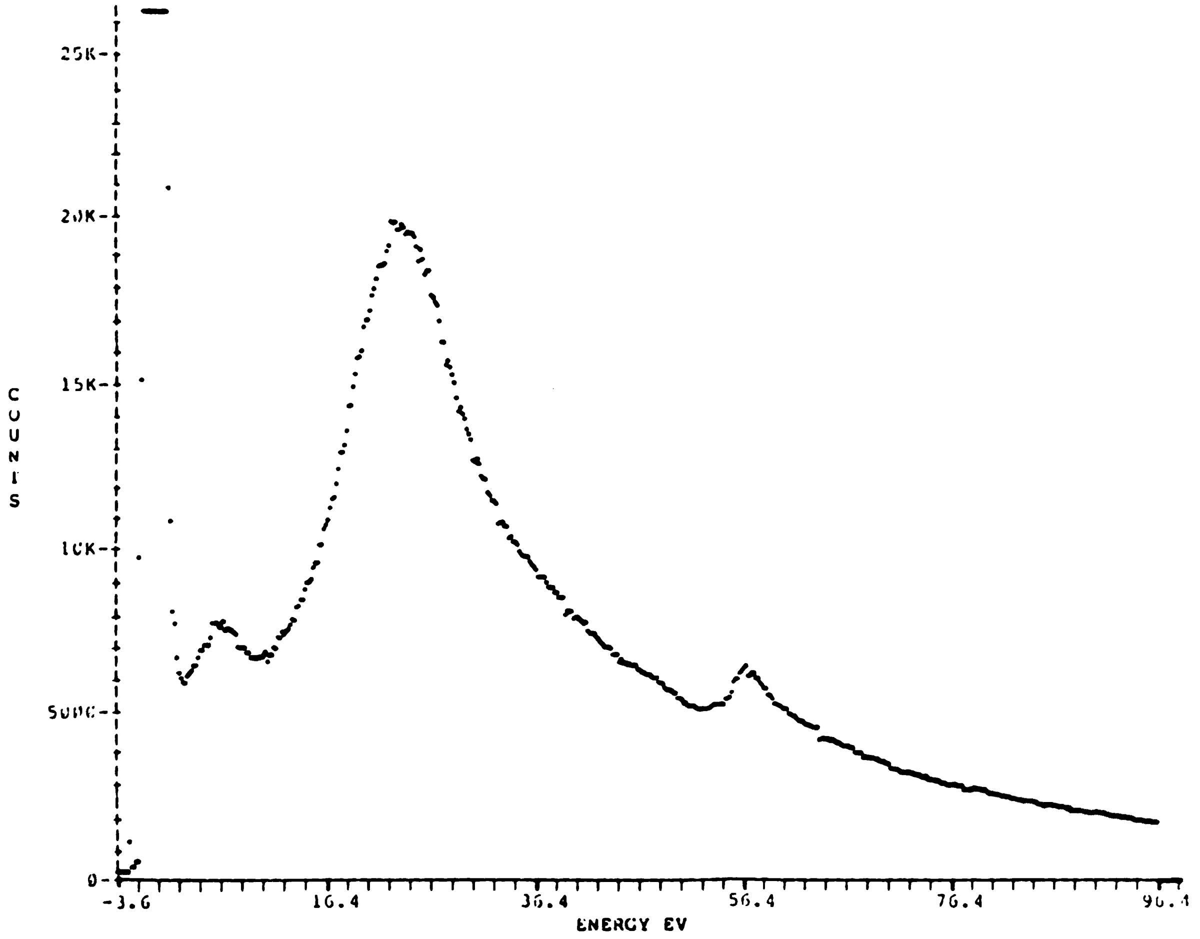

Figure 4.3

EELS of a-$Fe_{0.8}B_{0.2}$

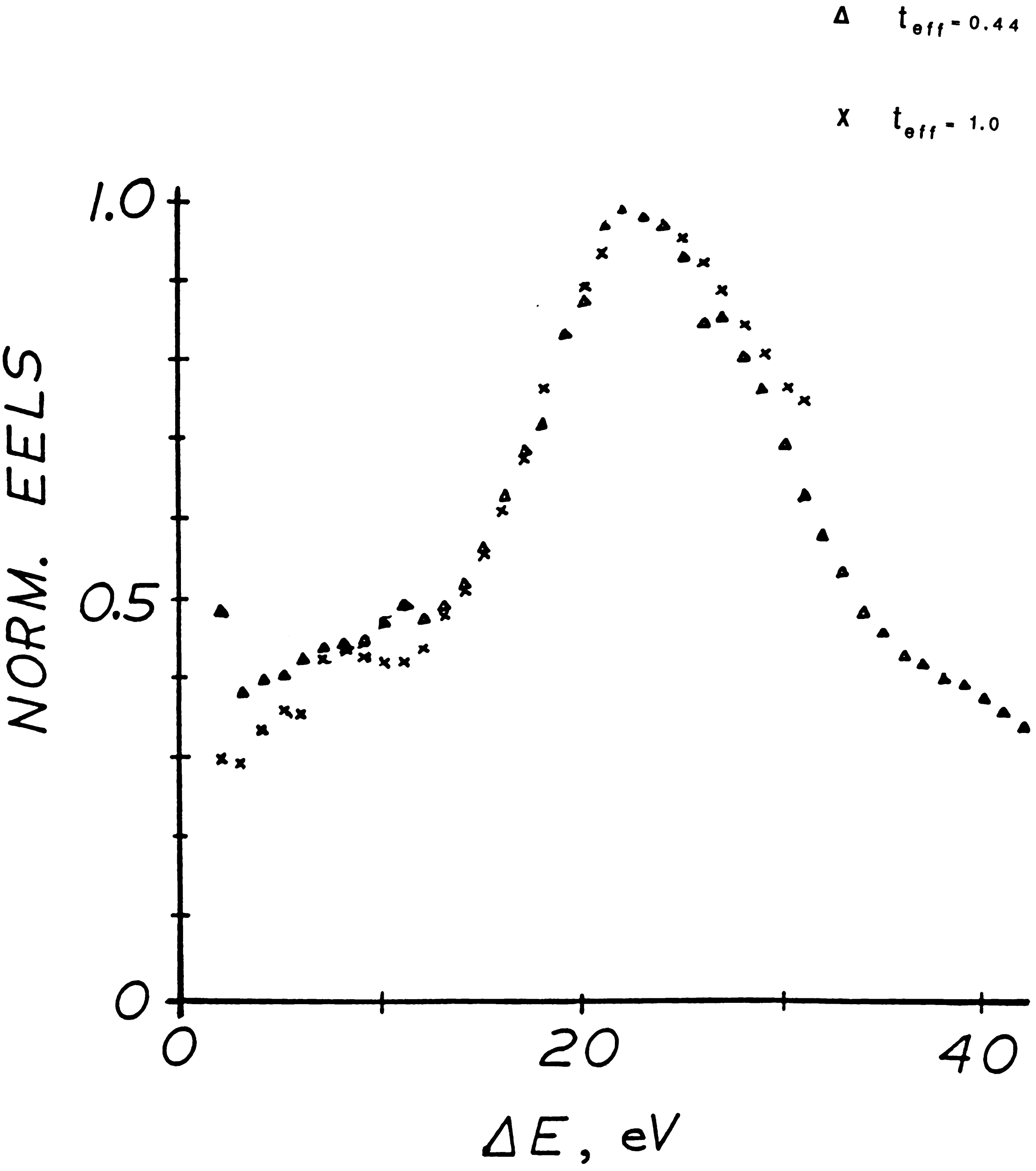

Figure 4.4

Normalized EELS of a-$Fe_{0.8}B_{0.2}$

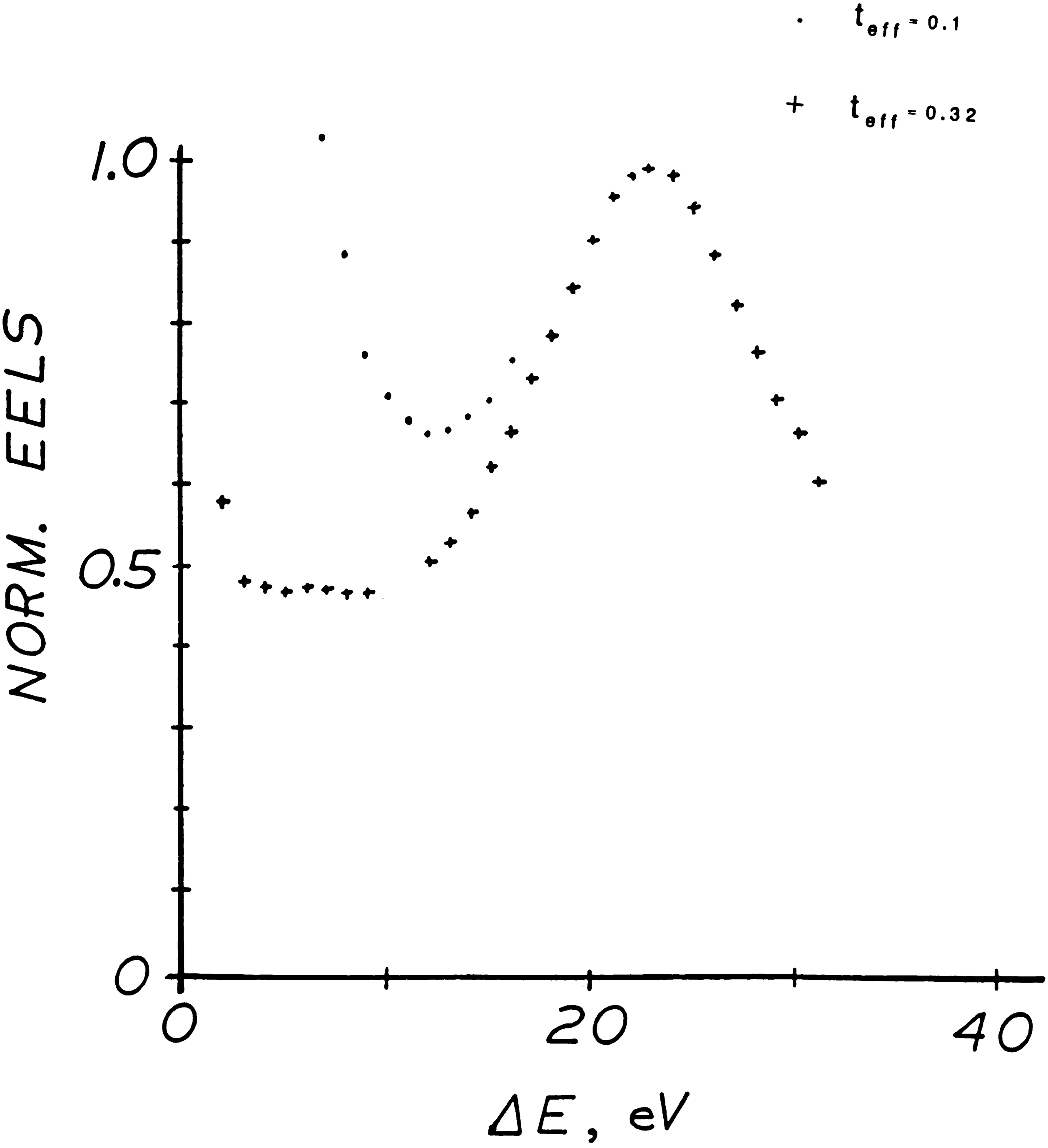

Figure 4.5

Normalized EELS of a-$Fe_{0.8}B_{0.2}$

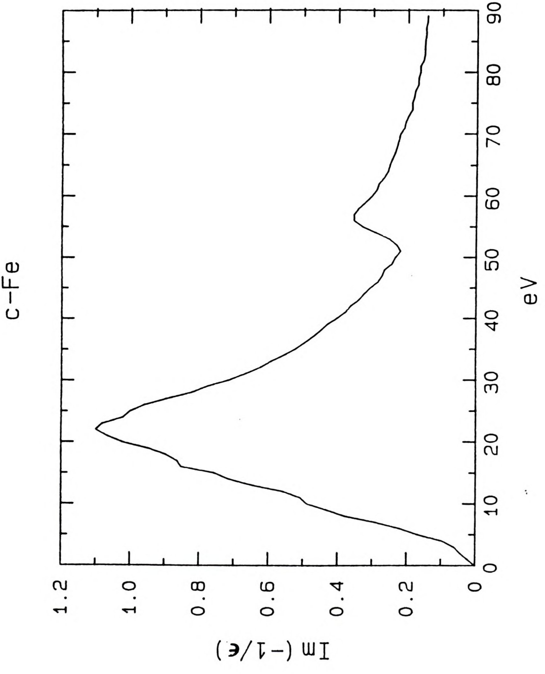

Figure 4.6

EELS of c-Fe

metal, but any attempt to further compare this peak to the free-electron plasma must be resisted. Plasma oscillationsare not well-defined in a system such as this transition metal-metalloid amorphus alloy. Depending on the procedure used to locate its position (centroid or peak), this feature has shifted by about 1 eV to 3.5 eV relative to pure crystalline Fe.

More significant is the absence of any sharp features in the spectrum of a-$Fe_{0.8}B_{0.2}$, that are normally found in the spectra of c-Fe. Many of these features are associated with interband transitions. Colavita et al [4.11] have done a comprehensive study of the excitations in ferromagnetic Fe and have identified many of the interband transitions in the energy loss spectra. The absence of these sharp features in the energy loss spectra of a-$Fe_{0.8}B_{0.2}$ may be explained by the lack of long range order in the amorphous phase. The loss of long range order also leads to the breakdown of the momentum conservation requirements for transitions between energy levels. Thus, one may conclude that in the amorphous $Fe_{0.8}B_{0.2}$ energy absorption is possible at energies forbidden in the c-$Fe_{0.8}B_{0.2}$ by the K-conservation requirement and would show up as a broad dominant loss. In our EELS measurements of pure Fe and the metallic glass the dominant losses are about 20 eV wide (FWHM) indicating that the loss of long

range order has no appreciable influence on the dominant loss.

At higher energies we see energy losses due to transitions from the inner shells. The feature at about 54 eV is the Fe $M_{2,3}$ core loss ($3P_{1/2,3/2} \rightarrow$ allowed states above Fermi level) and the features near 708 eV and 721eV are the Fe $L_{2,3}$ core losses ($2P_{1/2,3/2} \rightarrow$ allowed states above Fermi level). The shape and location of these loss features convey a great deal of information about the local chemical ordering (or the lack thereof) of the solid. In the spectra of a-$Fe_{0.8}B_{0.2}$, we find no shifts in the positions or changes in the shapes of these core losses. They resemble those in the spectra pure crystalline Fe.

We did not measure the EELS of c-$Fe_{0.8}B_{0.2}$. Hence, we report here measurements of other investigators for the sake of completeness and for comparison with our measurements. The studies of De Crescenzi et al [4.8] and Th Paul and Neddermeyer [4.4] need special mention. These two groups have done photoemission (XPS, UPS) reflection EELS (using second derivative detection technique) and Auger spectroscopy.

Several features at 2.5 eV, 5.9 eV, 9.1 eV, 12.0 eV and 16.6 eV are reported by De Crescenzi et al [4.8], though some of these may be due to the surface and adsorbed atoms on the surface. These results should be compared with the features at 4.5 eV, 8.5 eV, 11.5 eV and 23.0 eV as

determined in this investigation. De Crescenzi et al [4.8] also found a similarity between the energy loss spectra of pure crystalline Fe and c-$Fe_{0.8}B_{0.2}$ and a similarity between the spectra of pure crystalline Ni and a-$Fe_{0.8}B_{0.2}$.

De Crescenzi et al [4.8] explained the above mentioned similarities in the energy loss spectra in terms of the changes in local chemical short-range ordering and the changes in atoms coordinations when a-$Fe_{0.8}B_{0.2}$ crystallizes to form c-$Fe_{0.8}B_{0.2}$. Hricovini and Krempasy [4.3] have done XPS and UPS studies on $Fe_{0.8}B_{0.2}$ and conclude that the electronic structure of a-$Fe_{0.8}B_{0.2}$ is similar to the electronic structure of crystalline Fe_3B. The 3d electrons of Fe are basically undisturbed by the addition of boron. They rule out transfer of charge from B to Fe to explain this similarity in the electronic structure of a-$Fe_{0.8}B_{0.2}$ and Fe. Instead, hybridization of the s-p orbitals of Boron and the d-orbitals of iron is cited as a possible explanation.

Hybridization of the s-p orbitals and the d orbitals do result in the transfer of a small amount of charge between the two elements. The core-losses in EELS are sensitive to small charge transfers. In our EELS studies of a-$Fe_{0.8}B_{0.2}$, the $M_{2,3}$ core-losses of Fe at about 54 eV resembles the core-losses found in pure Fe in terms of shape and position. Thus the absence of a change in core-losses in a-$Fe_{0.8}B_{0.2}$ may be taken as an evidence ruling

out even small amounts of charge transfer. Examination of the Fe $L_{2,3}$ core losses (measurements not shown) also leads one to a similar conclusion.

Optical functions such as $\varepsilon_2(\omega)$ and $R(\omega)$ were computed from the energy loss data. These results are presented in Figures 4.7 and 4.8. $\varepsilon_2(\omega)$ and $R(\omega)$ share some common features--the plateau at about 10 eV and the structure at about 54 eV. The structure of $\varepsilon_2(\omega)$ is very sensitive to the normalization factor used in the Kramers-Kronig inversion. It must be mentioned that the two different curves of $\varepsilon_2(\omega)$ differ significantly from that reported by Ray and Tauc. Ray and Tauc measured the optical reflectivities in the photon energy range 0.05 eV to 6.0 eV. Using an extrapolation of their reflectivity measurements to higher energies, they computed $\varepsilon_2(\omega)$ by a KK inversion of the reflectivity data. A procedure such as this does not always reveal useful information because the KK inversion procedure is very sensitive to the high energy extrapolation in reflectivity. In the $\varepsilon_2(\omega)$ spectra of pure Fe and the metallic glass there is a structure at about 10 eV. In pure Fe this structure is a plateau; in the metallic glass this is a broad peak. The reason for the enhancement of this structure in the metallic glass is unclear. The photo--emission valence-band spectra of Hricovini and Krempasy [4.3] also indicates a weak structure at about 9 eV below the Fermi level.

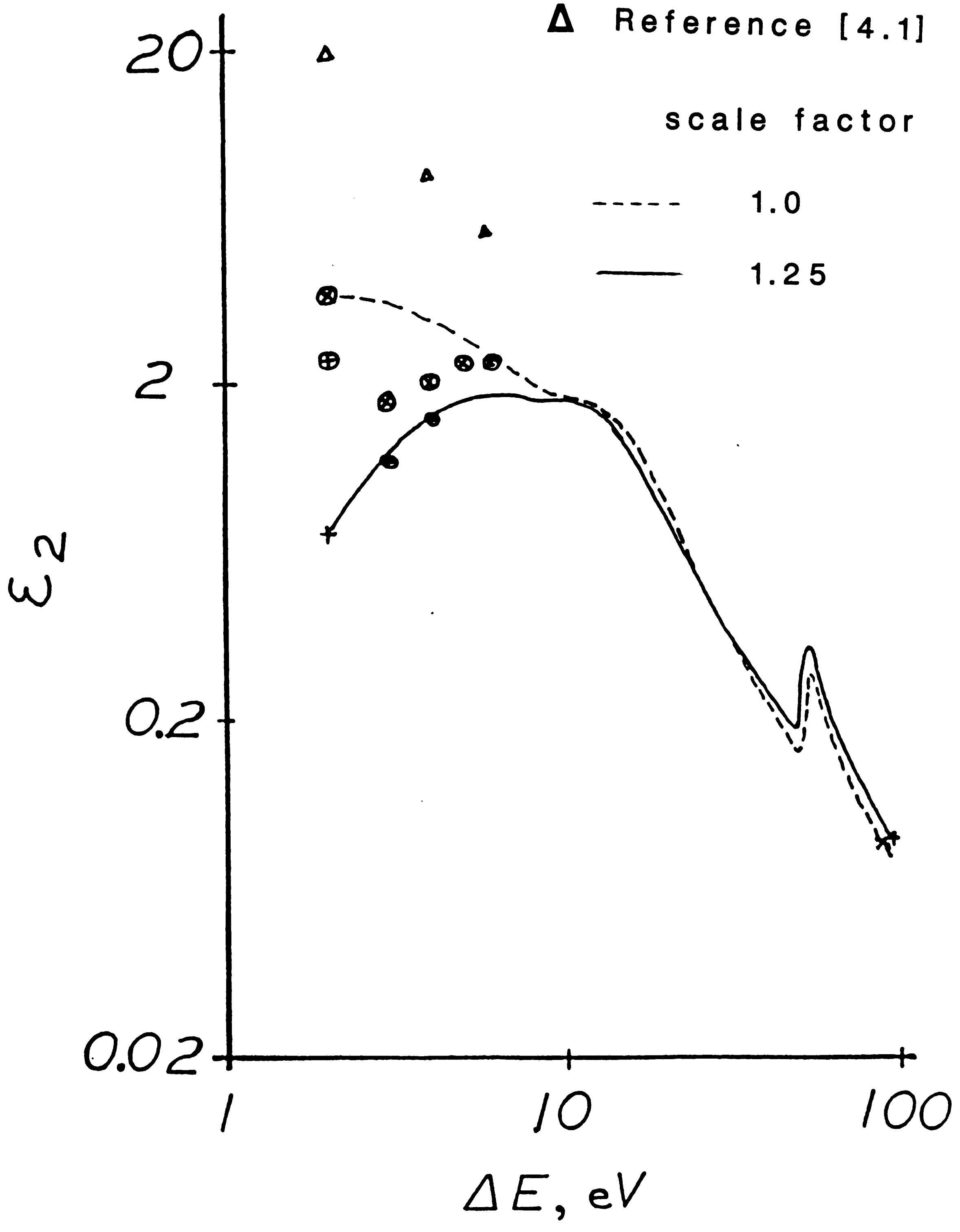

Figure 4.7

$\varepsilon_2(\omega)$ of $Fe_{0.8}B_{0.2}$

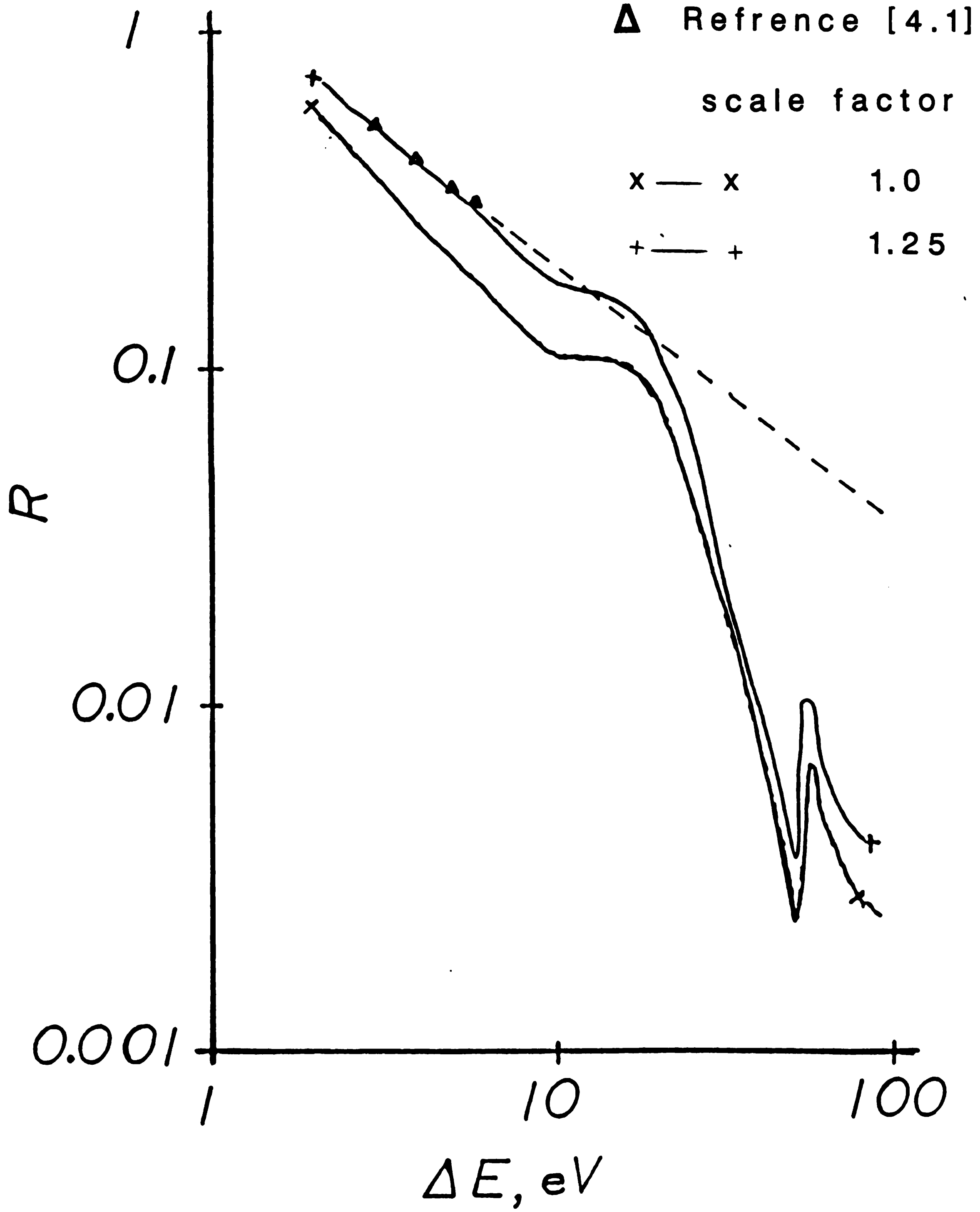

Figure 4.8

R(ω) of $Fe_{0.8}B_{0.2}$

CONCLUSION:

We have measured the optical reflectivity and high energy transmission EELS of melt-spun a-$Fe_{0.8}B_{0.2}$. Using the Kramers-Kronig dispersion relations we have computed the imagery part of dielectric function $\varepsilon_2(\omega)$ and the reflectivity $R(\omega)$ in the energy range 2 eV to 90 eV. The dominant feature is the EELS is at 23.0 eV ± 0.5 eV. This value is about 1 eV to 3.5 eV higher compared to that of pure, crystalline Fe, depending on the criterion used to locate the peak. Several other features were observed in the loss spectrum. Two features at 2.5 eV and 4.5 eV associated with volume excitations by other investigators was seen to be due to surface excitations. No significant changes in the shape or the position of the Fe $M_{2,3}$ core-loss was seen, ruling out a transfer of charge between the metalloid and transition metal atoms. The computed dielectric function $\varepsilon_2(\omega)$ differs significantly from published results while the computed reflectivity agrees with published results in the energy range 2 to 10 eV. Beyond 10 eV the discrepancy is significant.

CHAPTER 5

ORDER-DISORDER EFFECTS IN THE NITI SYSTEM

To identify the effects of loss of long range order on the electronic properties, metallic systems with and without 'artificial' order were studied using electron energy loss spectroscopy. For systems with 'artificial' order we used layered Ni-Ti samples and for systems without long range order (and 'artificial' order) we used amorphous Ni-Ti alloys produced by laser quenching the layered Ni-Ti samples. To investigate the effects of amorphization on the electronic levels we also studied a crystalline Ni-Ti (c - Ni-Ti) alloy. Experimental studies on these three kinds of systems are still limited in number. Artificially layered metallic systems have been used as X-ray mirrors, among other applications. A sound knowledge of their electronic properties is thus essential. Although amorphous metallic alloys have received extensive attention for their interesting magnetic and structural properties, a reliable understanding of their behavior at the microscopic level has not been achieved.

SAMPLE PREPARATION:

The NiTi samples for this study were prepared by using DC Sputtering techniques. Alternating layers of Ni and Ti were deposited on aluminum covered copper substrates. Three different guns were required for the process (Al, Ni and Ti). The sputtering was done in an atmosphere of ultra-pure (99.9999%) Ar; Ar pressure was 3 mtorr. A 1.0 μm layer of Al was deposited on the Cu substrate before depositing Ni and Ti layers. The total thickness of Ni and Ti layers were about 500 A in samples that were made specifically for AEM studies. The samples for magnetic studies and laser-quenched amorphization were about 1400 A in total thickness. Though samples of different layer thicknesses were prepared and studied, we limit our discussion to the results for the 50.8 A Ni/58.5 A Ti system.

Amorphization of these layered systems was accomplished by laser-quenching. Short duration (~ 10 x 10^{-9} sec) Q-switched laser pulses from a Nd-YAG laser was directed on different regions of the sample. The energy of these pulses were varied to yield fluences of 0.2 J/cm^2 to 3 J/cm^2. The region affected by each pulse was about 2 mm in diameter. Optimum amorphization of the layers was obtained at fluences of 1-2 J/cm^2.

Analytical electron microscope studies were done on small pieces of the layered and laser quenched samples that were floated off the Cu substrates by etching the intermediate Al layer with 50% KOH solution. Composition analysis by X-ray EDS showed the presence of Al in small amounts in certain regions of the sample. These regions were avoided while making energy loss measurements. Discs of 3 mm diameter were cut from the crystalline Ni-Ti samples and electrochemically etched for study in the AEM.

RESULTS AND DISCUSSION:

Electron energy loss spectra from 3 eV to 90 eV for layered NiTi, laser quenched NiTi alloy and c - NiTi alloy are shown in Figures 5.1, 5.2 and 5.3 respectively. Preliminary measurement of the optical reflectivity of the layered system is shown in Figure 5.4. Efforts to obtain more accurate and reliable optical measurements are currently underway. We were unable to measure the reflectivity of the laser quenched alloys, due to the limited size of laser quenched regions.

X-ray diffraction studies, using Cu-K_α radiation, of the 50.8 A/58.5 A layered NiTi systems showed fairly sharp Bragg peaks indicating layers of crystalline Ni and Ti. 'Satellite' Bragg peaks indicating good registry between successive layers of Ni and Ti were not seen. We attribute the lack of registry between successive layers to the roughness of the Cu substrates. See Figure 5.5 for the X-ray diffraction pattern.

were floated off the Cu substrates by etching the intermediate Al layer with 50% KOH solution. Composition analysis by X-ray EDS showed the presence of Al in small amounts in certain regions of the sample. These regions were avoided while making energy loss measurements. Discs of 3 mm diameter were cut from the crystalline Ni-Ti samples and electrochemically etched for study in the AEM.

RESULTS AND DISCUSSION:

Electron energy loss spectra from 3 eV to 90 eV for layered NiTi, laser quenched NiTi alloy and c - NiTi alloy are shown in Figures 5.1, 5.2 and 5.3 respectively. Preliminary measurement of the optical reflectivity of the layered system is shown in Figure 5.4. Efforts to obtain more accurate and reliable optical measurements are currently underway. We were unable to measure the reflectivity of the laser quenched alloys, due to the limited size of laser quenched regions.

X-ray diffraction studies, using Cu-K_{α} radiation, of the 50.8 A/58.5 A layered NiTi systems showed fairly sharp Bragg peaks indicating layers of crystalline Ni and Ti. 'Satellite' Bragg peaks indicating good registry between successive layers of Ni and Ti were not seen. We attribute the lack of registry between successive layers to the roughness of the Cu substrates. See Figure 5.5 for the X-ray diffraction pattern.

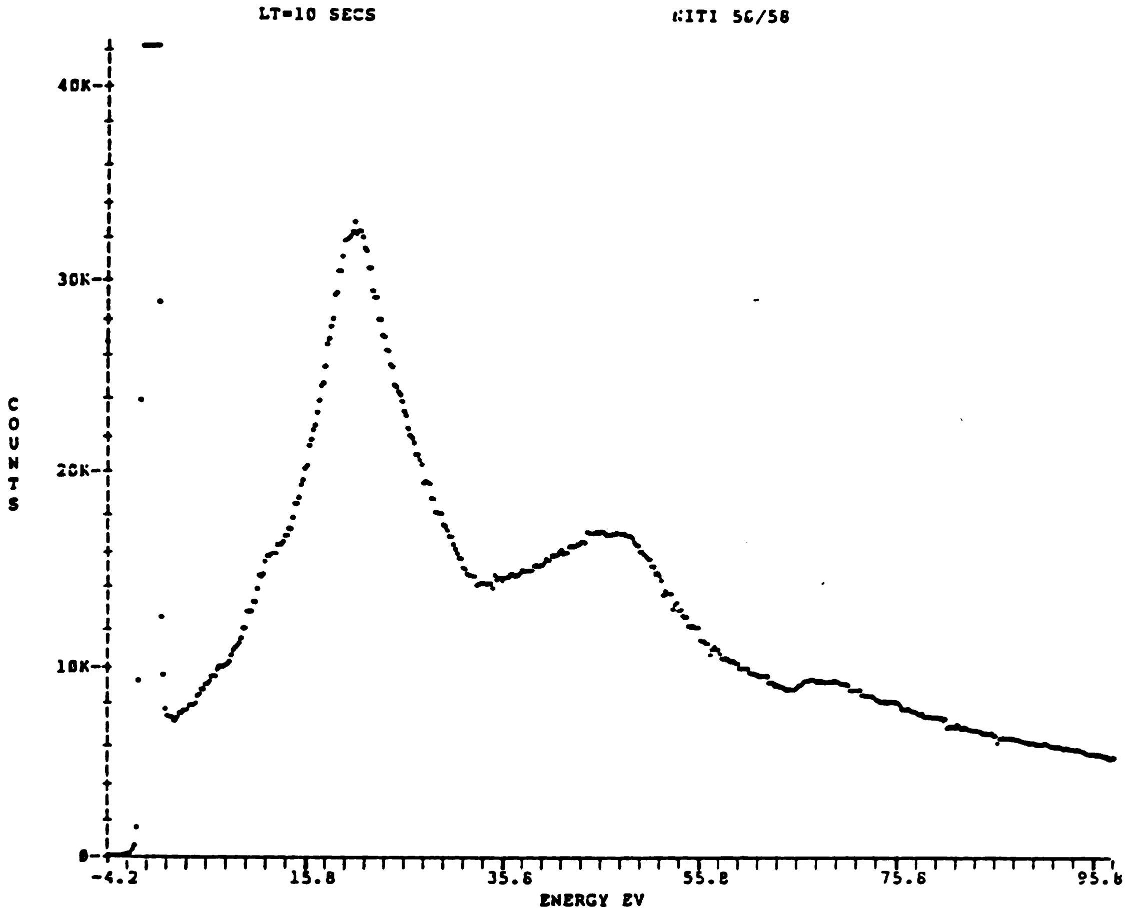

Figure 5.1

EELS of NiTi Layers

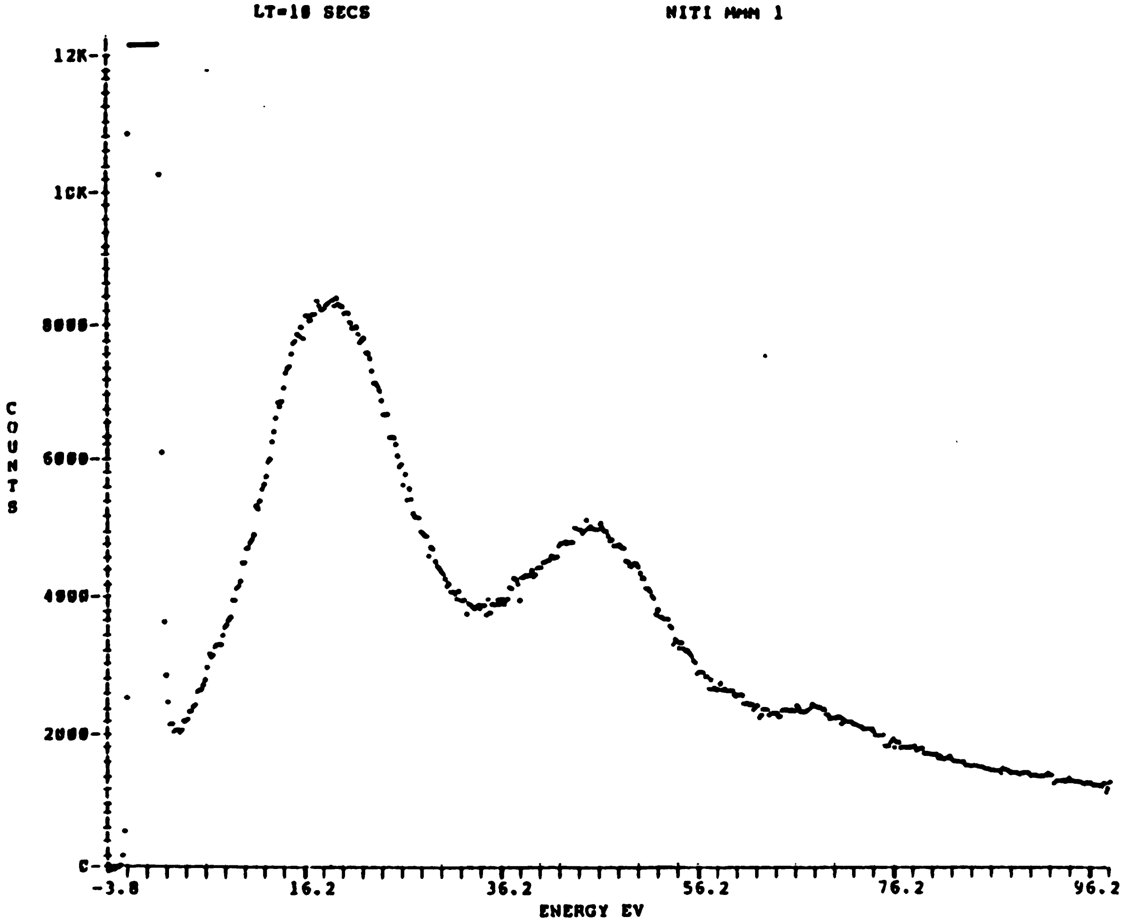

Figure 5.2

EELS of c-NiTi

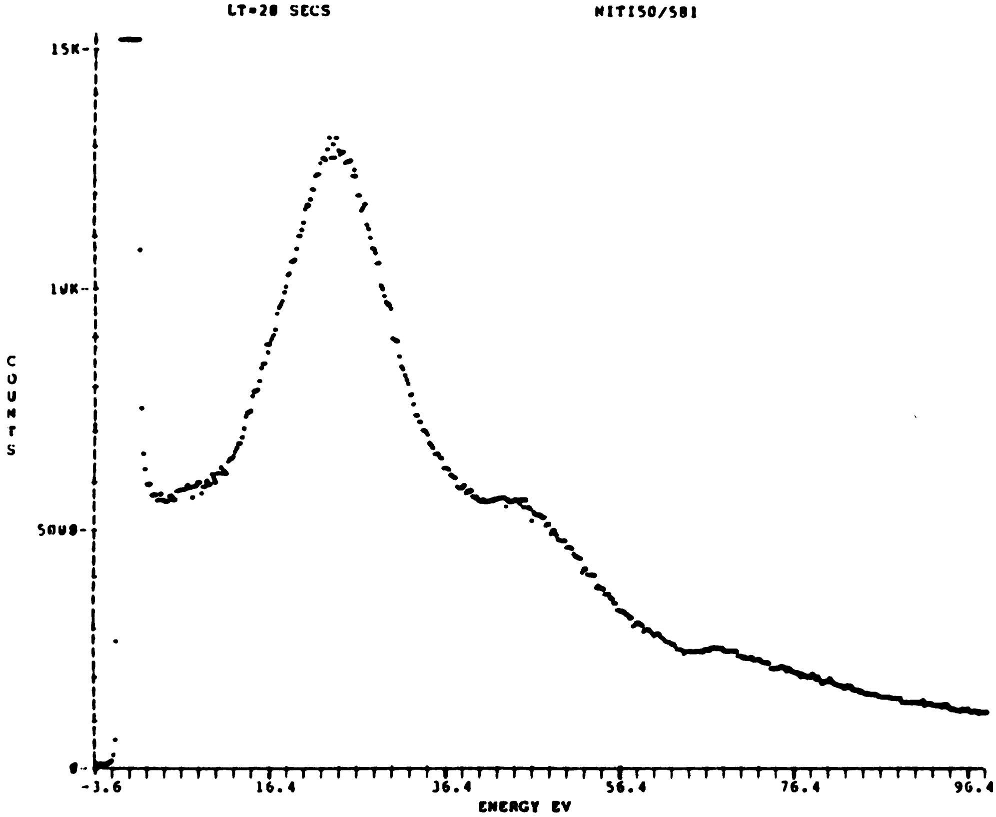

Figure 5.3

EELS of Laser Quenched NiTi

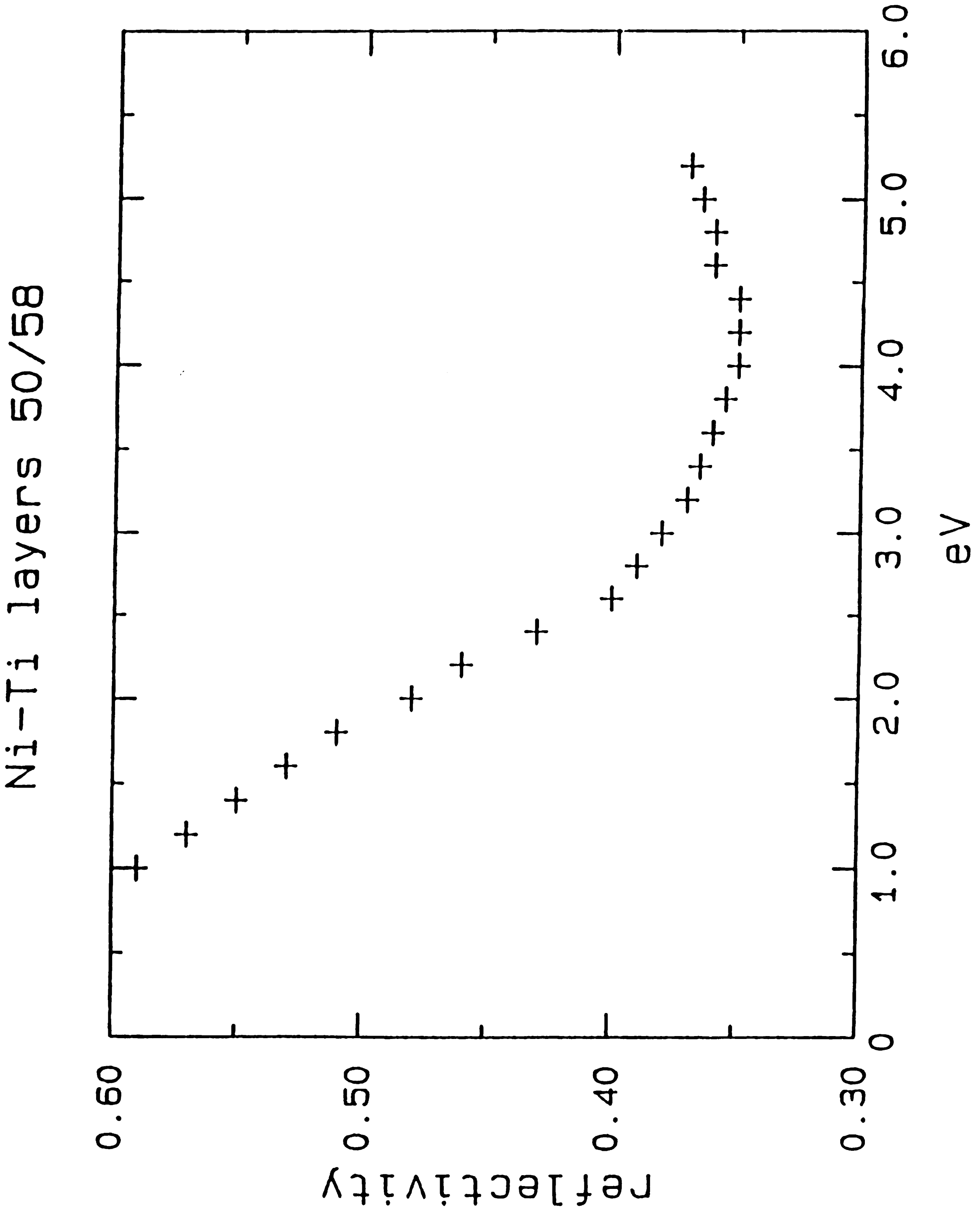

Figure 5.4

R(ω) of NiTi Layers

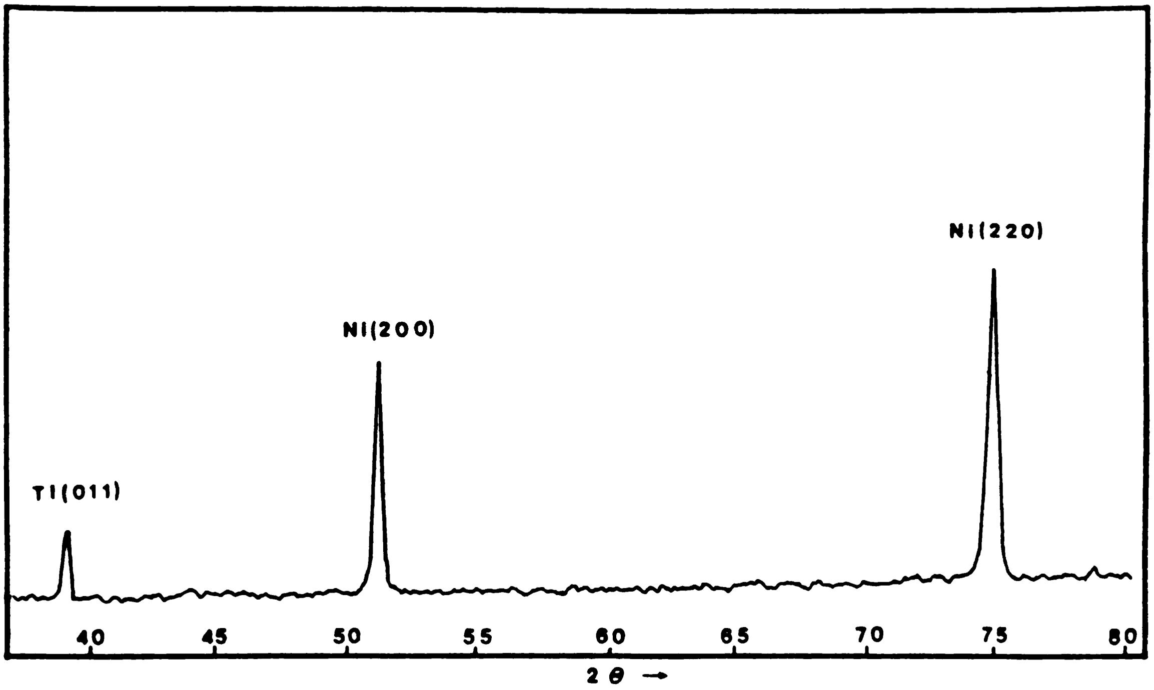

Figure 5.5

X-ray Diffraction of NiTi Layers

The energy loss measurements for the layered NiTi system (Figure 5.1) shows some surprising results. Since the X-ray diffraction studies (Figure 5.5) show sharp Ni and Ti Bragg peaks, it is reasonable to assume that the EELS of this system is a superpostion of the loss spectra of pure Ni and Ti. The layered samples studied had at least 5 layers of Ni (and Ti) to as many as 15 layers. Thus the total thickness of Ni (or Ti) was comparable to the mean free path of electrons for inelastic scattering; chracteristic features of Ni and Ti would be expected to appear in the EELS measurements. Instead of featuring two plasmon peaks at about 17 eV and about 25 eV (the characteristic features of Ni and Ti), the EELS of layered NiTi shows a relatively sharp plasmon at ~ 20.5 eV. This indicates that there is just one 'sea of electrons' and not two - corresponding to Ni and Ti electrons. Lack of clearly defined interfaces between Ni and Ti layers could lead to an 'average' crystal potential and thus a different plasma oscillation. Further examination of the EELS of the layered, laser quenched (Figure 5.2) and crystalline (Figure 5.3) samples shows that there is no appreciable shift in the location of the plasmon peaks in these three systems. The plasmon occurs at about 21.0 ± 1.0 eV in the three spectra, indicating that there is no significant change in the electron density. That the EELS of the layered NiTi and c - NiTi are similar is by itself surprising, especially when X-ray diffraction studies indicate the presence of well defined regions of Ni and Ti. Using the free electron model and counting the outer s and d electrons only, the plasmon energy should be about 6 eV lower than the observed plasmon energy. However, electron diffraction (Figures 5.6 & 5.7) studies of the layered and amorphous systems show that there is a clear change in the crystal structure as a result of laser quenching. The layered NiTi sample has 3 sharp diffraction peaks whereas the laser quenched has only one broad peak in the diffraction pattern.

The EELS of laser quenched NiTi alloy is similar to that of the transition metal-transition metal systems $Fe_{92}Zr_8$ and NiZr [5.1]. These two alloys have a broad plasmon at 23-25 eV. The $N_{2,3}$ core losses of Zr (40 eV) the $M_{2,3}$ losses of Fe (55 eV) and Ni (65 eV) are also seen. A similarity between the spectra of NIZr and NiTi might be expected because Zr and Ti share common outer electronic structure. The spectra of NiTi and $Fe_{92}Zr_8$,superficially similar show some differences on closer examination.

The $M_{2,3}$ ($3P_{3/2,1/2} \rightarrow$ allowed states above E_F) core losses of Ti clearly show the effects of amorphization. These features occur at about 45 eV ($M_{2,3}$ of Ti). In the layered NiTi and c - NiTi samples the Ti core loss is a broad feature extending from about 35 eV to about 55 eV; the $M_{2,3}$ excitation of Ni is also clearly visible as a step

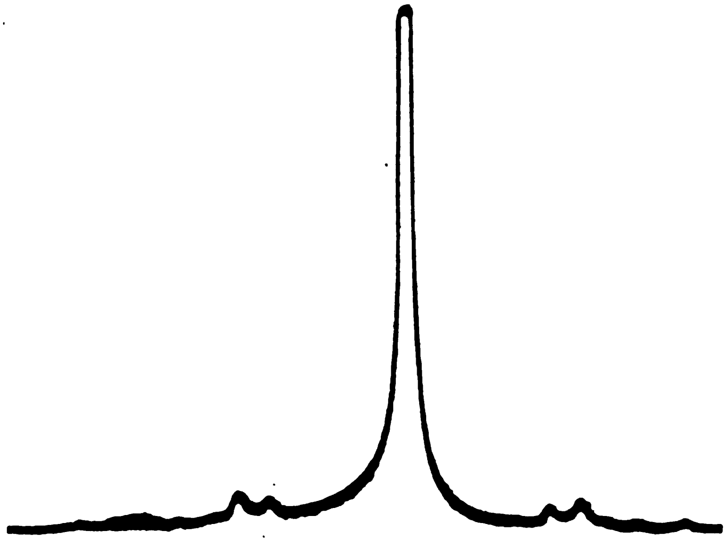

Figure 5.6

Electron Diffraction of NiTi Layers

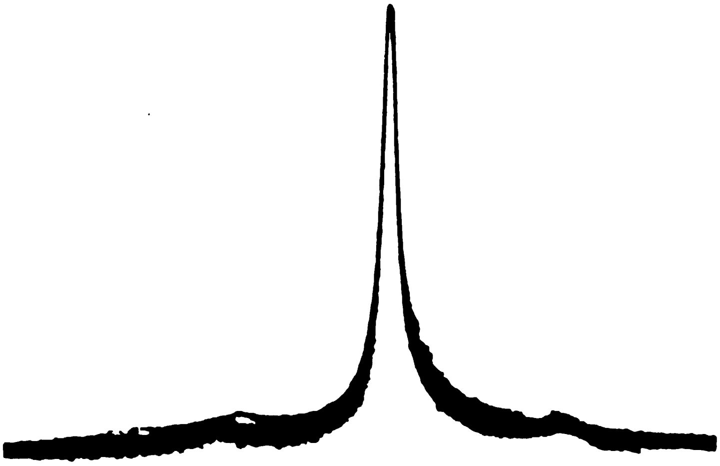

Figure 5.7

Electron Diffraction of Laser Quenched NiTi

at about 65 eV. In the EELS of the laser quenched alloy the Ti core loss is reduced to a slope change at about 43 eV whereas the Ni $M_{2,3}$ excitation seems to have undergone very little change. This observation coupled with the earlier observation that the plasmon oscillations are not influenced by amorphization produces an intriguing puzzle.

Typically, in the process of alloying, it is the outer electrons that are affected the most. In transition metals the electrons involved are the outer s and d shell electrons. In the 3d transition metals changes in the 4s and 3d bands on alloying can be expected to be observed in the plasma oscillations. Instead of a change in the plasmon excitation, we find a drastic change in the $M_{2,3}$ core excitation of Ti. The $M_{2,3}$ core losses of Ni do not show significant changes. The $M_{2,3}$ transitions of Ni and Ti share some of the same final states--those unoccupied levels above E_F. In addition to these states the final states of the core losses may include localised states associated with the creation of excited but un-ionized Ni or Ti atoms; such localised (virtual bound states) have been observed in alloy systems with low impurity concentrations. As the impurity concentration increases these localised states interact with each other and turn in to shared, extended states

In an alloy with equal amounts of Ni and Ti formation of such localised states is thus unlikely. Changes in the

final states of transitions associated with the $M_{2,3}$ core losses would be reflected as changes in the plasmon loss and the Ni $M_{2,3}$ core loss at about 65 eV. The lack of observable changes in the plasmon and the Ni core loss argue against such final state changes. It is thus reasonable to associate the changes in the Ti $M_{2,3}$ loss feature with changes in the Ti 3p levels. Such a change in the core state is rare and puzzling. To test this hypothesis, one must resort to experimental techniques that probe the core levels--methods like X-ray photoemission spectroscopy (XPS). In this technique monochromatic x-ray photons of sufficiently high energy ($h\nu \geq 50$ eV) are used to knock out electrons from core levels of the sample and the energy distribution of the electrons studied. This would allow the study of the density of states at energies of the 3p levels.

CONCLUSION:

Electron energy loss spectra of 50.8 A/58.5 NiTi layered samples, laser quenched amorphous NiTi alloy and crystalline NiTi alloy were measured. The EELS of the layered NiTi sample resembled the EELS of the crystalline sample and was significantly different from a spectrum obtained by a simple superpostion of the spectra of Ni and Ti. No appreciable difference was seen between the EELS of layered and laser quenched sample in the low energy region (< 35 eV). The spectra of laser quenched NiTi were

qualitatively similar to the spectra of a-NiZr and a-$Fe_{92}Zr$. Examination of the Ti $M_{2,3}$ core losses at about 45 eV in the layered and amorphous NiTi samples revealed that amorphization by laser quenching had significantly changed the structure of this loss feature. These changes were not seen in the EELS of the crystalline phase of the alloy. A profound change in the Ti 3p bands upon amorphization is one possible explanation for this change.

APPENDIX

KRAMERS-KRONIG ANALYSIS AND THE OPTICAL FUNCTIONS

In an electron energy loss measurement the quantity measured, $I(E,\theta)$, is the intensity of electrons that have lost energy E and scattered in the direction (θ,ϕ). Using the results of classical scattering theory the following expression relating $I(E,\theta)$ and the macroscopic dielectric function $\varepsilon(E)$ of the scattering material may be derived [A.1, A.2].

$$I(E,\theta) = I_0 N \frac{1}{2\pi^2 a_0 n E_0} \cdot \mathrm{Im} - \frac{1}{\varepsilon(E)} \cdot \frac{1}{\theta^2 + \theta_E^2}$$

Here a_0 is the Bohr radius, n the density of the solid in atoms/cm^3 and N the number of atoms/area in the volume examined.

In a typical EELS measurement the detector angle θ is usually fixed and θ_E varies over a small range.

$$I(E,\theta) \propto \mathrm{Im}\ (-1/(\varepsilon(E))$$

The function $1/\varepsilon(E)$ is the loss function and

$\varepsilon(E) = \varepsilon_1(E) + i\ \varepsilon_2(E)$. In terms of ε_1 and ε_2 the loss function $1/\varepsilon(E)$ is

$$\frac{1}{\varepsilon(E)} = \frac{\varepsilon_1(E) - i\varepsilon_2(E)}{(\varepsilon_1(E))^2 + (\varepsilon_2(E))^2}$$

The bulk dielectric function $\varepsilon(E)$ is a macroscopic description of the electronic response to external electric fields. The dielectric function contains all the essential features of the electronic excitation spectrum The structure in $\varepsilon_2(E)$ corresponds to critical points in the band transitions. The ability to measure the dielectric function directly gives us an opportunity to test the results of theoretical calculations.

KRAMERS-KRONIG DISPERSION RELATIONS:

The response of electrons in a solid to external fields (such as the electric fields of high energy electrons) can be accurately described by the linear response theory [A.3]. An important result of the linear response theory is the causality relationship between the imaginary part of the dielectric function ε and its real part. These relations are the well known Kramers-Kronig dispersion relations [A.4].

$$\varepsilon_1(\omega) - 1 = \frac{1}{\pi} P\int_{-\infty}^{\infty} \frac{\varepsilon_2(\omega')\, d\omega'}{\omega'-\omega}$$

$$\varepsilon_2(\omega) = \frac{-1}{\pi} P\int_{-\infty}^{\infty} \frac{[\varepsilon_1(\omega') - 1]\, d\omega'}{\omega' - \omega}$$

In addition $\varepsilon_1(\omega)$ and $\varepsilon_2(\omega)$ also satisfy the following

properties

$$\varepsilon^*(\omega) = \varepsilon(-\omega)$$

$$\varepsilon_1(-\omega) = \varepsilon_1(\omega) \quad \text{and} \quad \varepsilon_2(-\omega) = -\varepsilon_2(\omega)$$

The Kramers-Kronig relations may be rewritten as

$$\varepsilon_1(\omega) - 1 = \frac{2}{\pi} P\int_{-\infty}^{\infty} \frac{\omega'\varepsilon_2(\omega')\, d\omega'}{\omega'^2 - \omega^2}$$

$$\varepsilon_2(\omega) = \frac{-2}{\pi} P\int_{-\infty}^{\infty} \frac{[\varepsilon_1(\omega') - 1]\, d\omega'}{\omega'^2 - \omega^2}$$

The integrals in the expressions above are the Cauchy principal value integrals, avoiding the singularity at $\omega'=\omega$. A similar set of Kramers-Kronig dispersion relations exist for the loss function $1/\varepsilon(\omega)$. For example

$$\text{Re}\, [1/\varepsilon(\omega) - 1 = \frac{2}{\pi} P\int_{0}^{\infty} \text{Im}\, \frac{1}{\varepsilon(\omega')} \frac{\omega' d\omega'}{\omega'^2 - \omega^2}$$

If the Im $(1/\varepsilon(\omega))$ is known over a wide range of energies it is possible to compute numerically the functions $\text{Re}(1/\varepsilon(\omega))$, $\varepsilon_1(\omega)$ and $\varepsilon_2(\omega)$.

QUANTITATIVE ANALYSIS:

In the electron energy loss spectrum (EELS) of a real system, the contributions from surface excitations, multiple losses and the strong zero loss peak (elastically scattered primary electrons) make quantitative analysis of the spectrum difficult. Fortunately, a number of procedures are available to handle these problems. We discuss below some of these techniques adopted by us.

SURFACE EXCITATIONS:

In the EELS of a very thin sample ($t_{eff} < 0.2$) the contribution from surface excitations are relatively significant. Surface excitations do not scale with the thickness while the rest of the spectrum does. In our energy loss studies we confined our attention to regions that were thicker ($0.4 < t_{eff} < 1.0$) This minimized the errors due to the presence of surface excitations. No attempt was made to remove the contributions from surface excitations.

MULTIPLE LOSSES:

When the thickness of the sample is significant (≳ 50%) compared to the mean free path for inelastic scattering, the incident electrons loose energy to more than one excitation. Electrons that have lost energy by multiple scatterings give an abnormally high intensity at higher energies (> 20 eV) in the energy loss spectrum. In

general, the effect of double losses is much more than other higher order losses. In this study we limited our efforts to removing double losses from the energy loss spectra.

The procedure adopted by us for computing the intensity of double losses is similar to the techniques described by Daniels et al [A.4] and R. F. Egerton [A.2]. This method is really an approximation of a more vigorous technique and is good for only low energy losses (under 100 eV). The intensity of double losses at a (total) loss energy E is

$$I_2 (E) \cong \frac{1}{2I_0} \int_{\delta}^{E} I(E') \, I(E'-E) \, dE' \qquad , E > 15 \text{ eV}$$

The lower limit δ, of the integral ensures that the zero loss peak is avoided in this computation. In this approximation it is assumed that the region below about 15eV is free from double losses. I_0 is the zero loss peak intensity integrated over a few channels around 0 eV. This approximation also assumes that the instrumental resolution is very narrow and symmetric. The double loss corrected spectrum is given by the following expression.

$$I_{correct} (E) = I_{raw}(E) - \frac{1}{2I_0} \int_{\delta}^{E} I_{raw} (E-E) dE$$

$$E \geq 15 \text{ eV}$$

ZERO LOSS PEAK:

At the low energy end of the spectrum is the intense peak due to elastically scattered electrons. The tail of this zero loss peak extends to about 3eV of 4eV; it is also a function of the thickness of the sample. For sample thickness t_{eff} = 0.5 this tail is fairly narrow and may be eliminated by linearly extrapolating the spectrum such that I(0 eV) = 0 and I(3 eV) = $I_{meas.}$ (3 eV). This method yields fairly accurate spectra for metals and metallic alloys.

A spectrum, stripped of the zero loss peak and corrected for double losses must be scaled down before being used as input for the Kramers-Kronig inversion routine. This step is necessary to obtain accurate optical functions.

KRAMERS-KRONIG INVERSION:

The numerical integration technique used was the trapezoidal rule. This technique proved adequate because the energy loss spectra were available in 512 channels at 0.2 eV/channel steps. Several spectra of pure metals were used to test the KK inversion routine. The output of the KK inversion routine was the real part of the loss function, $Re(1/\varepsilon(E))$. The optical functions $\varepsilon_1(E)$, $\varepsilon_2(E)$ and reflectivity R(E) were computed using the following relations:

$$\varepsilon_1(E) + i\,\varepsilon_2(E) = \frac{\mathrm{Re}(1/\varepsilon) - i\mathrm{Im}(1/\varepsilon)}{|\mathrm{Re}(1/\varepsilon)|^2 + |\mathrm{Im}(1/\varepsilon)|^2}$$

$$R(E) = \frac{\sqrt{\varepsilon_1^2 + \varepsilon_2^2} + 1 - \sqrt{2(\sqrt{\varepsilon_1^2 + \varepsilon_2^2} + \varepsilon_1)}}{\sqrt{\varepsilon_1^2 + \varepsilon_2^2} + 1 + \sqrt{2(\sqrt{\varepsilon_1^2 + \varepsilon_2^2} + \varepsilon_1)}}$$

Optical reflectivity of the systems under study were also measured directly in the photon energy range 0.6 eV to 5.0 eV. The scaling factor for the EELS was adjusted (to within 10%) to yield a match between the directly measured and computed optical reflectivities. The computed optical functions were not very accurate for energies below 4.0 eV as revealed by tests on pure metals.

REFERENCES

[2.1] Elements of X-ray Diffraction Cullity, Addison Wesley Publishing Co., 1971.

[2.2] Solid State Physics, N.W. Ashcroft and N.D. Mermin, Holt, Reinhart and Winston, 1976.

[2.3] X-ray Diffraction, B.E. Warren, Addison Wesley Publishing Co., 1969.

[2.4] Constitution of Binary Alloys, M. Hansen, McGraw Hill Book Co., 1958.

[2.5] Introduction to Analytical Electron Microscopy, Chapter 15, J.J. Hren, J.I. Goldstein and D.C. Joy, Plenum Press, 1979.

[2.6] Electron Energy Loss Spectroscopy in the Electron Microscope, R.F. Egerton, Plenum Press, 1986.

[2.7] Transmission Electron Microscopy, G. Thomas and M.J. Goringe, John Wiley and Sons, 1979.

[2.8] Introduction to Analytical Electron Microscopy, Chapter 3 & 4, J.J. Hren, J.I. Goldstein and D.C. Joy, Plenum Press, 1979.

[2.9] Beginner's Guide to X-ray Analysis in an AEM, Part 1, N.J. Zaluzec, Argonne National Lab.

[2.10] Philbert and R. Tixier, Brit. J. Appl. Phys 1, 685, 1968.

[2.11] G. Cliff and G.W. Lorimer, J. Microscopy 103. 203, 1975.

[2.12] Introduction to Analytical Electron Microscopy, Chapter 7. J.J. Hren, J.I. Goldstein and D.C. Joy, Plenum Press, 1979.

[2.13] Electron Energy Loss Spectroscopy in the Electron Microscope, Chapter 3, R.F. Egerton, Plenum Press, 1986.

[2.14] J. Daniels, C.V. Festenberg, H. Raether and K. Zeppenfeld, Springer Tracts of Modern Physics 54, 78 - 135, 1970.

[2.15] Elementary Excitations in Solids, D. Pines W. Benjamin Inc., 1964.

[2.16] M.S. Issacson and M. Utlaut, Optic, 50, 213, 1978.

[3.1] R.E. Hummel, Phys. Stat. Sol. (a) 76, 11, 1983.

[3.2] Constitution of Binary Alloys, M. Hansen McGraw Hill Book Co., 1958.

[3.3] Elements of X-ray Diffraction, Cullity, Addison Wesley Publishing Co., 1971.

[3.4] Electronic Properties of Materials, R.E. Hummel Springer Verlag, 1985.

[3.5] J. Freidel, Can. J. Phys. 34,1190, 1956.

[3.6] P.W. Anderson, Phys. Rev 124, 41, 1968.

[3.7] H.P. Myers, L. Walden and A. Karlsson, Phil. Mag. 18, 725, 1968.

[3.8] L.A. Feldkamp, L.C. Davis and M.B. Stearno Phys. Rev. B 15,5535.

[3.9] J. Daniels, C.V. Festenberg, H. Raether and K. Zeppenfeld, Springer Tracts of Modern Physics, 1970.

[3.10] Ya Ksendzov, Phys. Stat. Sol. (b) 93, 415, 1979.

[3.11] Private discussions with A. Bansil and R. Prasad North Eastern University and S.D. Mahanti Michigan State University, 1986, 1987.

[3.12] R.S. Rao, A. Bansil, H. Asonsen and M. Pessa, Phys. Rev B 29, 1713, 1984.

[4.1] S. Ray and J. Tauc, Solid State Comm. 34, 769, 1980.

[4.2] E. Colavita, M. DeCrescenzi, L. Papagno, L.S. Caputi, R. Scarmozzino, R. Rosei and E. Tosatti, Phys. Rev. B 25, 2490, 1982.

[4.3] K. Hricovini and Krempasky, J. Phys. F: Met. Phys. 15, 1321, 1985.

[4.4] Th Paul and H. Neddermeyer J. Phys. F: Met. Phys. 15, 79, 1982.

[4.5] Abd-Elmeguid, H. Mickletz and I. Vincze, Phys. Rev. 25, 1, 1983.

[4.6] M. Eibschtuz, M.E. Lines and H.S. Chen Phys. Rev B, 28, 425, 1983.

[4.7] C.L. Chien K.M. Unruh Phys. Rev. B 29, 207, 1981.

[4.8] M. Decrescenzi, E. Colavita, L. Papagno, G. Chiarello, R. Scarmozzino, L.S. Caputi and R. Rosei, J. Phys. F: Met. Phys. 13,895, 1983.

[4.9] A. Ammou and G. Krill Solid State Comm. 33, 1087, 1980.

[4.10] Electron Energy Loss Spectroscopy in the Electron Microscope, R.F. Egerton page 227 Plenum Press, 1986.

[4.11] E. Colavita, M. DeCrescenzi, L. Papagno R. Scarmozzino, L.S. Caputi, R. Rosei and E. Tosatti, Phys. Rev. B 25,2490, 1982.

[5.1] C.L. Foiles, Solid Satte Comm., 53, 533, 1985.

[A.1] Introduction to Analytical Electron Microscopy Chapter 3, J.J. Hren, J.I. Goldstein and D.C. Joy, Plenum Press, 1979.

[A.2] Electron Energy Loss Spectroscopy in the Electron Microscope, R. Egerton, Plenum Press, 1986.

[A.3] Classical Electrodynamics, J.D. Jackson, John Wiley and Sons, 1962.

[A.4] J. Daniels, C.V. Festengberg,, H. Raether and K. Zeppenfeld, Springer Tracts of Modern Physics 54, 78, 1970.